Development and characterization of KAGRA Photon Calibrator for the accurate calibration of gravitational wave signals
（重力波精密較正のためのKAGRA輻射圧キャリブレータの開発及び性能評価）

by

Bin-Hua Hsieh

A thesis submitted in partial fulfillment for the degree of
Master of Science

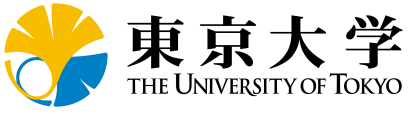

in the
Institute for Cosmic Ray Research
Department of Physics, School of Science

THE UNIVERSITY OF TOKYO

August 2018

THE UNIVERSITY OF TOKYO

Abstract

Institute for Cosmic Ray Research
Department of Physics, School of Science

Master of Science

by **Bin-Hua Hsieh**

KAGRA is an underground-based Large-scale Cryogenic Gravitational wave Telescope which is located in Kamioka, Gifu, Japan. It is a 2.5 generation gravitational wave detector since it is improved from the second-generation detector by employing underground environment and cryogenic technologies for mirrors into a three kilometers interferometer, which are two improvements on the third generation detectors. In order to accurately estimate the physical parameters from a gravitational wave signal, the calibration of the gravitational wave signal is important. We developed Photon Calibrator to achieve 1% calibration accuracy. In this thesis, I describe the development and characterization of KAGRA Photon Calibrator, which is a tool used for calibration of KAGRA detector.

Photon Calibrator generates two power modulated laser beams using an auxiliary laser source. Radiation pressure from the modulated laser beams generates the force on the mirror surface, modulating the mirror position. The mirror displacement can be derived from input absolute laser power. By comparing the mirror displacement and interferometer output, the mirror displacement can be calibrated. In the KAGRA Photon Calibrator, we employ a 20 watt laser, which allows us to generate a modulated signals in high frequency easily, and the usage of twin AOMs allows us to mitigate the rotation effect of the mirror. Since we use the auxiliary laser source to modulate the mirror, we prevent Photon Calibrator from being a noise source of the detector by requiring the unintended mirror displacement induced by Photon Calibrator to be ten times smaller than the sensitivity of the detector. The power stabilization of Photon Calibrator is an important issue. We use an active controller called Optical Follower Servo to control and reduce the relative power noise of the laser and the harmonic noise of the modulated signal. Finally, we constructed a 72 meters Photon Calibrator and checked the power loss and power stabilization of the system.

Acknowledgements

It would not be possible for me to accomplish this thesis without the assistance of many people. I am using this opportunity to express my gratitude to everyone who supported me throughout this master course.

First, I would like to express the deepest appreciation to my supervisor Prof. Takaaki Kajita, who gave me a chance to join the KAGRA gravitational wave research. I was impressed by his passion in scientific research and the hardworking spirit. Although his time is occupied by many works and activities, he still took time out of his busy schedule to concern and instruct me in my research and life. He gave me opportunities to join the international conferences, which makes me able to share my research achievement to the world.

Besides my supervisor, I would also like to acknowledge with much appreciation the crucial role of Dr. Yuki Inoue for introducing me to the research of calibration. His sagacity and diligence on research gave me a deep impression. He always gives many insightful suggestions on my study, provides powerful assistance when I have difficulties on my research, helps me on negotiating the research schedule with other groups, and gives many useful comments on my thesis. I have been trained to be a researcher under his instruction, and have been able to conduct a meaning and prospective research with his guidance.

I would like to express my special gratitude and thanks to Prof. Sadakazu Haino for giving large support on my study. He leads the calibration group, provided his budget on purchasing instruments for my research, and gave his support for my research in the KAGRA site. He shared his abundant research experience, which made me understand the important attitude of being an outstanding researcher.

My sincere thank also goes to Prof. Takayuki Tomaru, who gave me a large support on not only my study but also on my life in KEK and in the KAGRA site. He has always given perceptive recommendations to me and provided many necessary instruments for my study. He encouraged me while I feel frustrated with my research, and his sense of humor made me feel relieved to continue doing research.

I am profoundly grateful to Prof. Nobuyuki Kanda, who conduct an important budget for my instruments on my calibration research. He provided critical comments on my report, which helped me understand the blind spot in my study and improve my research achievement.

A special thank goes to Dr. Takaaki Yokozawa, who gave me a large support especially during my stay in the KAGRA site. He spent a lot of time accompanying me to the KAGRA Y-end, helped me prepare the necessary instruments, and gave me many useful comments on my research. He also provided powerful assistance when I had difficulties in research.

I am also deeply thankful to Dr. Takahiro Yamamoto, who taught me how to use the digital system in the KAGRA site. Thanks to his instruction, I am able to use employ the digital system in my Photon Calibrator research, which made the data acquisition and data analyzation much easier.

I would also like to thank Dr. Darkhan Tuyenbayev, who gave me a lot of support on my research in the KAGRA site. Thanks to his experience in LIGO, his assistance in beam alignment and power measurement was very critical.

I would also like to thank Dr. Chihiro Kozakai, who gave me a critical supports in the KAGRA site. She provided me with a lot of suggestions for my experimental results, and also gave me a lot of comments on my thesis.

I would also like to thank Yu-Kuang Chu (Cory), who gave me a lot of ideas while discussing with Pcal problems. His cheerful personality also made the lab life more interesting.

I appreciate Prof. Jun'ichi Yokoyama, who is my secondary supervisor in GSGC program, gave me a lot of advice when I presented my research progress to him. He concerned about my study life in Japan and helped me deal with some issues for a international student to stay in Japan.

I would like to thank Prof. Takao Nakagawa and Prof. Katsuaki Asano to be my referees in the thesis defense presentation. They gave me a lots of comments and pointed out the problems in my research which made me understand what I should improve.

I would like to express my gratitude to the people in High Energy Accelerator Research Organization(KEK). Emiko Kotaki, Ayako Hagiwara, Ayako Ueda gave me a lot of support and managed my stay in KEK. I would like to thank Kunihiko Hasegawa, who taught me a lot of knowledge about interferometer. He generously provided me with the drawings of green laser in an optical layout. His humorous personality makes me feel relieved in the lab research life. I was also enjoyed while playing basketball with him. I also want to thank Tomohiro Yamada gave me a large support when I came to KEK first time also during my stay in KEK. I also received a lot of suggestions about applying JSPS Research Fellowships for Young Scientists and writing the master thesis from his experience. He was a very good chef and provided me extremely delicious "Lu-rou-fan (魯肉飯)". I would like to thank Takaharu Shishido and Rishabh Bajpai, who also gave me an interesting lab research life. The sporting life with Takaharu Shishido was also very exciting.

People in the KAGRA site also gave me a lot of assistance. Dr. Takafumi Ushiba, Masayuki Nakano, Koki Okutomi, Takahiro Miyamoto and Yutaro Enomoto, helped me commuting between locomotion and Kamioka office many times. I would like to show my gratitude to them. I appreciate NAOJ team members for helping me commuting from Locomotion to KAGRA site. Takahiro Miyamoto also gave me a large support when he still stayed in KEK. He introduced the the KAGRA and cryogenic suspension

system to me in the beginning when I came to KEK, also helped me when I moved my house to Tsukuba. The discussion and gym visiting with Kouseki Miyo in the KAGRA site were also interesting.

I am also grateful to the people in Institute for Cosmic Ray Research (ICRR). Rie Kikuchi, Ai Chida, Akiko Aota helped me about the travelling fee reimbursement whenever I had a business trip to Kamioka or attended the international conference in other countries. Chieko Mashima helped me for my life in ICRR especially before and on the first day when I reached Japan. Hiroki Tanaka, who was my tutor in the first semester of my master course, helped me deal with the issue which I encountered as staying in Japan for a student. Ryohei Kozu, Kohei Yamamoto, and Junjie Xia not only gave me a lot of interesting discussions in the group meeting but also provide an interesting life in locomotion.

I appreciate the secretaries in Kamioka office helped me during my stay in Kamioka, and technicians helped me with the mine works. I would like to thank the staffs in Physics office help me for many documentation works. Also, I would like to thank Ms. Kazuyo Sawabe for helping me dealing with the documentation work for GSGC program. I want to thank GSGC program give me the chance to start my research life in the University of Tokyo.

Finally, I would like to thank my parents, who agreed with me to study abroad in Japan and supported my research life. With their assistance, I could concentrate on my research and do not need to worry about my family.

Contents

List of Figures

List of Tables

Abbreviations

AOM	Acousto-Optic Modulator
ADC	Analog to Digital Converter
BBH	Binary Black Hole
BNS	Binary Neutron Star
CBC	Compact Binary Coalescence
CW	Continuous Wave
DAC	Digital to Analog Converter
DGS	Digital System
ETM	End Test Mass
EXA	X-End A Chamber
EYA	Y-End A Chamber
EYC	Y-End C Chamber
Gcal	Gravity Field Calibrator
GS	Gold Standard
GW	Gravitational Wave
ITM	Initial Test Mass
IR	Infrared
LCGT	Large-scale Cryogenic Gravitational Wave Telescope (the KAGRA)
LHO	LIGO Hanford Observatory
LLO	LIGO Livingston Observatory
MEDM	Motif Editor and Display Manager
OFS	Optical Follower Servo
Opamp	Operational Amplifier
Pcal	Photon Calibrator
PD	Photodetector

QPD	Quadrant Photodiode
RPN	Relative Power Noise
Rx	Receiver Module
SNR	Signal to Noise Ratio
Tcam	Telephoto Camera
TF	Transfer Function
Tx	Transmitter Module
UGF	Unity Gain Frequency
VGA	Variable Gain Amplifier
WS	Working Standard

Physical Constants

Speed of Light	c	=	2.997×10^8 ms^{-1}
Newtonian Constant of Gravitation	G	=	6.674×10^{-11} m^{3}kg^{-1}s^{-2}
Solar Mass	$M_\odot$	=	1.988×10^{30} kg
Megaparsec	Mpc	=	3.085×10^{22} m

Dedicated to my parents

Chapter 1

Introduction

In our childhood, we had experiences of watching the dim or bright, wax and wane of the moon by our eye. After we grew up, we use telescopes to observe the Mars, Jupiter and other stars in the sky. We have already known that we are able to observe the universe by light, i.e., electromagnetic waves. Scientists have been using telescopes to collect the electromagnetic radiation with different wavelengths from cosmic sources. However, there are some cosmic objects which do not emit electromagnetic radiations. For example. black hole, which is an extremely massive object, have a strong gravitational field that nothing can escape from inside even light. Dark matter, which constitutes 27% of the universe, does not emit electromagnetic radiations either. Furthermore, electromagnetic waves can only be observed 10^5 years after the Big Bang, which means we are not able to use electromagnetic waves to understand the universe before that. Therefore, exploring the universe using other approach is necessary.

Gravitational waves are one of the methods to observe cosmic objects which do not emit electromagnetic radiations and explore the early universe 10^5 years after the Big Bang. It was proposed by Einstein in 1916 from the linear approach of general relativity. The first indirect detection of gravitational waves was detected by R. Hulse and J. Taylor from the binary neutron star PSR B1913-16 in 1974. They observed that the orbital period of PSR B1913-16 decreases gradually, while the orbital decay is consistent with the theoretically expected change in general relativity. Gravitational waves have not been directly detected until 2015, when LIGO, two gravitational wave detectors located in the USA, detected the first gravitational waves signal GW150914 generated by binary black hole system. Two years later, a gravitational waves GW170817 generated by binary neutron star was detected by LIGO and Virgo, and the short gamma-ray burst GRB 170817A was also detected by other gamma-ray telescopes after 1.7 seconds. This event

not only proved that short gamma-ray burst is generated by binary neutron stars, but also was a prelude to the multi-messenger astronomy era.

To understand the universe by gravitational waves, multiple detectors sensed to various wavelengths are required. KAGRA, the 3 kilometers Large-scale Cryogenic Gravitational wave Telescope (LCGT), is being constructed and planned to be operating in 2019 to join the detection of gravitational waves with LIGO and Virgo. There are two main features in KAGRA: it is constructed underground to prevent large seismic noise, and it employs cryogenic techniques to cool down the mirror in order to reduce thermal noise. Once KAGRA joins the gravitational wave research, we are able to detect gravitational waves and estimate the source parameters afterwards. Then one critical issue appears: How accurate could we estimate the parameters? Since the uncertainty of gravitational wave signals propagates to the uncertainty of estimate source parameters, calibration of the detector becomes a critical point.

For the second generation gravitational wave interferometers, the required $h(t)$ calibration accuracy is 1 percent in the current stage. To achieve this goal, Photon Calibrator (Pcal) is one of the calibration method used in current gravitational wave detectors. It uses auxiliary laser source, emits modulated photon pressure to give modulated forces to the surface of end test mass. The gravitational wave amplitude changes arm length of the interferometer, which can be regarded as modulating the end test mass position. By modulating the end test mass with Pcal, we are able to calibrate the relationship between the displacement of end test mass and the interferometer output by deriving the displacement of the end test mass by the absolute laser power. Besides, gravitational wave interferometers use feedback control loop to suppress noises. Photon Calibrator also allows us to calibrate the time-dependent parameters in the feedback control loop in order to measure the gravitational wave signal accurately.

There are two features in KAGRA Photon Calibrator: 20 watts laser and 2 Acousto-optic modulators (AOM).

1. **20 watts laser**:
   In LIGO Photon Calibrator, the maximum laser source is 2 watts, which takes time to generate calibration lines at high frequency. By increasing laser power to 20 watts, we are able to generate calibration lines at high-frequency region more easily.

2. **2 AOMs**: We send two modulated laser beam to minimize the elastic deformations on the mirror. LIGO Photon Calibrator uses one AOM and split the laser power into two beams afterwards. Two AOMs in the Pcal allow us to send two different

forces of the laser beam to the end test mass in order to mitigate the rotation effect of end test mass.

In this thesis, we introduce the development and characterization of KAGRA Photon Calibrator. In chapter 2, we introduce the theory of gravitational waves and the gravitational waves events which have been detected so far. In chapter 3, we explain the principle of gravitational wave interferometer and introduce KAGRA and other gravitational wave detectors in worldwide. In chapter 4, we give an overview of calibration method and introduce the KAGRA Photon Calibrator instrument and requirements. In chapter 5, we introduce the characterization of the optical system especially on the laser beam profile measurement and the mode matching. In chapter 6, we introduce a instrument called Optical Follower Servo (OFS) which is an active feedback controller used for power stabilization of Pcal. In chapter 7, we discuss the result of the integration test including Pcal, OFS, and digital system. In chapter 8, we discuss the noise of the Pcal and the future plan. Finally, the conclusion of this thesis is given in chapter 9.

Chapter 2

Gravitational Wave Science

2.1 Gravitational Wave Theory

2.1.1 Linearized Einstein Field Equation

The Einstein field equation is described as[1][2]

$$G_{\mu\nu} \equiv R_{\mu\nu} - \frac{1}{2} g_{\mu\nu} R = \frac{8\pi G}{c^4} T_{\mu\nu} \tag{2.1}$$

where $G_{\mu\nu}$ is called the Einstein tensor, $R_{\mu\nu}$ is the Ricci curvature tensor, $g_{\mu\nu}$ is the metric tensor, R is the Ricci scalar, G is the Newton's gravitational constant, c is the speed of light in vacuum, and $T_{\mu\nu}$ is the stress-energy tensor. Using geometrized units where $G = c = 1$, this can be written as

$$G_{\mu\nu} \equiv R_{\mu\nu} - \frac{1}{2} g_{\mu\nu} R = 8\pi T_{\mu\nu} \tag{2.2}$$

Since $G_{\mu\nu}$ and $T_{\mu\nu}$ are symmetric tensors, Eq. 2.2 should be regarded as ten coupled differential equations. Furthermore, Einstein field equations have the property called Bianchi identities:

$$G_{\mu\nu;\nu} = 0 \tag{2.3}$$

where the semi-colon denotes a covariant derivative. This identities mean that there four differential identities in the ten $G_{\mu\nu}$, so there are only six independent differential equations in ten Einstein equations, leaving the metric tensor with four degrees of freedom, which correspond to the freedom in choosing coordinates system.

Considering a weak gravitational field which space-time is nearly flat, the metric tensor can be written as

$$g_{\mu\nu} = \eta_{\mu\nu} + h_{\mu\nu} \tag{2.4}$$

where $\eta_{\mu\nu}$ is the metric in flat space-time

$$\eta_{\mu\nu} = \begin{pmatrix} -1 & 0 & 0 & 0 \\ 0 & 1 & 0 & 0 \\ 0 & 0 & 1 & 0 \\ 0 & 0 & 0 & 1 \end{pmatrix} \tag{2.5}$$

and

$$|h_{\mu\nu}| \ll 1 \tag{2.6}$$

everywhere in space-time.

2.1.1.1 The Christoffel symbols and curvature tensors

The Christoffel symbols in the linearized metric can be written as

$$\begin{aligned} \Gamma^{\mu}{}_{\alpha\beta} &= \frac{1}{2} g^{\mu\nu}(g_{\alpha\nu,\beta} + g_{\beta\nu,\alpha} - g_{\alpha\beta,\nu}) \\ &= \frac{1}{2} g^{\mu\nu}(h_{\alpha\nu,\beta} + h_{\beta\nu,\alpha} - h_{\alpha\beta,\nu}) \\ &= \frac{1}{2}(h^{\mu}{}_{\alpha,\beta} + h^{\mu}{}_{\beta,\alpha} - h_{\alpha\beta}{}^{,\mu}) \end{aligned} \tag{2.7}$$

To compute the Ricci tensor

$$R_{\mu\nu} = \Gamma^{\alpha}{}_{\mu\nu,\alpha} - \Gamma^{\alpha}{}_{\mu\alpha,\nu} - \Gamma^{\beta}{}_{\mu\alpha}\Gamma^{\alpha}{}_{\mu\beta} + \Gamma^{\beta}{}_{\mu\nu}\Gamma^{\alpha}{}_{\beta\alpha} \tag{2.8}$$

to the linear order, we can drop the "$\Gamma\Gamma$" terms and left with

$$\begin{aligned} R_{\mu\nu} &= \Gamma^{\alpha}{}_{\mu\nu,\alpha} - \Gamma^{\alpha}{}_{\mu\alpha,\nu} \\ &= \frac{1}{2}(h^{\alpha}{}_{\mu,\nu\alpha} + h^{\alpha}{}_{\nu,\mu\alpha} - h_{\mu\nu}{}^{,\alpha}{}_{\alpha} - h^{\alpha}{}_{\mu,\alpha\nu} - h^{\alpha}{}_{\alpha,\mu\nu} + h_{\mu\alpha}{}^{,\alpha}{}_{\nu}) \\ &= \frac{1}{2}(h^{\alpha}{}_{\nu,\mu\alpha} + h_{\mu\alpha}{}^{,\alpha}{}_{\nu} - h_{\mu\nu}{}^{,\alpha}{}_{\alpha} - h^{\alpha}{}_{\alpha,\mu\nu}) \end{aligned} \tag{2.9}$$

Using the notations

$$h \equiv h^{\alpha}{}_{\alpha} \tag{2.10}$$

$$\Box = \partial^{\mu}\partial_{\mu} = -\partial_t^2 + \nabla^2 \tag{2.11}$$

, then the Ricci tensor becomes

$$R_{\mu\nu} = \frac{1}{2}(h^{\alpha}{}_{\nu,\mu\alpha} + h_{\mu\alpha}{}^{,\alpha}{}_{\nu} - \Box h_{\mu\nu} - h_{,\mu\nu}). \tag{2.12}$$

and for the Ricci scalar we have

$$\begin{aligned} R &= \eta^{\mu\nu} R_{\mu\nu} \\ &= \frac{1}{2}(h^{\alpha\mu}{}_{,\alpha\mu} + h_{\mu\alpha}{}^{,\alpha\mu} - \Box h - \Box h) \\ &= h^{\mu\nu}{}_{,\mu\nu} - \Box h \end{aligned} \tag{2.13}$$

The Einstein equation can be written as

$$\begin{aligned} G_{\mu\nu} &= R_{\mu\nu} - \frac{1}{2}\eta_{\mu\nu} R \\ &= \frac{1}{2}(h^{\alpha}{}_{\nu,\mu\alpha} + h_{\mu\alpha}{}^{,\alpha}{}_{\nu} - \Box h_{\mu\nu} - h_{,\mu\nu} - \eta_{\mu\nu} h^{\alpha\beta}{}_{,\alpha\beta} + \eta_{\mu\nu}\Box h) \end{aligned} \tag{2.14}$$

Finally, we can derive the linearized Einstein field equation

$$h^{\alpha}{}_{\nu,\mu\alpha} + h_{\mu\alpha}{}^{,\alpha}{}_{\nu} - \Box h_{\mu\nu} - h_{,\mu\nu} - \eta_{\mu\nu} h^{\alpha\beta}{}_{,\alpha\beta} + \eta_{\mu\nu}\Box h = 16\pi T_{\mu\nu} \tag{2.15}$$

2.1.1.2 The trace reverse of $h_{\mu\nu}$

Since Eq. 2.15 is a little bit complicated, here we define a variable called 'trace reverse' of $h_{\mu\nu}$

$$\bar{h}_{\mu\nu} \equiv h_{\mu\nu} - \frac{1}{2}\eta_{\mu\nu} h, \tag{2.16}$$

$$\bar{h} \equiv \bar{h}^{\mu}{}_{\mu} = -h \tag{2.17}$$

The inverse of Eq. 2.16 is the same:

$$h_{\mu\nu} = \bar{h}_{\mu\nu} - \frac{1}{2}\eta_{\mu\nu}\bar{h} \tag{2.18}$$

Then Eq. 2.15 can be written as

$$\begin{aligned} \bar{h}^{\alpha}{}_{\nu,\mu\alpha} - \frac{1}{2}\bar{h}_{,\mu\nu} + \bar{h}_{\mu\alpha}{}^{,\alpha}{}_{\nu} - \frac{1}{2}\bar{h}_{,\mu\nu} - \Box\bar{h}_{\mu\nu} + \frac{1}{2}\eta_{\mu\nu}\Box\bar{h} - \bar{h}_{,\mu\nu} + 2\bar{h}_{,\mu\nu} \\ - \eta_{\mu\nu}\bar{h}^{\alpha\beta}{}_{,\alpha\beta} + \frac{1}{2}\eta_{\mu\nu}\Box\bar{h} + \eta_{\mu\nu}\Box\bar{h} - 2\eta_{\mu\nu}\Box\bar{h} = 16\pi T_{\mu\nu} \end{aligned} \tag{2.19}$$

, and we can simpified the equation with only 4 terms on the left-hand side:

$$\bar{h}^{\alpha}{}_{\nu,\mu\alpha} + \bar{h}_{\mu\alpha}{}^{,\alpha}{}_{\nu} - \Box\bar{h}_{\mu\nu} - \eta_{\mu\nu}\bar{h}^{\alpha\beta}{}_{,\alpha\beta} = 16\pi T_{\mu\nu} \tag{2.20}$$

2.1.1.3 Gauge transformation

If there is a very small change in coordinates of the form

$$x^{\mu'} = x^{\mu} + \xi^{\mu}(x^{\nu}) \tag{2.21}$$

, and we demand ξ^{α} be small such that $|\xi^{\alpha}{}_{,\beta}| \ll 1$, then we have

$$\Lambda^{\mu'}{}_{\nu} = \frac{\partial x^{\mu'}}{\partial x^{\nu}} = \delta^{\mu}{}_{\nu} + \xi^{\mu}{}_{,\nu}, \tag{2.22}$$

$$\Lambda^{\mu}{}_{\nu'} = \delta^{\mu}{}_{\nu} - \xi^{\mu}{}_{,\nu} + O(|\xi^{\mu}{}_{,\nu}|^2). \tag{2.23}$$

The Lorentz transformation for the metric tensor is

$$\begin{aligned} g_{\mu'\nu'} &= \Lambda^{\alpha}{}_{\mu'}\Lambda^{\beta}{}_{\nu'}g_{\alpha\beta} \\ &= (\delta^{\alpha}{}_{\mu} - \xi^{\alpha}{}_{,\mu})(\delta^{\beta}{}_{\nu} - \xi^{\beta}{}_{,\nu})g_{\alpha\beta} \\ &= g_{\mu\nu} - \xi^{\alpha}{}_{,\mu}g_{\alpha\nu} - \xi^{\beta}{}_{,\nu}g_{\mu\beta} + \xi^{\alpha}{}_{,\mu}\xi^{\beta}{}_{,\nu}g_{\alpha\beta} \end{aligned} \tag{2.24}$$

We can neglect the last term since it is the second order term

$$\begin{aligned} g_{\mu'\nu'} &= \eta_{\mu'\nu'} + h_{\mu'\nu'} \\ &= \eta_{\mu\nu} + h_{\mu\nu} - \xi_{\nu,\mu} - \xi_{\mu,\nu} \end{aligned} \tag{2.25}$$

Therefore, we get

$$h_{\mu'\nu'} = h_{\mu\nu} - \xi_{\nu,\mu} - \xi_{\mu,\nu} \tag{2.26}$$

and the trace reversed $h_{\mu\nu}$ is

$$\begin{aligned} \bar{h}_{\mu'\nu'} &= h_{\mu'\nu'} - \frac{1}{2}\eta_{\mu'\nu'}h^{\mu'}{}_{\mu'} \\ &= h_{\mu\nu} - \xi_{\nu,\mu} - \xi_{\mu,\nu} - \frac{1}{2}\eta_{\mu\nu}(h^{\mu}{}_{\mu} - \xi^{\mu}{}_{,\mu} - \xi^{\mu}{}_{,\mu}) \\ &= \bar{h}_{\mu\nu} - \xi_{\nu,\mu} - \xi_{\mu,\nu} + \eta_{\mu\nu}\xi^{\alpha}{}_{,\alpha} \end{aligned} \tag{2.27}$$

Taking divergence of Eq. 2.27 gives

$$\bar{h'}^{\mu\nu}{}_{,\nu} = \bar{h}^{\mu\nu}{}_{,\nu} - \xi^{\nu,\mu}{}_{\nu} - \xi^{\mu,\nu}{}_{,\nu} + \eta^{\mu\nu}\xi^{\alpha}{}_{,\alpha\nu} = \bar{h}^{\mu\nu}{}_{,\nu} - \Box\xi^{\mu} \tag{2.28}$$

The transform system is in Lorentz gauge $\bar{h'}^{\mu\nu}{}_{,\nu} = 0$ if we could select $\Box\xi^{\mu} = \bar{h}^{\mu\nu}{}_{,\nu}$. Since $\Box f = g$ is the three-dimensional inhomogenous wave equation, and it always has a solution for any g, therefore we can always find some ξ^{μ} which transform arbitrary $h_{\mu\nu}$ to the Lorentz gauge.

Therefore, in the Lorentz gauge, the linearized Einstein Eq. 2.20 becomes simply

$$\Box\bar{h}_{\mu\nu} = -16\pi T_{\mu\nu} \tag{2.29}$$

2.1.2 Gravitational Waves

The Einstein equation Eq. 2.29 in vacuum

$$\left(-\frac{\partial^2}{\partial t^2} + \nabla^2\right)\bar{h}_{\mu\nu} = 0 \tag{2.30}$$

, is called three-dimensional wave equation. It has the solution of the form

$$\bar{h}_{\mu\nu} = A_{\mu\nu}\exp(ik_{\alpha}x^{\alpha}) \tag{2.31}$$

Substituting Eq. 2.31 to Eq. 2.30, we can get

$$k^{\mu}k_{\mu} = 0 \tag{2.32}$$

and the Lorentz gauge $\bar{h}^{\mu\nu}{}_{,\nu} = 0$ give us that

$$A^{\mu\nu}k_{\mu} = 0. \tag{2.33}$$

This is the first constraint on the amplitude $A_{\mu\nu}$. We can use the gauge freedom to restrict it further. Introducting a gauge by solving $\Box\xi_{\mu} = 0$, we can get

$$\xi_{\mu} = \Re\left(iB_{\mu}e^{ik_{\alpha}x^{\alpha}}\right) \tag{2.34}$$

Substituting Eq. 2.31 and Eq. 2.34 into Eq. 2.27, we can get the gravitational wave amplitude changes by

$$A'_{\mu\nu} = A_{\mu\nu} + k_{\mu}B_{\nu} + k_{\nu}B_{\mu} - \eta_{\mu\nu}k_{\alpha}B^{\alpha} \tag{2.35}$$

We can choose the B_{μ} to impose two further restrictions on $A'_{\mu\nu}$

$$\begin{aligned} A^{\alpha}{}_{\alpha} &= 0 \\ A_{0i} &= 0 \end{aligned} \tag{2.36}$$

Eq. 2.33 and Eq. 2.36 are called *transverse-traceless*(TT) gauge. Since $A_{\mu\nu}$ is a symmetric tensor which has 10 degrees of freedom and there are 8 constraints on it, therefore there are 2 remaining polarizations of gravitational waves. These restrictions on $A_{\mu\nu}$ gives

$$A^{\mathrm{TT}}_{\mu\nu} = \begin{pmatrix} 0 & 0 & 0 & 0 \\ 0 & A_+ & A_\times & 0 \\ 0 & A_\times & -A_+ & 0 \\ 0 & 0 & 0 & 0 \end{pmatrix} \tag{2.37}$$

where A_+ and $A_\times$ are two directions of gravitational wave polarizations. The effect of two polarizations is shown in Fig. 2.1.

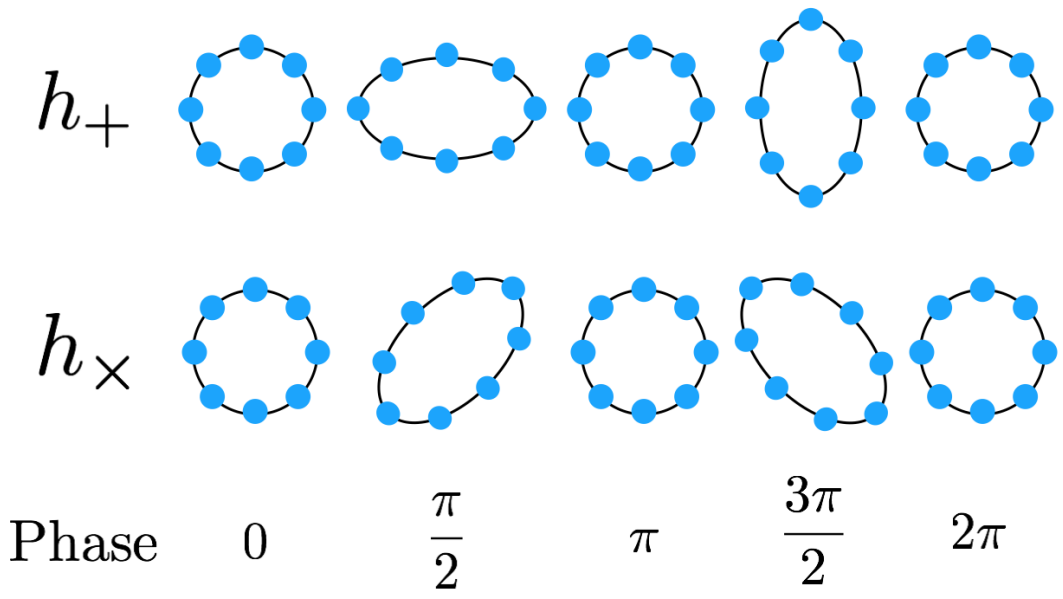

FIGURE 2.1: The effect of gravitaional waves act on free particles. The upper part shows the "+" polarization and lower part shows the "×" polarization.

2.1.3 The effect of gravitational waves on free particles

Consider a particle initially in a flat space-time encounters a gravitational wave. Choose a Lorentz frame which the particle is initially at rest, and choose the TT gauge referred to this frame. Then a free particle follows the geodesic equation

$$\frac{\mathrm{d}}{\mathrm{d}\tau}U^\mu + \Gamma^\mu{}_{\alpha\beta}U^\alpha U^\beta = 0 \tag{2.38}$$

Since the particle is initially at rest, the initial value of the acceleration is

$$\left(\frac{\mathrm{d}U^\mu}{\mathrm{d}\tau}\right)_0 = -\Gamma^\mu{}_{00} = \frac{1}{2}\eta^{\mu\nu}(h_{\nu 0,0} + h_{0\nu,0} - h_{00,\nu}) \tag{2.39}$$

From Eq. 2.37, $h^{\mathrm{TT}}_{\nu 0,0} = 0$, so the initial acceleration vanishes. Since the particle is initially at rest, it remains at a constant coordinate even if a gravitational wave comes. But all we know is that by choosing TT gauge we can find a coordinate system which makes corresponding particle stay at the same coordinate.

Now consider two nearby particles, one at the origin and the other at $(x, y, z) = (\varepsilon, 0, 0)$, both are initially at rest. Then the proper distance between them is

$$\begin{aligned} \Delta l \equiv \int |\mathrm{d}s|^{1/2} &= \int |g_{\mu\nu}\mathrm{d}x^{\mu}\mathrm{d}x^{\nu}|^{1/2} \\ &= \int_0^{\varepsilon} |g_{xx}|^{1/2} \\ &\approx |g_{xx}(x=0)|^{1/2}\varepsilon \\ &\approx \left(1 + \frac{1}{2}h^{\mathrm{TT}}_{xx}(x=0)\right)\varepsilon \end{aligned} \tag{2.40}$$

Since h^{TT}_{xx} is not generally zero, the proper distance between two particles change with time, and it is proportional to the initial distance ε. If the original distance between two particles are longer, then gravitational waves give a bigger distance change. That is the reason why the modern ground-based gravitational wave interferometers(e.g. LIGO, Virgo and KAGRA) are built in km-scales, and the space-based interferometers are planned to built in million km-scales. Furthermore, from Eq. 2.40, the distance change is proportional to h^{TT}_{ij}, which are the small number around 10^{-21} or smaller. Therefore, the gravitational wave detectors should have the sensitivity higher than 10^{-21}.

2.2 Source of Gravitational Waves

2.2.1 Compact Binary Coalescence (CBC)

The gravitational waves which have been detected by LIGO and VIRGO so far are from CBC [3][4]. CBC gravitational waves are generated by orbiting pair of massive and compact objects, like black holes and neutron stars. It can be categorized into three categories:

1. Binary Black Hole (BBH)
2. Binary Neutron Star (BNS)
3. Neutron Star-Black Hole Binary (NSBH)

There are three stages in CBC lifecycle: inspiral, merger, and ringdown (Fig. 2.2). In the inspiral stage, when two of these compact object orbit against each other, they emit

gravitational waves, which take the energy off from the system's orbital energy and make them closer and closer. Moving closer makes them orbit each other faster, which cause them to lose more orbital energy. Therefore, frequency from gravitational wave signal from CBC increases while measuring time increases, which is called chirp signal. When two black holes are close enough, they start to merge, emitting peaks at this stage. Once merged, the single black hole settles down to a stable form via ringdown stage. The distortion from the spherical shape reduces rapidly by emitting gravitational waves until the stable sphere is present.

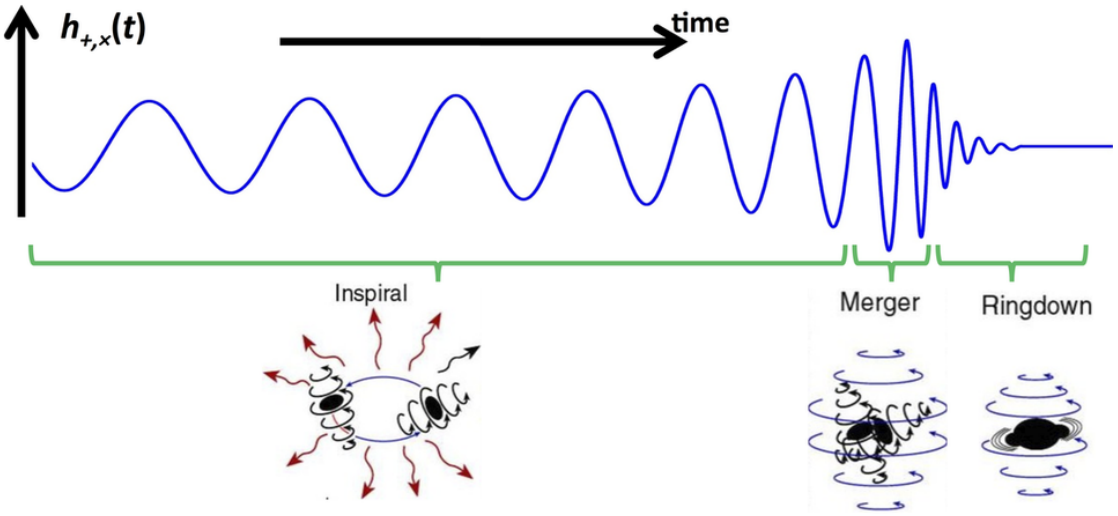

FIGURE 2.2: Compact binary coalescence [5]

The angular frequency in the inspiral system is given by

$$\dot{\omega} = \left(\frac{96}{5}\right)\left(\frac{G\mathcal{M}}{c^3}\right)^{\frac{5}{3}}\omega^{\frac{11}{3}} \tag{2.41}$$

[6]. $\mathcal{M}$ is the chirp mass given by

$$\mathcal{M} = \mu^{\frac{3}{5}}M^{\frac{2}{5}} \tag{2.42}$$

where M is the total mass and μ is the reduced mass of the binary system given by

$$\mu = \frac{M_1 M_2}{M_1 + M_2} \tag{2.43}$$

where M_1 and M_2 are the masses of binary system. This equation shows the characteristic of chirp signal: the orbital frequency increase when orbital distance decreases. Integrating Eq. 2.41 gives the frequency of the gravitational waves in function of time:

$$f = \frac{5^{\frac{3}{8}}}{8\pi}\left(\frac{G\mathcal{M}}{c^3}\right)^{-\frac{5}{8}}(t_c - t)^{-\frac{3}{8}} \tag{2.44}$$

, where t_c is the time when two objects merge. If the chirp signal can be detected, we can calculate the chirp mass of the binary system. Using chirp mass and amplitude of gravitational wave signal, the distance between binary system to earth could be calculated, and the Hubble constant or other cosmological constant can be measured.

2.2.1.1 Binary black holes

The first detection of gravitational waves detected in September 14, 2015, is from binary black holes, which is called GW150914 [7]. This gravitational waves is formed by binary black holes whose mass are 36 and 29 solar masses. Two black holes merged, ringdown to a single blackhole which is evaluated to 62 solar masses and emitted gravitational waves with energy of 3 solar masses. Beside first detection, there were 4 more gravitational waves detection generated by binary black holes: GW 151226[8], GW170104 [9], GW170608 [10], GW170814 [11]. The detection of gravitational waves formed by binary black hole merger proves that strong gravitational field event generates gravitational waves.

2.2.1.2 Binary neutron stars

In August 17, 2017, a gravitational wave signal GW170817 generated by binary neutron star merger with a total mass around 2.82 solar masses was observed by LIGO and Virgo [12]. This gravitational wave signal continued about 100 second in the detectable frequency range, , increasing from 24 hertz to few hundred hertz. 1.7 seconds after merging time, a electromagnetic wave signal GRB 170817A, a short gamma ray burst, was detected by Fermi Gamma ray Space Telescope [13]. More than 70 observatories coving all the electromagnetic spectrum observed this event. This detection proves that binary neutron star merger exists, and it will generate short gamma ray burst and kilonova. It is also a first event which connected the observation of gravitational waves with other astronomical fields.

2.2.1.3 Neutron star-Black hole binary

There is no detection of NS-BS merger so far, but in the future we can detect the following event and evaluate the event rate. We can obtain the new information about universe and general relativity.

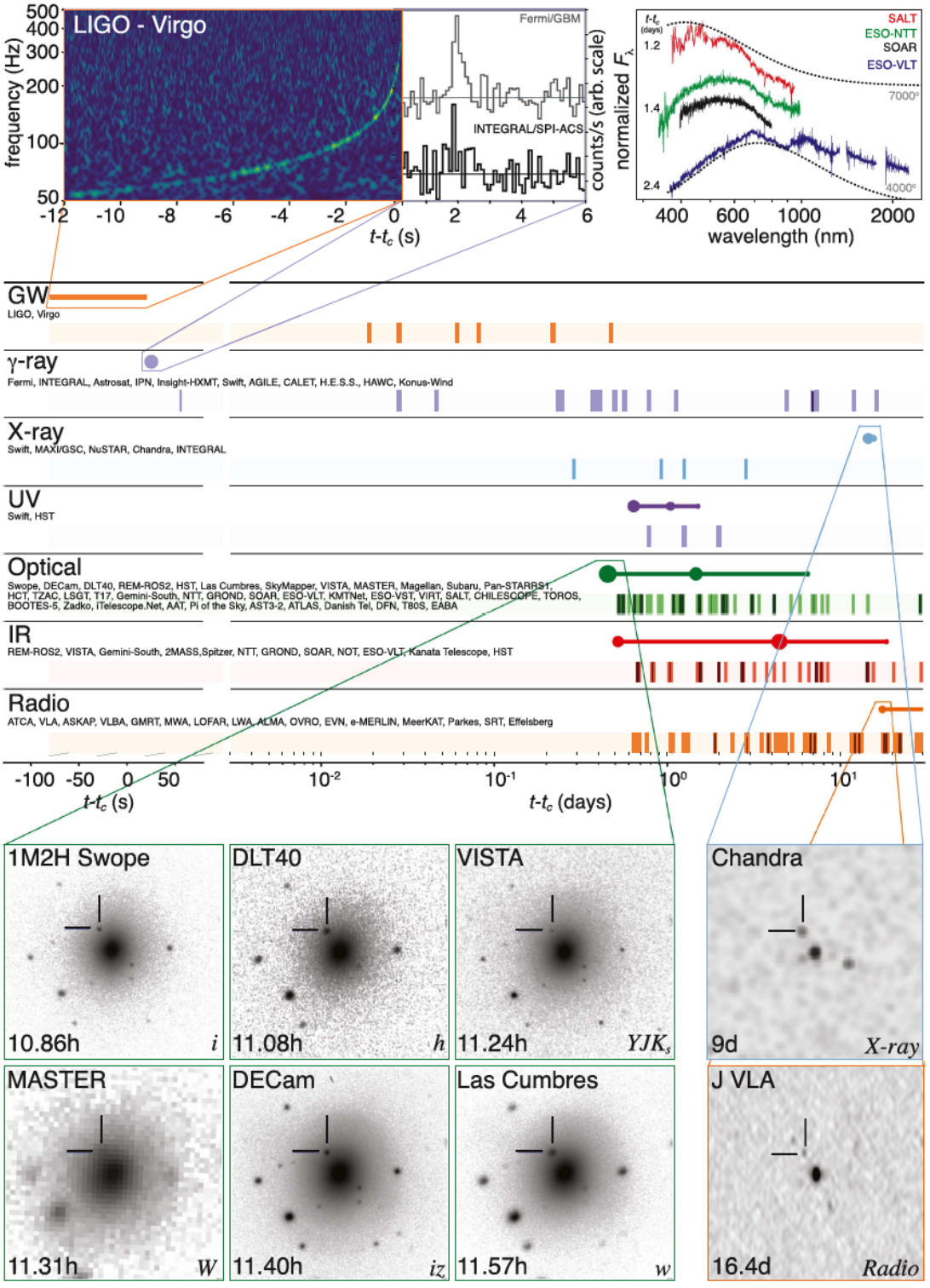

FIGURE 2.3: Multimessenger observation of a Binary Neutron Star Merger [13]. The Gamma ray is observed 1.7 seconds after the binary black hole merger. Over the following days and weeks, many telescopes in different wavelengths observed the debris which was ejected from binary neutron star.

2.2.2 Continuous Wave (CW)

Continuous waves are generated from a single spinning massive object like neutron star. To generate gravitational waves, the spherical asymmetry in neutron star is required, which gives the star quadrupole moment changing with time to emit gravitational waves. This kind of gravitational waves is continuously the same frequency and same amplitude, therefore, it is called continuous wave.

2.2.3 Supernovae and gravitational collapse

Supernova is a transient astronomical event which occurs in the final of the life of massive star. Neutron stars or black holes are generated from gravitation collapse of supernovae. Since gravitational collapse is usually not symmetry, then there will be a change of quadrupole moment which generate gravitational waves. A supernovae event happens once in decades in our galaxy, and the exact explosion mechanism is still not fully understood.

2.2.4 Stochastic gravitational waves

In the early Universe, many models shows that there was inflation which space expanded in a very short time. If the expansion was not symmetry, it may have emitted gravitaional waves. These gravitational waves rarely decayed or scatted, which may be detected today as a stochastic background of gravitational waves. This background signal is too weak for any currently operational gravitational wave detector to observe. Cosmic Microwave Background can only investigate the universe from 10^5 years after Big Bang. If stochastic gravitational waves could be detected, we may be able to understand the universe up to 10^{-30} seconds [14].

2.3 Detected Events and Parameter Estimation

So far five binary black hole events (GW150914, GW151226, GW170104, GW170608, GW170814) and one binary neutron star event (GW170817) have been detected by LIGO and Virgo [7][8][15][9][10][11][12]. We summarized the estimate source parameters from each event from binary black hole merger arrevents in Table. 2.1 and Fig. 2.4, and binary neutron star merger event in Table. 2.2.

	GW 150914	GW 151226	GW 170104	GW 170608	GW 170814
Signal to noise ratio ρ	23.7	13.0	13	13	18
Primary BH mass m_1 $[M_\odot]$	$36.2^{+5.2}_{-3.8}$	$14.2^{+8.3}_{-3.7}$	$31.2^{+8.4}_{-6.0}$	12^{+7}_{-2}	$30.5^{+5.7}_{-3.0}$
Secondary BH mass m_2 $[M_\odot]$	$29.1^{+3.7}_{-4.4}$	$7.5^{+2.3}_{-2.3}$	$19.4^{+5.3}_{-5.9}$	7^{+2}_{-2}	$25.3^{+2.8}_{-4.2}$
Final black hole mass m_f $[M_\odot]$	$62.3^{+3.7}_{-3.1}$	$20.8^{+6.1}_{-1.7}$	$48.7^{+5.7}_{-4.6}$	$18.0^{+4.8}_{-0.9}$	$55.9^{+3.4}_{-2.7}$
Radiatied energy E_{rad} $[M_\odot c^2]$	$3.0^{+0.5}_{-0.4}$	$1.0^{+0.1}_{-0.2}$	$2.0^{+0.6}_{-0.7}$	$0.85^{+0.06}_{-0.17}$	$2.7^{+0.4}_{-0.3}$
Final black hole spin a_f	$0.68^{+0.05}_{-0.06}$	$0.74^{+0.06}_{-0.06}$	$0.64^{+0.09}_{-0.20}$	$0.69^{+0.04}_{-0.05}$	$0.70^{+0.07}_{-0.05}$
Luminosity distance D_L [Mpc]	420^{+150}_{-180}	440^{+180}_{-190}	880^{+450}_{-390}	340^{+140}_{-140}	540^{+130}_{-210}
Source redshift z	$0.09^{+0.03}_{-0.04}$	$0.09^{+0.03}_{-0.04}$	$0.18^{+0.08}_{-0.07}$	$0.07^{+0.03}_{-0.03}$	$0.11^{+0.03}_{-0.04}$
Peak luminosity $\ell_{\rm peak}[10^{56}{\rm erg/s}]$	$3.6^{+0.5}_{-0.4}$	$3.3^{+0.8}_{-1.6}$	$3.1^{+0.7}_{-1.3}$	$3.4^{+0.5}_{-1.6}$	$3.7^{+0.5}_{-0.5}$
Source localization $\Delta\Omega$ $[{\rm deg}^2]$	230	850	1200	860	60

TABLE 2.1: Parameters of gravitational waves from binary black hole merger

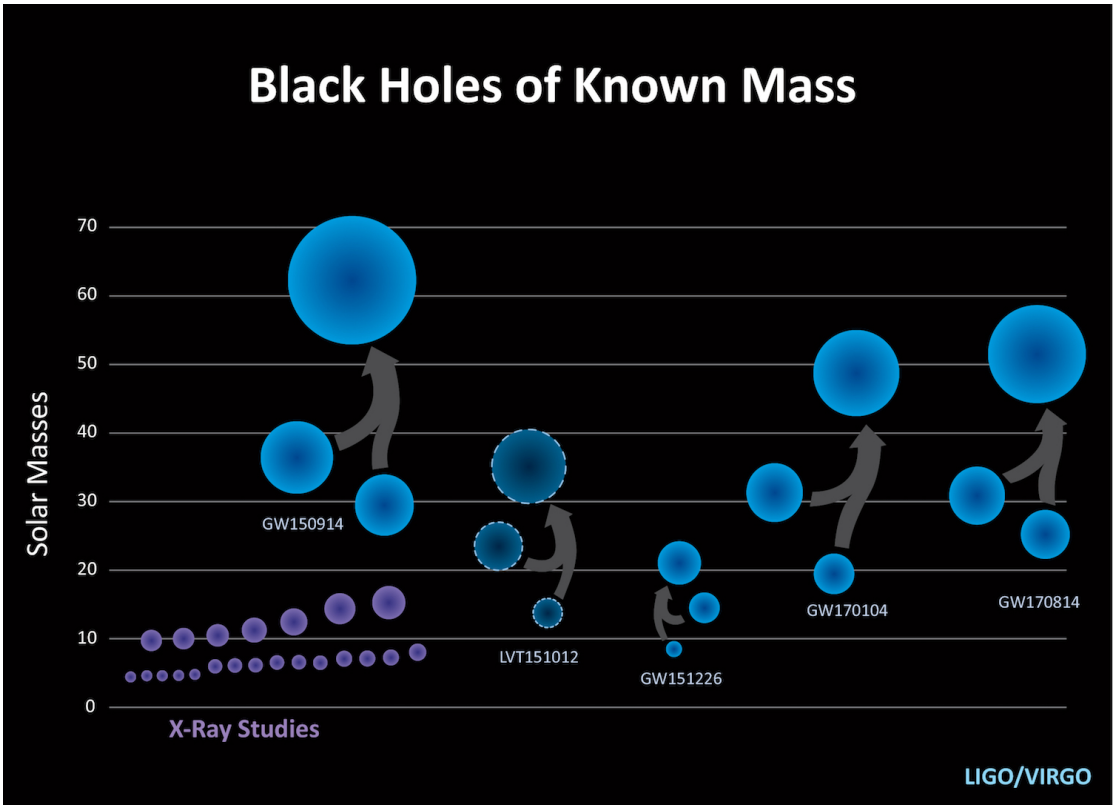

FIGURE 2.4: Binary black hole merger [4]

First four binary black hole events were detected only by LIGO. GW170814 and GW170817 were detected by LIGO and Virgo simultaneously. We can find that the source localization in two event detected by LIGO and Virgo were better than other events. In

	GW 170814
Signal to noise ratio ρ	32.4
Primary NS mass m_1 $[M_\odot]$	$1.36 - 2.26$
Secondary NS mass m_2 $[M_\odot]$	$0.86 - 1.36$
Total NS mass m_f $[M_\odot]$	$2.82^{+0.47}_{-0.09}$
Radiatied energy E_{rad} $[M_\odot c^2]$	> 0.025
Luminosity distance D_L [Mpc]	40^{+8}_{-14}
Source redshift z	$0.11^{+0.03}_{-0.04}$
Peak luminosity $\ell_{\rm peak}[10^{56}{\rm erg/s}]$	$3.7^{+0.5}_{-0.5}$
Source localization $\Delta\Omega$ [deg^2]	28
Hubble constant [km/s Mpc]	$70.0^{+12.0}_{-8.0}$

TABLE 2.2: Parameters of gravitational waves from binary neutron star merger

GW170814 events, the sky localization reduced from 1160 deg^2 using only two detectors to 60 deg^2 using all three detectors. By including KAGRA in the future, a source of gravitational wave signal will be localized to a few square degrees [16]. In order to accurately estimate these parameters from gravitational wave signals, calibration of the detectors play an important role. The absolute calibration of each detectors corresponds to the estimated source distance and the other parameters in CBC, and the relative calibration between each detectors corresponds to the estimated source localization. Therefore, we need to work on accurate calibration of gravitational wave signals in order to estimate the CBC parameters and further physical parameters accurately.

2.4 Summary

In this chapter, first we use weak field approach in Einstein equation and get the linearized Einstein equation. Gravitational wave can be derived from the linearized Einstein equation, and we showed that there are two polarization directions. Then we derived that the displacement change by gravitational wave is proportional to original distance, therefore we need a large scale gravitational wave detector to enlarge the displacement change. Next we introduced the various source of gravitational waves. Finally, we showed the parameters from gravitational wave event which have been detected so far, and explain the accurate calibration is important to determine the error of estimated physical parameters.

Chapter 3

Gravitational Wave detectors

3.1 Gravitational Wave Interferometer

3.1.1 Michelson interferometer

Michelson interferometer use a beam splitter to split a laser beam into two orthogonal beams which emit along x-axis and y-axis. There are two mirrors placed at each axis. Two beams which are reflected by mirror meet at beam splitter again, interfere with each other, and the interfered signal is detected by a photodetector. Fig. 3.1 shows the schematic of the Michelson interferometer.

Consider a gravitational wave whose polarization direction is "+" mode. The line element can be written as

$$ds^2 = -c^2dt^2 + (1 + h_+(t))dx^2 + (1 - h_+(t))dy^2 + dz^2 \tag{3.1}$$

where h_+ is the amplitude of gravitational wave in "+" mode depending on time. Since for the light, $ds^2 = 0$, the infinitesimal distance in x is

$$dx = \pm\frac{c}{\sqrt{1 + h_+(t)}}dt^2 \approx \left(1 - \frac{1}{2}h_+(t)\right)cdt \tag{3.2}$$

Assume the time which light travels back and forth from beam splitter to mirror is τ_x. Integrating Eq. 3.2 we can get

$$\begin{aligned} \frac{2L_x}{c} &= \int_{t-\tau_x}^{t} \left(1 - \frac{1}{2}h_+(t)\right)dt \\ \Longrightarrow \tau_x &= \frac{2L_x}{c} + \frac{1}{2}\int_{t-\tau_x}^{t} h_+(t)dt \end{aligned} \tag{3.3}$$

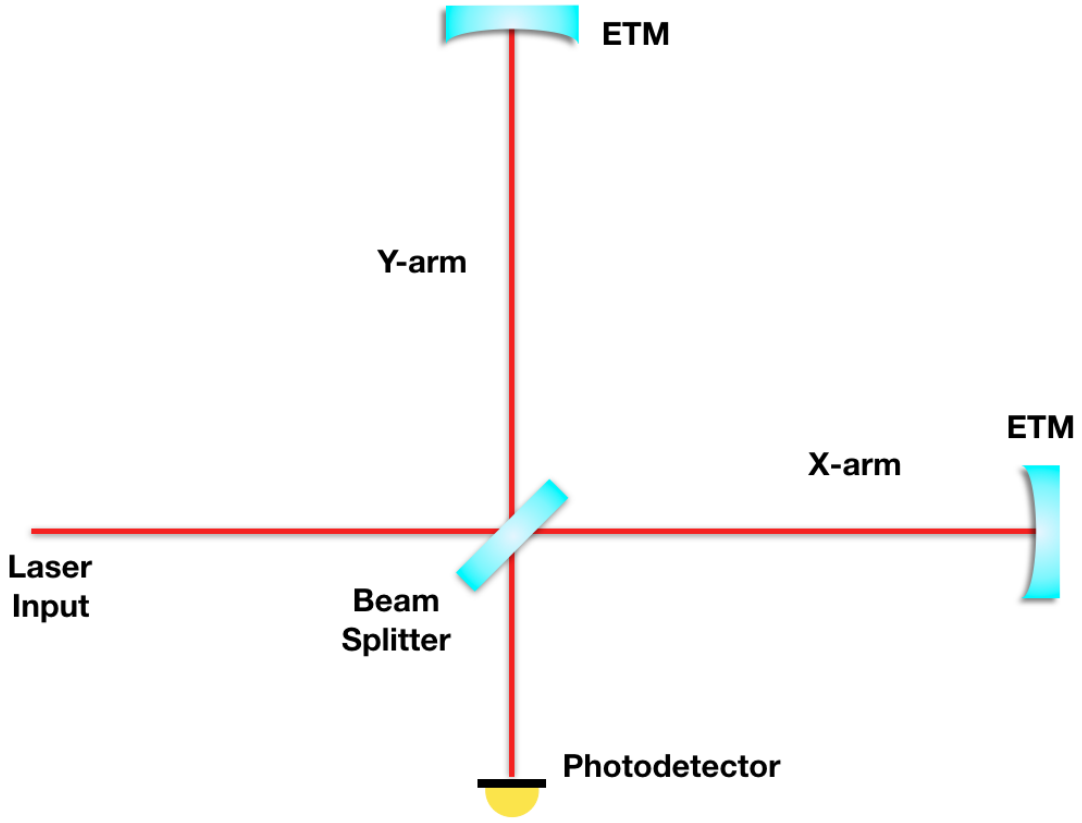

FIGURE 3.1: Michelson interferometer

Consider $h \ll 1$ is small, and we can approximate $\tau_x \approx 2Lx/c$. Then the phase difference after emitting back and forth from beam splitter to mirror in x-axis is

$$\phi_x = \Omega\tau_x \approx \Omega\frac{2L_x}{c} + \frac{\Omega}{2}\int_{t-\frac{2L_x}{c}}^{t} h_+(t)dt \tag{3.4}$$

where Ω is the frequency of the laser. Similarly, the phase difference in y-axis is

$$\phi_y = \Omega\tau_y \approx \Omega\frac{2L_y}{c} - \frac{\Omega}{2}\int_{t-\frac{2L_y}{c}}^{t} h_+(t)dt \tag{3.5}$$

Combining two laser beams in x-axis and y-axis, the phase difference between two axis is

$$\begin{aligned}\phi = \phi_x - \phi_y &= \Omega\frac{2(L_x - L_y)}{c} + \frac{\Omega}{2}\int_{t-\frac{2L_x}{c}}^{t} h_+(t)dt + \frac{\Omega}{2}\int_{t-\frac{2L_y}{c}}^{t} h_+(t)dt \\ &= \Omega\frac{2(L_x - L_y)}{c} + \Delta\phi_{GW}\end{aligned} \tag{3.6}$$

If the both arm are same length $L_x = L_y = L$, the phase difference generated by gravitational waves is

$$\Delta\phi_{GW} = \Omega \int_{t-\frac{2L}{c}}^{t} h_+(t)dt \tag{3.7}$$

Consider the frequency response of Michelson interferometer, the Fourier transform of $h_+(t)$ is

$$h_+(t) = \int_{-\infty}^{\infty} h(\omega)\mathrm{e}^{i\omega t}d\omega \tag{3.8}$$

, where ω is the angular frequency of gravitational wave signal. Substitute Eq. 3.8 into Eq. 3.7, the phase difference can be described as

$$\begin{aligned}\Delta\phi_{GW} &= \Omega \int_{t-\frac{2L}{c}}^{t} \int_{-\infty}^{\infty} h(\omega)\mathrm{e}^{i\omega t}d\omega dt \\ &= \int_{-\infty}^{\infty} \frac{2\Omega}{\omega}\mathrm{e}^{i\omega(t-\frac{L}{c})} \sin\left(\frac{\omega L}{c}\right) h(\omega)d\omega \\ &= \int_{-\infty}^{\infty} H_{MI}(\omega)h(\omega)d\omega\end{aligned} \tag{3.9}$$

where

$$H_{MI}(x) = \frac{2\Omega}{\omega}\mathrm{e}^{i\omega(t-\frac{L}{c})} \sin\left(\frac{\omega L}{c}\right) \tag{3.10}$$

is the frequency response function of Michelson interferometer. The frequency response function has the maximum value when

$$\frac{\omega L}{c} = \frac{\pi}{2} \tag{3.11}$$

. That is,

$$L = \frac{c}{4f} \tag{3.12}$$

Therefore, for a gravitational wave whose frequency is 100 Hz, the optimum length L of the Michelson interferometer is 750 km. Since it is difficult to built a such large interferometer on the ground, there are two different ways to enlarge the effective base line length. The one is delay-line method and the other is Fabry-Perot cavity method. Since the noise of delay-line method is higher than Fabry-Perot method, current gravitational wave detectors use Fabry-Perot cavity to increase the length of light path.

3.1.2 Fabry-Perot Michelson Interferometer

Fabry-Perot Michelson interferometer use two additional mirrors to form two Fabry-Perot cavities. Fig. 3.2 shows the configuration of Fabry-Perot Michelson interferometer. When the input laser beam emits into Fabry-Perot cavities, it reflects several times inside the cavity and then output to the beam splitter again, which increases the effective baseline length. The reflection times inside the Fabry-Perot cavity correspond to the "Finesse" of Fabry-Perot cavity. The "Finesse" $\mathcal{F}$ is defined as

$$\mathcal{F} = \frac{\pi\sqrt{r_{\mathrm{I}} r_{\mathrm{E}}}}{1 - r_{\mathrm{I}} r_{\mathrm{E}}} \tag{3.13}$$

where r_{I} and r_{E} are the reflectivity of Initial Test Mass (ITM) and End Test Mass (ETM), and the effective reflect times N inside the Fabry-Perot cavity is

$$N = \frac{2\mathcal{F}}{\pi} \tag{3.14}$$

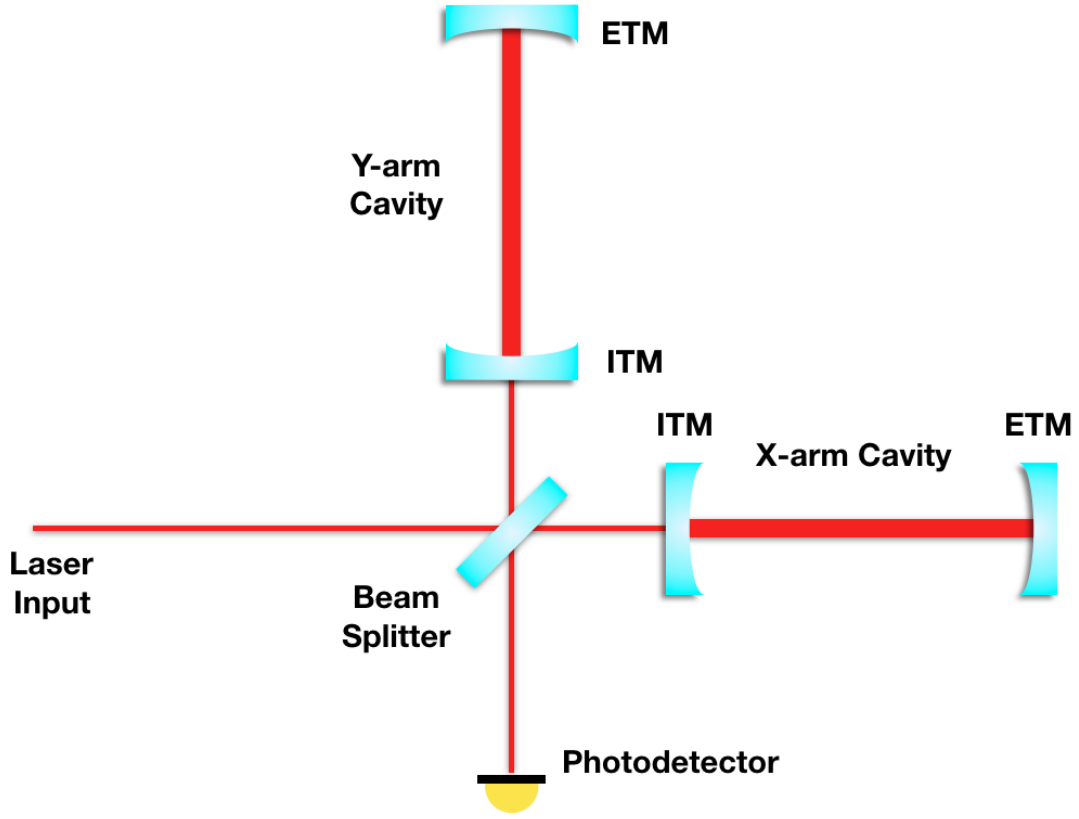

FIGURE 3.2: Fabry-Perot Michelson Interferometer

3.2 KAGRA experiment

3.2.1 Large-scale Cryogenic Gravitational-wave Telescope (LCGT)

The Large-scale Cryogenic Gravitational-wave Telescope called KAGRA is a underground gravitational wave interferometer located in Kamioka, Gifu, Japan. The arm length of KAGRA is 3 kilometers.

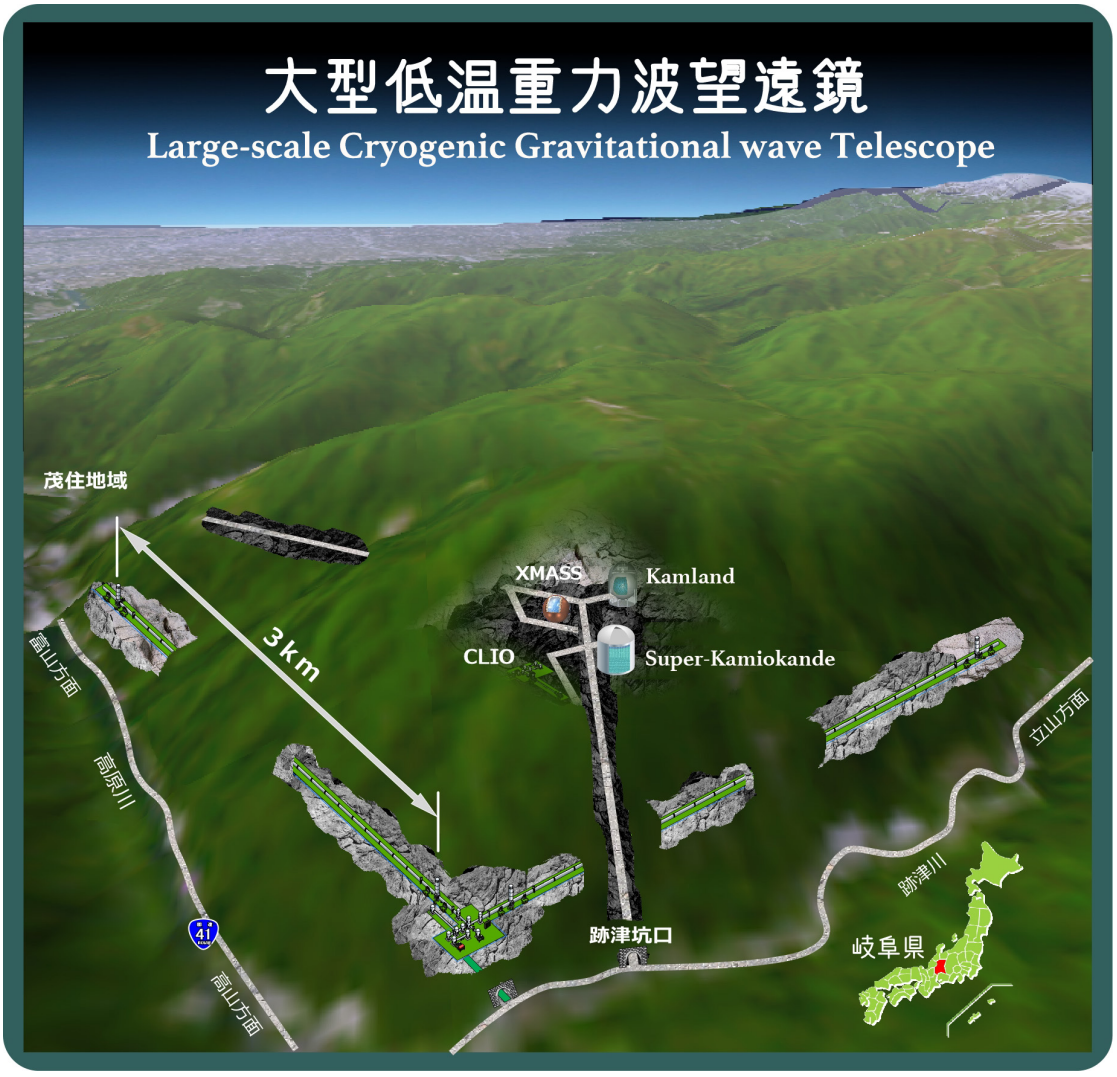

FIGURE 3.3: Large-scale Cryogenic Gravitational-wave Telescope (KAGRA) [17]

There are two main features in KAGRA:

1. **Underground:** The reason why KAGRA is constructed underground in Kamioka site is to reduce seismic noise with stable environment. In Kamioka, the seismic noise on the ground is 100 times smaller than the suburb near Tokyo due to less human activities, and the seismic noise will attenuate more in underground.

2. **Cryogenic mirrors:**
   When the high power laser emits to the mirror, it generates large heat on the mirror surface, which cause the thermal noise on the mirror. To reduce the thermal noise of the mirror, KAGRA mirrors are cooled down to 20K, and the material sapphire which has high Q value in cryogenic temperature is chosen for the mirror. Heat is transfered from sapphire mirror surface to the ear of mirror, and then transferred out using 4 sapphire fibers.

3.2.2 Designed sensitivity

The designed sensitivity of KAGRA is shown in Fig. 3.4. It can be decomposed to seismic noise, suspension thermal noise, mirror thermal noise, and quantum noise.

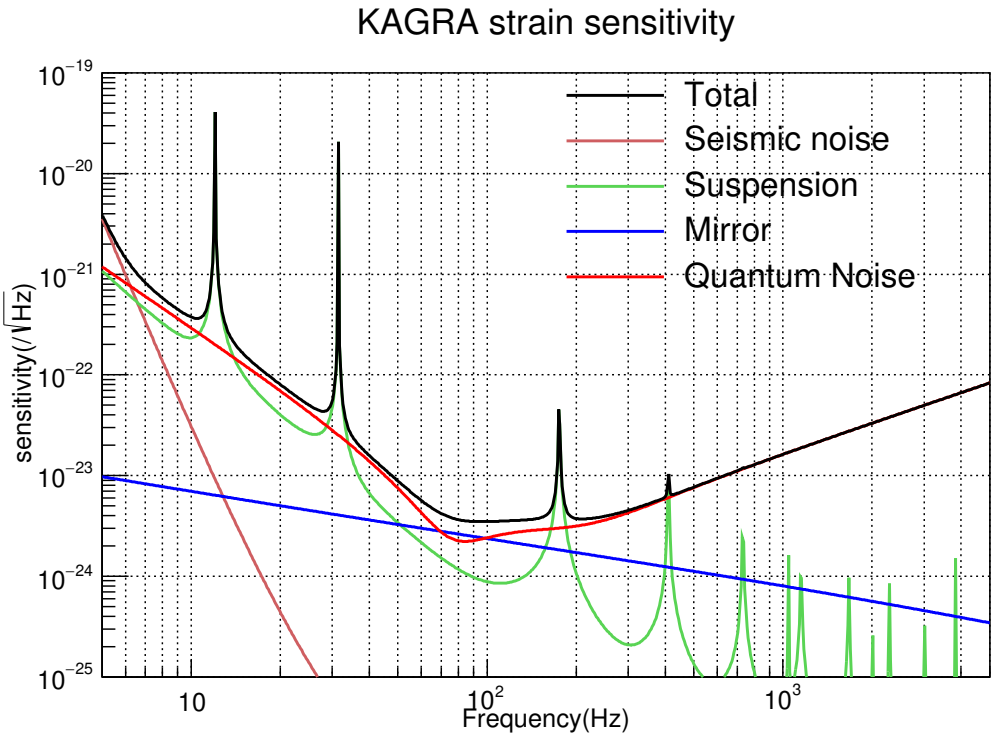

FIGURE 3.4: The design strain sensitivity of KAGRA

3.3 Gravitational Wave detector in worldwide

3.3.1 LIGO

LIGO is two ground-based Fabry-Perot Michelson interferometer whose arm length is 4 kilometers located in America [4]. One interferometer is located in Hanford and the other

is located in Livingston. The construction started in 1992. The first gravitational wave event was detected by LIGO Hanford, Washington and LIGO Livingston, Louisiana in September 14, 2015.

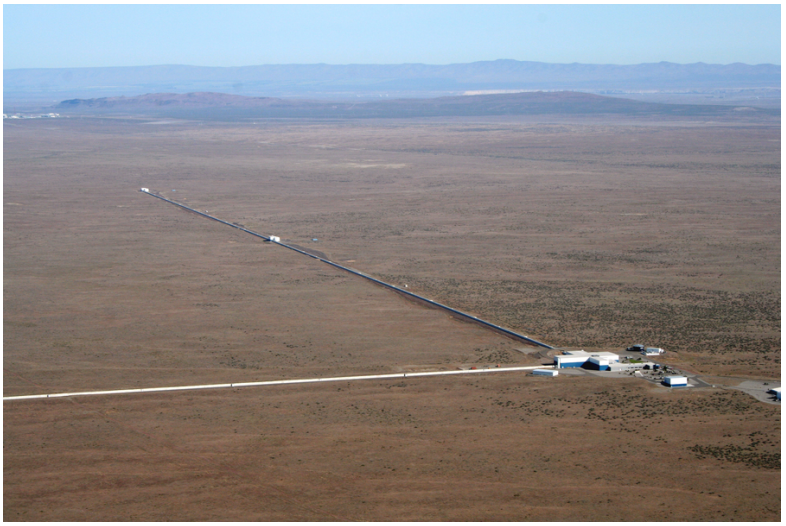

FIGURE 3.5: LIGO Hanford Observatory [4]

FIGURE 3.6: LIGO Livingston Observatory [4]

3.3.2 Virgo

Virgo is a ground-based Fabry-Perot Michelson interferometer whose arm length is 3 kilometers [18]. It was constructed in 1996 near Cascina sitePisa, Italy. The first gravitational wave detection of Virgo is on August 14, 2017. It also detected the binary neutron star coalescence on August 17, 2017. The cooperation between LIGO and Virgo increases the source localization from hundreds of deg^2 to tens of deg^2.

FIGURE 3.7: Virgo detector [4]

3.3.3 GEO600

GEO600 is a ground-based interferometric gravitational wave detector located near Hannover[19], Germany. It was built in 1995, and the arm length is 600 meters. GEO 600 used many advanced technologies to reach the sensitivity to the order of 10^{-21}, such as monolithic suspensions, electrostatic drives, signal recycling, output mode cleaner, which are planned to be used in the next generation of gravitational wave detectors.

3.3.4 Other detectors

Apart from current gravitational wave detectors, there are many gravitational wave detectors which are planned to be built. LIGO plan to move gravitational wave detector component from 2 km Hanford component to India, which is called LIGO-india [20]. LIGO-india is set to be built by 2025. Furthermore, LIGO plan to upgrade the current detector by using cryogenic mirror, which is called LIGO Voyager, and will be installed by 2025 [21]. For the third generation gravitational wave detectors, Einstein Telescope,

FIGURE 3.8: GEO600 [4]

which is two 10 kilometers xylophone shape detectors, is planned be built in Europe [22]. One detector is working in room temperature as a high frequency detector, and the other working in cryogenic temperature as a low frequency detector. LIGO also plans to built a third generation detector called Cosmic explorer, whose arm length is 40 kilometers[21]. The informations of gravitational wave detectors is summarized in Table. 3.1.

3.4 Summary

In this chapter, we discussed the operation principle of Michelson interferometer for detecting gravitational waves, and we showed the reason why we need the Fabry-Perot Michelson interferometer. Next we introduced KAGRA, which is the Large-scale Cryogenic Gravitational-wave Telescope, and showed two features of KAGRA. Finally, we introduced LIGO, Virgo, GEO 600, which are three operating interferometers in the world, and also compared the gravitational wave interferometer in worldwide.

Detectors	Arm length	Mirror material	Mirror masses	Mirror temperature	Location	Country
KAGRA	3km	Sapphire	23kg	20K	underground	Japan
LIGO	4km	Fused Silica	40kg	300K	ground-based	USA
Virgo	3km	Fused Silica	40kg	300K	ground-based	Italy
GEO600	600m	Fused Silica	5.6kg	300K	ground-based	Germany
LIGO india	4km	Fused Silica	40kg	300K	ground-based	India
LIGO Voyager	4km	Silicon	200kg	123K	ground-based	USA
Einstein Telescope (HF)	10km	Fused Silica	200kg	290K	underground	Europe
Einstein Telescope (LF)	10km	Silicon	211kg	10K	underground	Europe
Cosmic Explorer	40km	Silicon	320kg	123K	underground	USA

Table 3.1: The gravitational wave detectors in world wide

Chapter 4

GW detector Calibration and Photon Calibrator

4.1 Overview of Calibration

In order to accurately analyze the physical parameter from gravitational wave signal, calibration with accuracy and precision within 1% is required in the current stage. Fig. 4.1 shows the differential arm length (DARM) feedback control loop and the gravitational wave signal reconstruction pipeline [23]. When the gravitational wave incident on a interferometer and change the length of two arms $\Delta L_{\text{ext}} = \Delta L_x - \Delta L_y = hL$, DARM loop generate the laser power fluctuations at the readout photodetector. Error signal d_{err} is the digitize signal of PD readout, and sensing function $C = d_{\text{err}}/\Delta L_{\text{res}}$ defines the readout photodetector response to DARM loop displacement, where ΔL_{res} is the residual DARM displacement suppressed by feedback control. Digital filters $D = d_{\text{ctrl}}/d_{\text{err}}$ convert the error signal to control signal d_{ctrl}, and d_{ctrl} controls the actuators $A = \Delta L_{\text{ctrl}}/d_{\text{ctrl}}$ and generate force on the optical cavity to change length in order to cancel the DARM displacement and lock the interferometer. The relationship between error signal, control signal, and DARM loop displacement ΔL_{ext}, ΔL_{res} is given by:

$$\begin{aligned} d_{\text{err}} &= \Delta L_{\text{res}} C \\ d_{\text{ctrl}} &= \Delta L_{\text{res}} C D \\ \Delta L_{\text{res}} &= \Delta L_{\text{ext}} - d_{\text{ctrl}} A \end{aligned} \tag{4.1}$$

We can write each parameters by ΔL_{ext}:

$$\begin{aligned} \Delta L_{\text{res}} &= \frac{1}{1+G}\Delta L_{\text{ext}} \\ d_{\text{err}} &= \frac{C}{1+G}\Delta L_{\text{ext}} \\ d_{\text{ctrl}} &= \frac{G}{1+G}\frac{1}{A}\Delta L_{\text{ext}} \end{aligned} \tag{4.2}$$

and the reconstructed gravitational wave strain signal can be written as

$$h = \frac{\Delta L_{\text{ext}}}{L} = \frac{1}{L}\left(\frac{1}{C^{(\text{model})}} * d_{\text{err}} + A^{(\text{model})} * d_{\text{ctrl}}\right) \tag{4.3}$$

where $C^{(\text{model})}$ and $A^{(\text{model})}$ are the models of sensing function and actuation function.

From Eq. 4.3, we understand that in order to calibrate gravitational wave signal accurately, the accurate calibration of sensing function C and actuation function A is important. To search the systematic errors in interferometer, three fundamental methods are used for calibrate the actuator: Free-swinging Michelson method use the laser wavelength for calibration, photon Calibrator method use modulated photon pressure generated by auxiliary laser to calibrate the mirror displacement, frequency modulation method relies on frequency-to-length transfer function for a Fabry-Perot cavity [24].

For free-swinging Michelson method, first we misalign the ETMs and align ITMs to form a simple Michelson interferometer as shown in Fig. 4.2(a). The output is locked at the dark fringe. We can measure the over open-loop transfer function and transfer function from ITM to Michelson readout by actuating the ITM . Then we unlock the feedback loop, allow suspension system to swinging freely. The change of arm length cause the photodetector readout fluctuate from bright fringe to dark fringe. The difference between peak to peak output corresponds to the situation when the displacement difference of two ITMs is one-fourth of the main laser wavelength. Therefore we can calibrate the photodetector readout using laser wavelength, and measure the optical gain. Combining this result with ITM transfer function result, we can calibrate the actuation function of the ITMs. Next, we misalign one of the ITM and realign the ETM on the other arm, forming a resonant Fabry-Perot cavity as shown in Fig. 4.2(b). We measure the transfer function from ITM and ETM to the Michelson readout. Thus, the actuation function of ETM can also be calibrated.

However, in free-swinging Michelson method the we need electronics to generate large amplitude, which cause the large noise. Besides, the actuation signal generated by free-swinging michelson method is too large compared to gravitational wave amplitude. Furthermore, we need to unlock the interferometer to perform a free-swinging michelson calibration, which could not be used while interferometer is locked. Therefore, we

need to choose another high sensitivity calibration method. Photon Calibrator is a candidate of high sensitivity calibration method which could be used in locked Michelson interferometer.

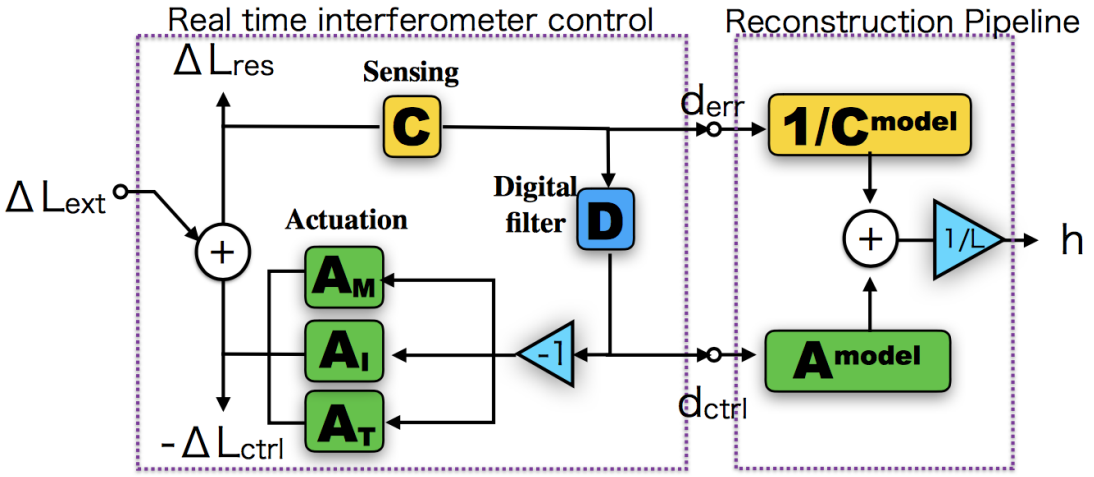

FIGURE 4.1: DARM feedback control loop and GW signal reconstruction

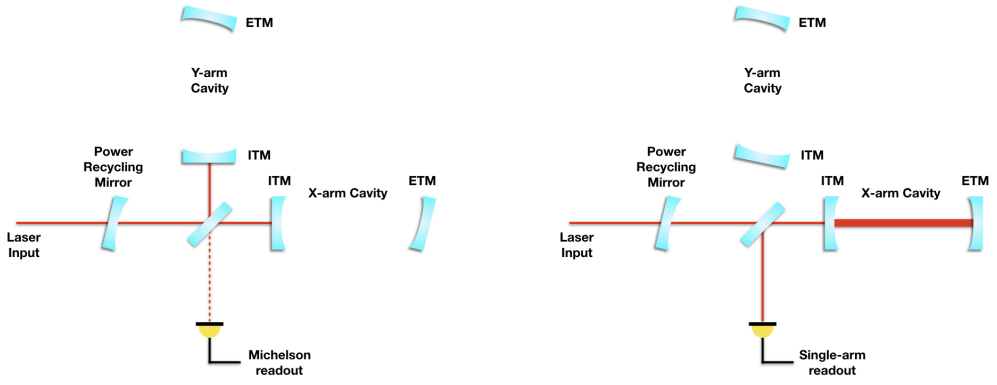

(a) ITM actuation function calibration

(b) ETM actuation function calibration

FIGURE 4.2: Free-swinging Michelson calibration method

In this chapter, we will introduce the photon Calibrator. An introduction of photon Calibrator is shown in section 2. Section 3 and section 4 introduce the details of transmitter module and receiver module of photon Calibrator. Section 5 explain the periscope used for sending Pcal beam to ETM. Telephoto camera which is used for monitoring Pcal beam is discussed in Section 6. The transfer function of digital filters is discussed in Section 7, and the noise requirement of Pcal is given in Section 8.

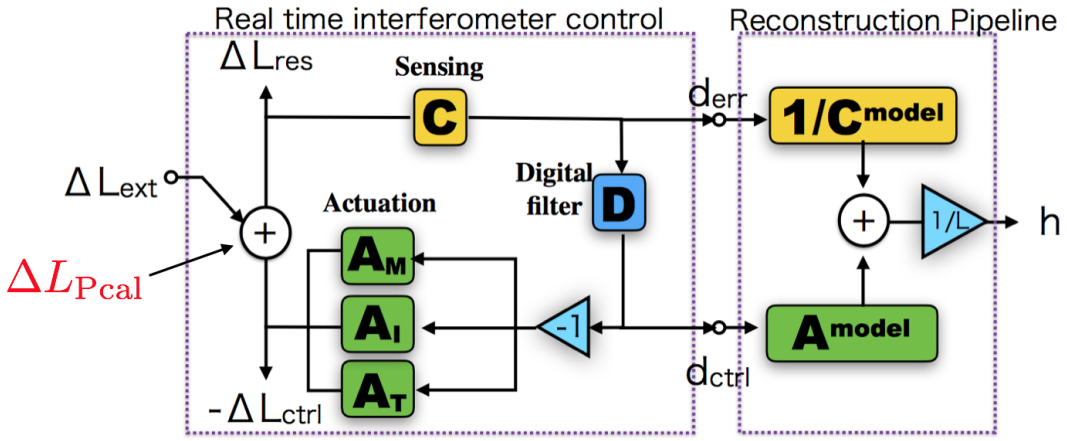

FIGURE 4.3: Schematic of arm length difference generated by Pcal in DARM loop

4.2 Introduction to Photon Calibrator

Photon Calibrator (Pcal) use photon pressure from an auxiliary laser, which is placed in End-A chamber (EXA at X-end and EYA at Y-end), to apply the periodic force on the end test mass. This periodic force continuously change the arm length, and we can monitor the response of sensing function C and actuation function A (Fig. 4.3). Since we do not know how does the C and A look like, we plan to inject 5 different frequencies of periodic modulation, so-called calibration lines, to understand C and A performance. The 5 frequencies are chosen at 7 Hz, 35 Hz, 330 Hz, 1 kHz, 3 kHz due to the response of C and A. We plan to inject these 5 calibration lines with signal to noise ratio (SNR) 100. Fig. 4.4 shows the 5 calibration lines with signal to noise ratio 100 compare to relative power noise requirement of Pcal laser. We will explain how to calculate the relative power noise requirement of Pcal in Sec. 4.6.

If we put this calibration lines on the KAGRA sensitivity curve, it will be shown like Fig. 4.5.

From Fig. 4.5, we understand that the relative power noise floor of Pcal is important. If the relative power noise floor of Pcal is high, it will become a noise source of KAGRA and decrease the sensitivity. To prevent Pcal being one of the noise source in the KAGRA interferometer, the laser power stabilization is one of the most important issue in Pcal. Photon Calibrator consist of transmitter module (Tx module), receiver module (Rx module), telephoto camera (Tcam) and periscope. In the photon Calibrator system, two power modulated beam are generated in Transmitter module. In order to stabilized and clean modulated laser power, an active feedback control system called Optical Follower Servo is used in Pcal system. Two laser beams are sent from Tx module to the periscope in EYA chamber, and passing through four mirrors in the EYA chamber then reach the

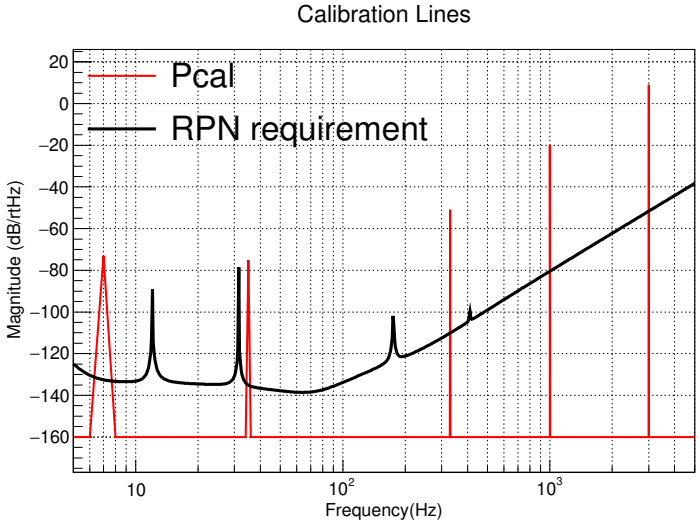

FIGURE 4.4: 5 calibration lines with laser noise level at -160 dB/rtHz with SNR 100. Black line is the relative power noise requirement of Pcal laser.

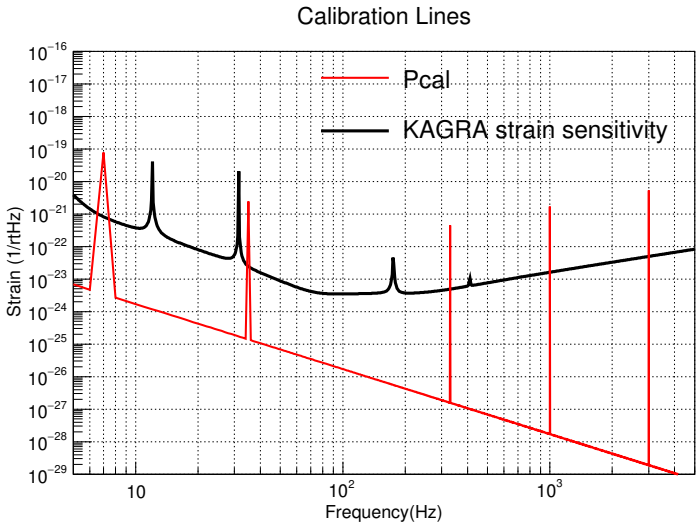

FIGURE 4.5: 5 calibration lines with laser noise level at -160 dB/rtHz with SNR 100 on the KAGRA strain sensitivity curve

end test mass. After reflected from end test mass, two laser beam pass through four periscopes again and finally go to Rx module. The distance between EYA chamber and ETM is 36 m. The position of two laser beams is monitored by telephoto camera, which we use telephoto camera to analyze the beam positions. The schematic layout of photon Calibrator is shown in Fig. 4.6. We will explain each part of the photon Calibrator in the following section.

The displacement of ETM induced by photon Calibrator can be described by

$$x(f) = \frac{2P\cos\theta}{c} S(f) \left(1 + \frac{M}{I}(\vec{a}\cdot\vec{b})\right) \tag{4.4}$$

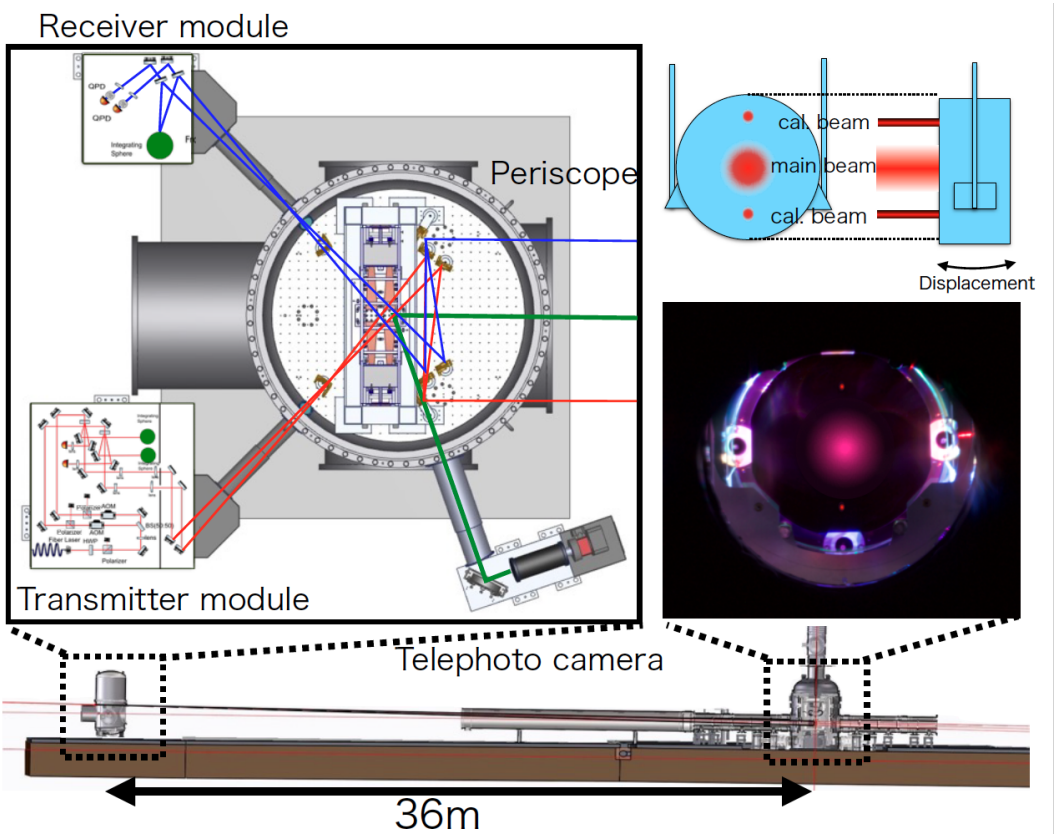

FIGURE 4.6: Schematic of Yend Pcal

where θ is the incident angle of the Pcal beams on the end test mass surface, c is the speed of light in vacuum, M is the mass of the mirror, I is the moment of inertia of the mirror, $\vec{a}$ and $\vec{b}$ are displacement vectors from the center of the test mass for photon Calibrator lasers and interferometer laser, and $S(f)$ is the force-to-length transfer function of the suspended end test mass. In KAGRA, the end test mass is suspended by 14 meter vibration isolation system, and $S(f)$ can be approximate by $S(f) \approx -1/(M(2\pi f)^2)$ at higher frequency (>10 Hz) from its transfer function. The specifications of KAGRA Pcal, and aLIGO, Virgo Pcal are shown in Table. 4.1.

	KAGRA	**aLIGO**	**aVirgo**
Mirror material	Sapphire	Silica	Silica
Mirror mass Mass M	23kg	40kg	40kg
Mirror diameter	220 mm	340 mm	350 mm
Mirror thickness	150 mm	200 mm	200 mm
Incident angle θ	0.72deg	8.75deg	30deg
Displacement from Pcal to ETM	36m	8m	1.5m
Pcal laser power P	20W	2W	3W
Laser wavelength	1047nm	1047nm	1047nm

TABLE 4.1: Parameters of Photon Calibrator

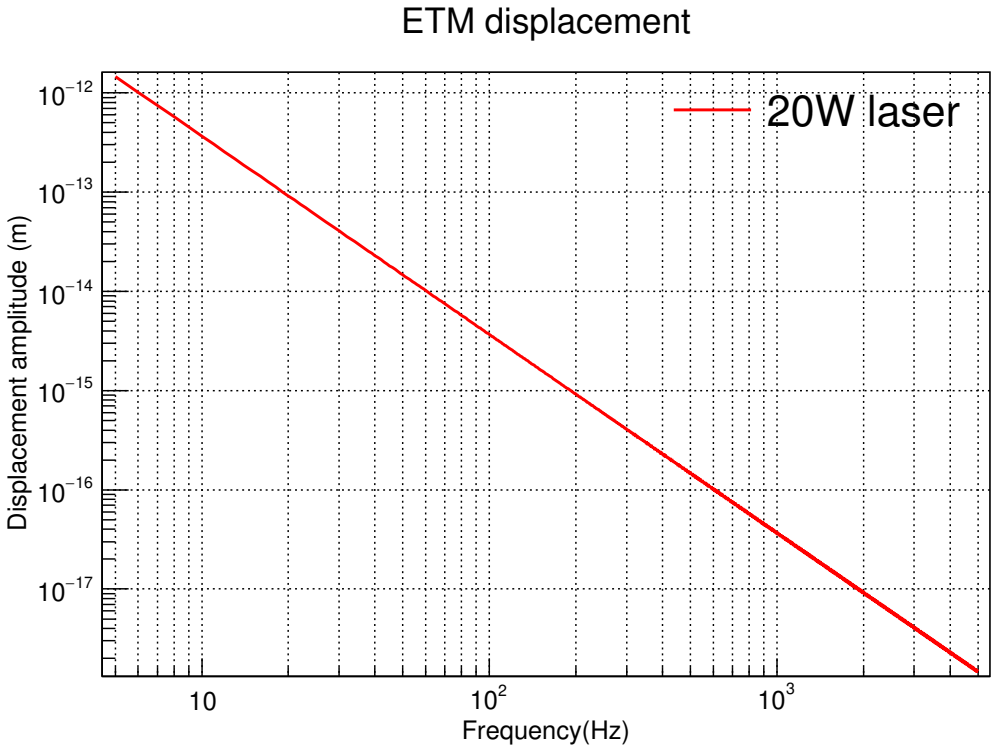

FIGURE 4.7: Displacement of ETM

We can estimate the displacement of the end test mass by using the parameters in Table. 4.1. We assume 25% of the total power can be used for mirror displacement. A half is because we modulate the laser power by plus and minus sine wave, and the other half is the pessimistic estimation of transmitter module optical efficiency and AOM efficiency. Using these parameter, we can calculate that the maximum displacement of the mirror is

$$x(f) = 3.67 \times 10^{-11}/f^2 \quad [m] \tag{4.5}$$

and the result is shown in Fig. 4.7.

4.3 Transmitter Module

The purpose of transmitter module is to generate power stabilized laser beams and modulate the laser power. Fig. 4.9 shows the optical layout of Tx module. The optical components are mounted on a 900 mm×900 mm optical table made by Thorlabs (B9090L) [25]. The compliance curve of the optical table is shown in Fig. 4.8.

We use a 20 watt laser in our photon Calibrator system to generate sinusoidal modulation in high frequency without long integration time. In order to modulate the laser power, we

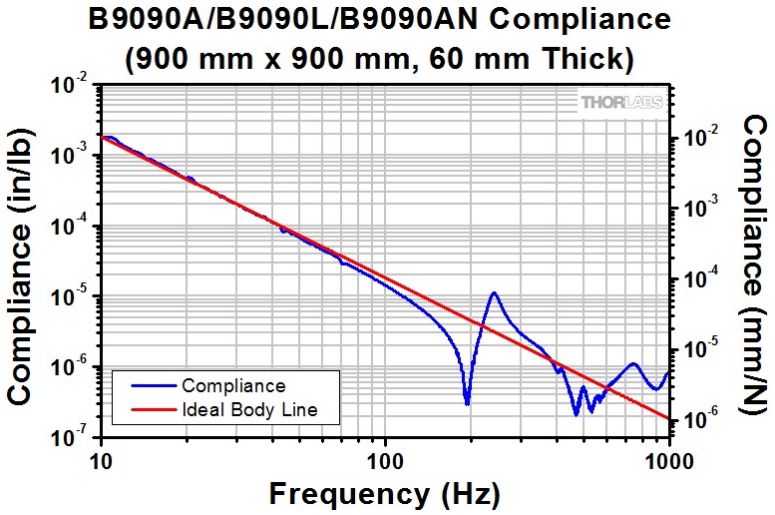

FIGURE 4.8: Compliance Curve of B9090L breadboard [25]

employ acousto-optic modulator (AOM). In KAGRA photon Calibrator, we use 2 AOMs in the transmitter module, which allow as to generate different force by photon pressure to mitigate the rotational effect of the end test mass. Since the performance of AOM depend on the polarization angle of the laser, we use half-wave plate and polarizer to control the polarization angle of the laser. Besides, the beam width requirement of AOM is 250 μm, so we put a positive lens in front of AOM to make the beam width matches the requirement. We split the laser beam into two beams by a beam splitter, each beam is emitted to a AOM. After modulated by AOM, each laser beam pass through a beam sampler to provide sample beams for photodetectors and integrating sphere. We send the modulated signal to optical follower servo, which reduce the high frequency noise. The optical follower servo controls AOM, generates the modulated laser beam, which constitutes a feedback control loop. By using this feedback control loop, the laser power can be stabilized. The main laser beam will pass through a 1-inch negative lens and a 2-inch positive lens, which are used for modematching for ETM, and we put picomotors at the end of Tx module to adjust the beam position on the ETM precisely. Since the distance from EYA chamber to ETM is 36 meters and the infrared laser is not visible, the beam alignment is not so easy. To make it easier, we employ two green laser for the beam alignment. The picture of Tx module is shown in Fig. 4.10. Each component inside the transmitter module is introduced in the following sections.

4.3.1 Ytterbium fiber laser

In the KAGRA photon Calibrator, we use LEA PHOTONICS CW Ytterbium fiber laser (CYFL-TERA) [26]. The model number is CYFL-TERA-20-LP-1047-AM1-RGO-OM1-T305-C1. The laser wavelength is 1047 nm, the maximum power is 20 watts, and the

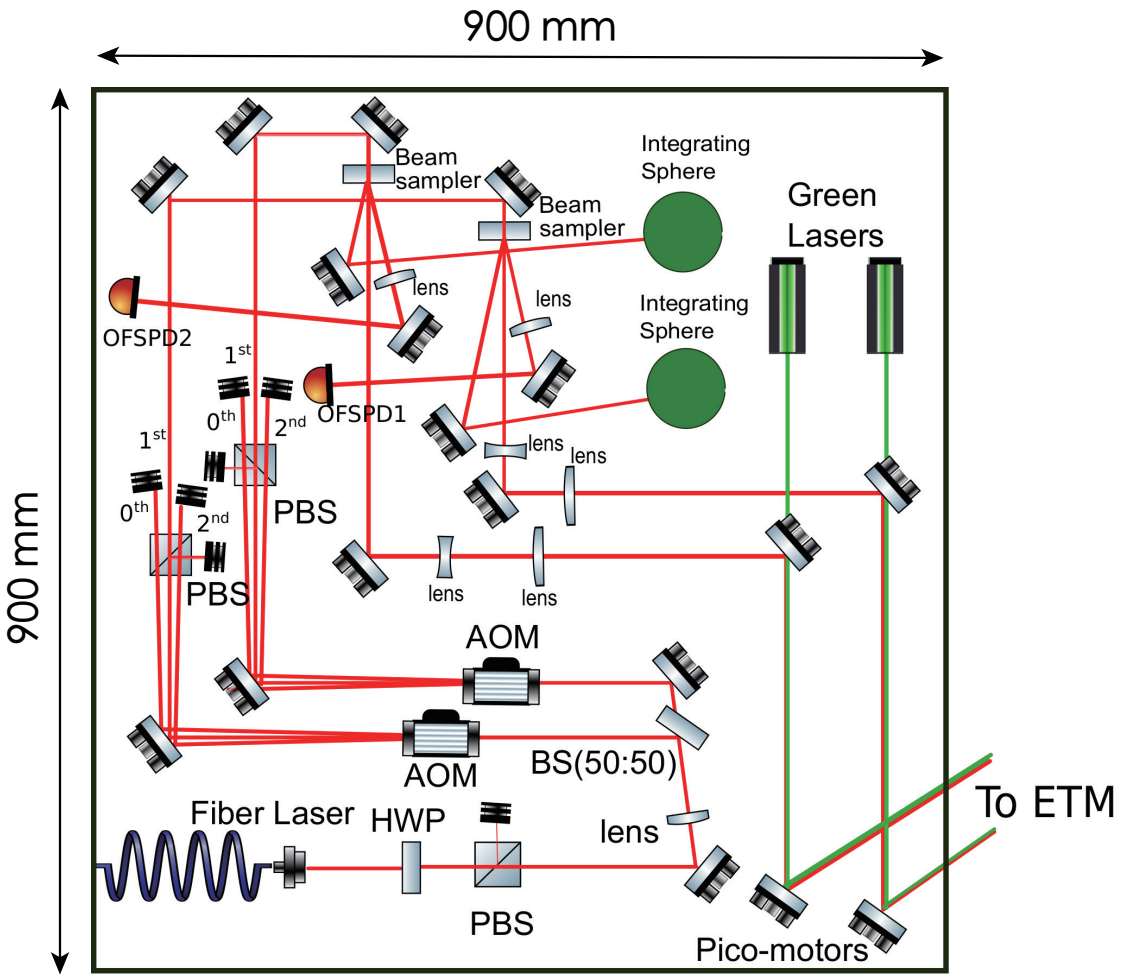

FIGURE 4.9: Optical layout of Tx module

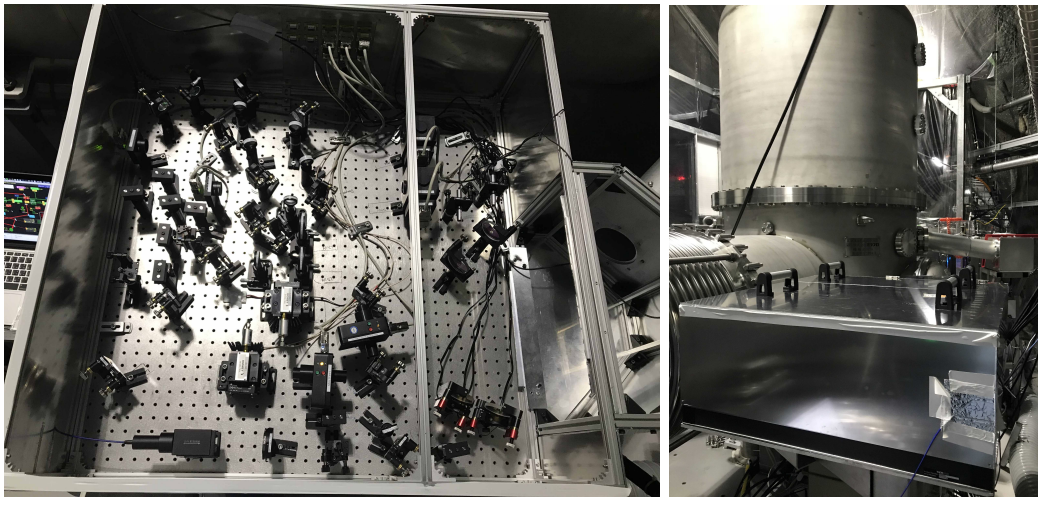

FIGURE 4.10: Picture of Tx module

beam quality is less than 1.1. The definition figure of beam quality M^2 is shown in Fig. 4.11. The input beam waist is D, and we put a positive lens whose focal length is f to focus the beam. The distance between input beam waist and lens should also be

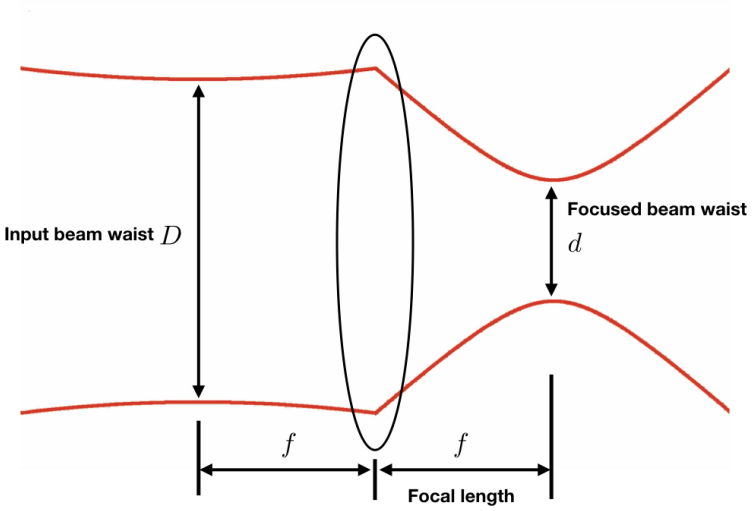

FIGURE 4.11: Beam quality M^2 definition

f. Then we can measure the focused beam waist d after lens. Then the beam quality M^2 is defined as

$$M^2 = \frac{dD\pi}{4\lambda f} \tag{4.6}$$

where λ is the wavelength of the laser. For a gaussian beam, the beam quality is unity.

An Faraday isolator is placed at the output port of fiber to prevent unwanted beam feedback into laser cavity. The picture of laser and the isolator are shown in Fig. 4.12 and Fig. 4.13. It has active power control (APC) and active current control (ACC) modes. APC mode allows you to adjust the power set point to control the laser power, and ACC mode allows you to adjust the current set point to control the laser. We use the Ophir StarBright power meter to measure the laser power [27]. The picture of the power meter is shown in Fig. 4.14. The measured value of APC and ACC performance are shown in Fig. 4.15.

4.3.2 0^{th} order half wave plate

To control the polarization angle of the beam, we use half-wave plate made by CVI laser optics [28]. The part number is QWPO-1047-05-2-R10 with wave length 1047 nm, and the waveplate diameter is 12.7 mm. The details of the half-wave plate is shown in Table. 4.2.

FIGURE 4.12: Picture of 20W laser

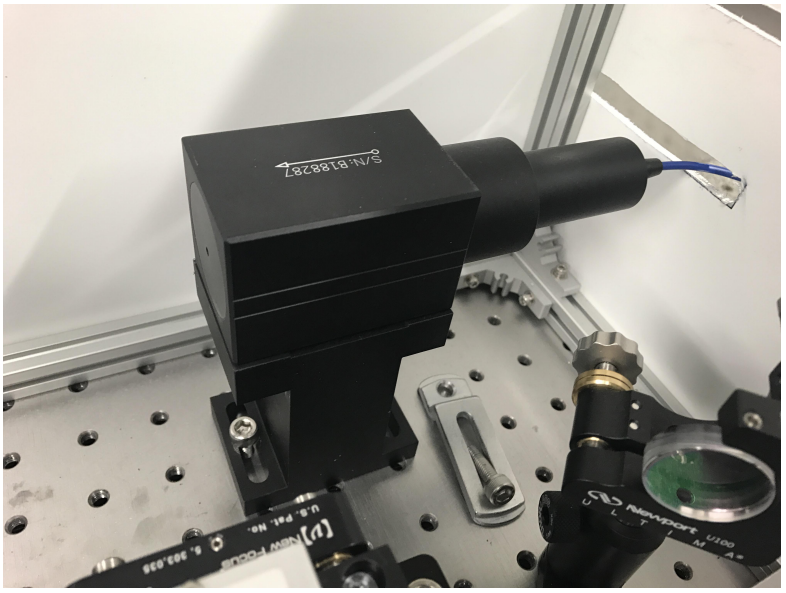

FIGURE 4.13: Picture of isolator

Next, we calculate how half-wave plate change the polarization angle of the beam. The function of half-wave plate can be described using Mueller matrix.

$$M = \begin{pmatrix} 1 & 0 & 0 & 0 \\ 0 & 1 & 0 & 0 \\ 0 & 0 & -1 & 0 \\ 0 & 0 & 0 & -1 \end{pmatrix} \tag{4.7}$$

(a) Power meter (b) Reader

FIGURE 4.14: StarBright power meter [27]

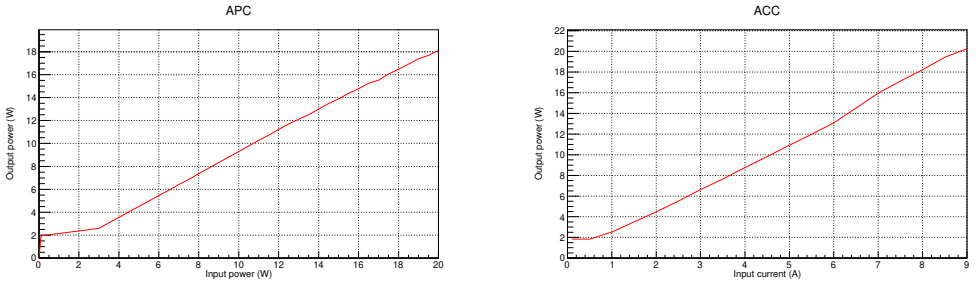

(a) APC mode (b) ACC mode

FIGURE 4.15: Measured laser power

Parameters	Value	Unit	Note
Waveplate Type	Quartz Waveplates		
Wavelength Range	1047	nm	
Retardance	$\lambda/2$		half-wave
Clear aperture	85	%	of diameter
Reflection	0.25	%	per surface
Retardance Tolerance	$\lambda/200$ to $\lambda/500$		at 23 °C
Material	Crystal Quartz		
Surface Quality	10.5	scratch-dig	
Waveplate Diameter	12.7	mm	

TABLE 4.2: Specification of Half-wave plate

For a linear horizontal polarization beam, the Stokes vector S can be written as

$$S = \begin{pmatrix} 1 \\ 1 \\ 0 \\ 0 \end{pmatrix} \tag{4.8}$$

The rotation matrix $R(\theta)$ is

$$R(\theta) = \begin{pmatrix} 1 & 0 & 0 & 0 \\ 0 & \cos(2\theta) & \sin(2\theta) & 0 \\ 0 & -\sin(2\theta) & \cos(2\theta) & 0 \\ 0 & 0 & 0 & 0 \end{pmatrix} \tag{4.9}$$

The Stokes vector after passing through half wave plate is

$$S' = R(\theta)MR^{-1}(\theta)S = \begin{pmatrix} 1 \\ \cos(4\theta) \\ -\sin(4\theta) \\ 0 \end{pmatrix} \tag{4.10}$$

The Strokes vector becomes identical when half-wave plate is rotated every 90 degrees. We rotate the half-wave plate, put a polarizar after it and measure the laser power. The measured result is shown in Fig. 4.16. From the result, we can see that the period of laser state is 90 degrees.

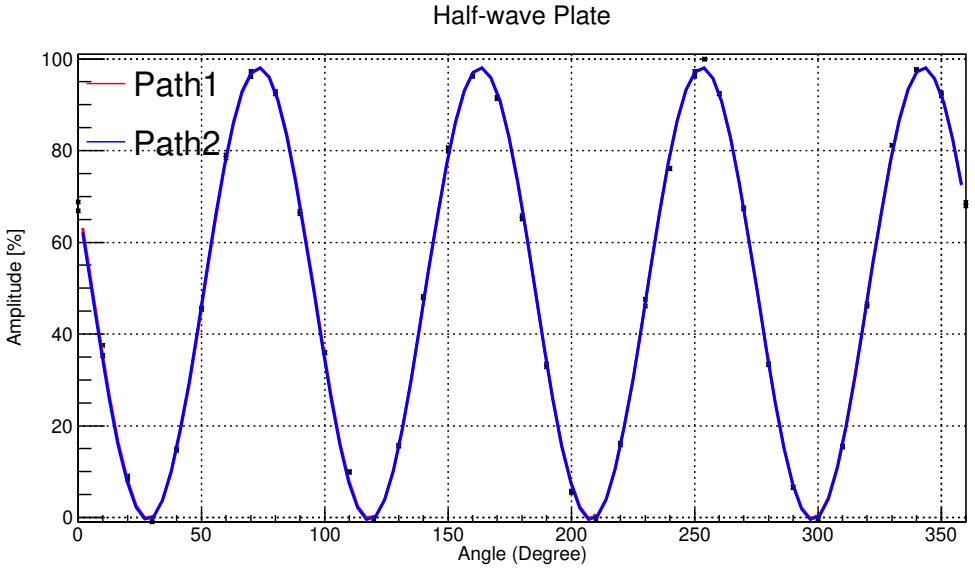

FIGURE 4.16: The measured performance of Half-wave plate

4.3.3 Polarizer

We place 3 polarizers to define the polarization angle of our beam, since the performance of half-wave plate and Acousto-optic modulators (AOMs) depend on the polarization angle of the beam. One polarizer is placed right after HWP to maintain the same incident

polarization angle emitted to AOM. The other two polarizers are placed after two AOMs to ensure the both beams after AOM has the same polarization angle. The polarizer is manufactured by Karl Lambrecht Corporation [29]. The part number is TFPC12-1047, which is optimized for 1047 nm laser. The specification is shown in Table. 4.3, and the transmission of s and p polarization is shown in Fig. 4.17.

Parameters	Value	Unit	Note
Cube Dimensions	12.7*12.7*12.7	inch	±0.25 mm
Standard Central Wavelength	1047	nm	
Substrate	BK7		
Clear aperture diameter	12	mm	
Surface Quality	40-20	scratch-dig	

TABLE 4.3: Specification of Polarizers

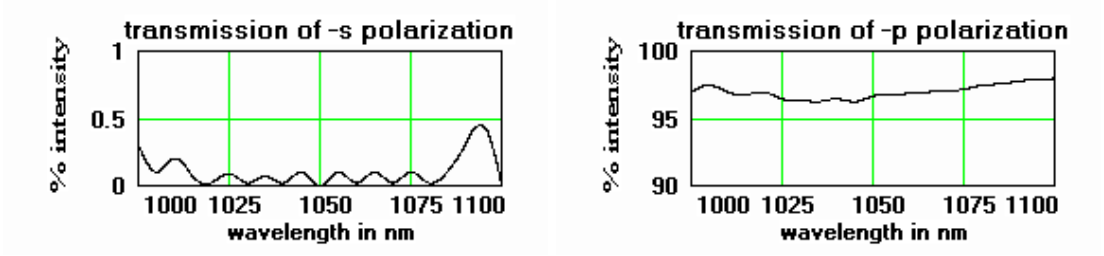

FIGURE 4.17: Transmittance of polarizer (Specification) [29]

From Fig. 4.17, we can see that around 3 % of power is lost in the p-polarization.

4.3.4 Mirror

We employ 14 one-inch mirrors and 4 two-inch mirrors. One inch mirror is made by CVI laser optics [30]. The part number is Y1S-1025-45, and the specification is shown in Table. 4.4.

Parameters	Value	Unit
Coating Wavelength	1064	nm
Dimensions	25.4	mm
Thickness	6.35	mm
Incidence Angle	45	degree
Coating Type	Ion Beam Sputtered	
Shape	Flat	
Material	Fused Silica	
Clear aperture diameter	$\geq$ 85%	
Surface Quality	10-5	scratch-dig

TABLE 4.4: Specification of Mirrors

We measured the relationship between mirror reflectivity and incident angle. The result is shown in Fig. 4.18.

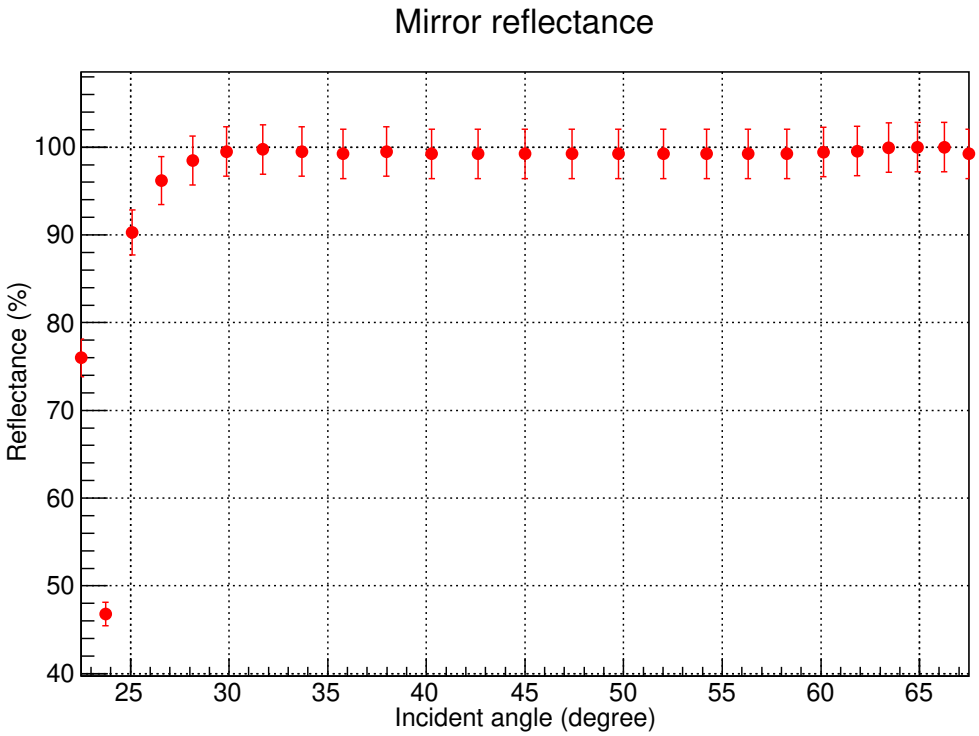

FIGURE 4.18: Reflectivity of the mirror

4.3.5 Beam Splitter

We split the laser beam into two beams with the beam splitter manufactured by CVI laser optics [31]. The part number is BS1-1064-50-1012-45P. The specification is shown in Table. 4.5. From Table. 4.5, we found that the error of reflectivity is too large for

Parameters	Value	Unit
Wavelength	1064	nm
Dimensions	25.4	mm
Thickness	3.18	mm
Beamsplitter Type	Plate Beamsplitters	
Coating Type	Laser Line Dielectric	
Shape	Round	
Material	Fused Silica	
Clear aperture diameter	$\geq$ 85%	
Surface Quality	10-5	scratch-dig
Reflectivity	50.0$\pm$4.0	%

TABLE 4.5: Specification of beam splitter

us. We measured the relationship between beam splitter reflectivity and incident angle. The result is shown in Fig. 4.19. We found that the angle which beam splitter has 50%

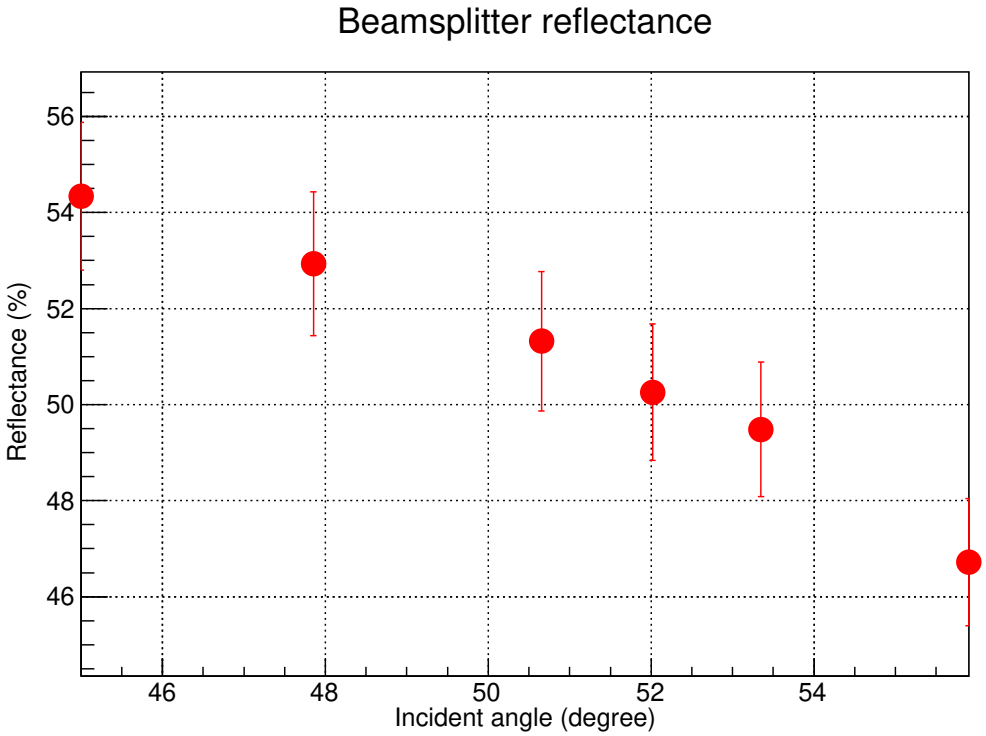

FIGURE 4.19: Reflectivity of the beam splitter

reflectivity is not 45 degree but 52.5 degree. To balance the power of two beams, we can either choose to change polarization angle of the beam or change the incident angle of beam splitter. However, the performance of AOM depends on angle of polarization, it is better to maintain the same polarization angle and change the incident angle of beam splitter. Therefore, we aligned the laser beam to make the incident angle be 52.5 degree and ensure the power of two beams are the same. In LIGO, they put a beam splitter after AOM to split the laser beam and the incident angle is 45 degrees. Thus, their power difference of two Pcal beams could be larger than KAGRA Pcal.

4.3.6 Acousto-optic modulator

Acousto-optic modulator (AOM) is use for modulating laser power and making calibration lines. AOM is made by ISOMET company [32]. The part number is M1080-T80L-1.5 and the specification is shown in Table. 4.6. The AOM driver is also made by ISOMET company and the part number is 532C-4 [33]. In KAGRA Pcal, we use two AOMs to mitigate the rotation effect of end test mass. We use AOM and Optical Follower Servo to reduce the noise of our laser. The detail of Optical Follower Servo is in Ch. 6.

Parameters	Value	Unit
Spectral Range	0.36>1.5	μm
A/R Wavelengths	700-900 or 1064	μm
Interaction Medium	Tellurium Dioxide(TeO_2)	
Acoustic Velocity	4.2	mm/μs
Center Frequency	80	MHz
RF bandwidth	30	MHz
Input Impedance	50	Ω
Clear aperture	3.5	mm
Active aperture	1.5	mm
Static Insertion Loss	<3	% at 1.1μm
Reflectivity	<0.5	%/Surface
Laser Polarization	Any	
Optical Power	20	W
Beam width	250	μm
Optical Rise Time	77	ns
Deflection Efficiency	>85	%

TABLE 4.6: Specification of AOM

The figure of AOM is shown in Fig. 4.20.

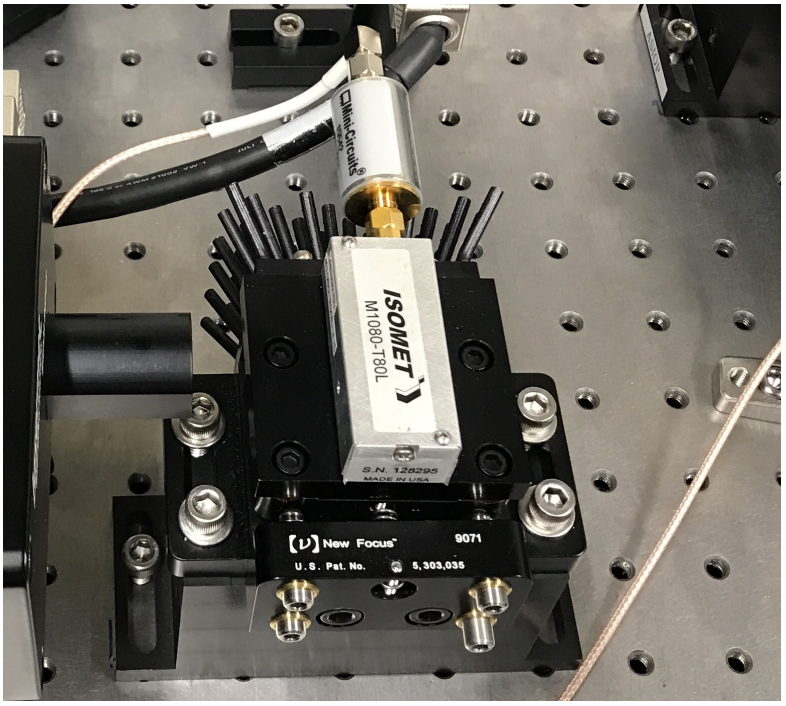

FIGURE 4.20: Acousto-optic modulator

4.3.7 Lens

Since the beam width requirement for AOM is $250\mu m$, we did the mode matching using JamMt to calculate which lens we should use and where the lenses should be placed. The detail of modematching is shown in Sec. 5.3. We use positive and negative lenses manufactured by CVI laser optics [34]. As a result, we use PLCX-25.4-99.9-UV-1053 one-inch positive lens for the mode matching on AOM, and use PLCC-25.4-25.8-UV-1047 one-inch negative lens and PLCX-50.8-62.5-UV-1047 two-inch positive lens for the mode matching on end test mass. The specification is shown in Table. 5.2.

4.3.8 Beam sampler

To make a close-loop feedback control system, we need to acquire the signal from photodetector, and send it back to Optical Follower Servo. Therefore, we use the beam sampler to split the beam into 3 beams. The beam sampler is manufactued by HOLO/OR, and the part number is SA-014-1-Y-A [35]. The power of two side beams are $0.4\%\pm0.1\%$ of the main beam. One of the side beam is injected to a photodetector of Optical Follower Servo (OFSPD), and the other side beam is injected to a photodetector of integrating sphere (TxPD). The error of this beam sampler directly propagate to the difference of measured value of OFSPD and TxPD. The specification is shown in Table. 4.7.

Parameters	Value	Unit
Material	Fused Silica	
Wavelength	1047	nm
Diameter	25.4	mm
Clear Aperture	19	mm
Thickness	3	mm
AR coating	2 Sides	
Energy ratio of sampled beams	0.4±0.1	%
Propagation angle of sampled beams	15.43	degree
Transmission efficiency	closed to 100%	

TABLE 4.7: Specification of beam sampler

4.3.9 Beam shutter

For the safety issue, we put two beam shutters in front of two AOMs to dump the beam when emergency happens. The beam shutter is made by Lasermet company, and the part number is LS-10-12 [36]. The specification is shown in Table. 4.8.

The figure of beam shutter is shown in Fig. 4.21.

Parameters	Value	Unit
Max laser power	20	W
Aperture size	15	mm
Drive voltage	11-14	V DC
Drive voltage with LS-VC-24.12	15-35	V DC
Current consumption	150	mA
Size	98 x 63.5 x 36	mm

TABLE 4.8: Specification of beam shutter

FIGURE 4.21: Beam shutter

4.3.10 Photodetector and Integrating sphere

We use photodetector to detect the laser power. We use photodetectors in Tx module to directly detect the sampled beam from beam sampler, and we also mount the photodetector on the port of integrating sphere in Tx and Rx module. We mount the C30665GH InGaAs photodiode in on the circuit board as shown in Fig. 4.22. We changed the diffrential gain by changing the resistor and capacitor in the circuit. The parameters are listed in Table. 4.9.

Detector	Rt $[k\Omega]$	Ct $[pF]$	Rg $[k\Omega]$	Cg $[pF]$	Gain
OFSPD	8.45	12	2	4.7	1
TxPD	75	2.7	5	4.7	2.5
RxPD	100	2.4	4	4.7	2

TABLE 4.9: Parameters of photodetector

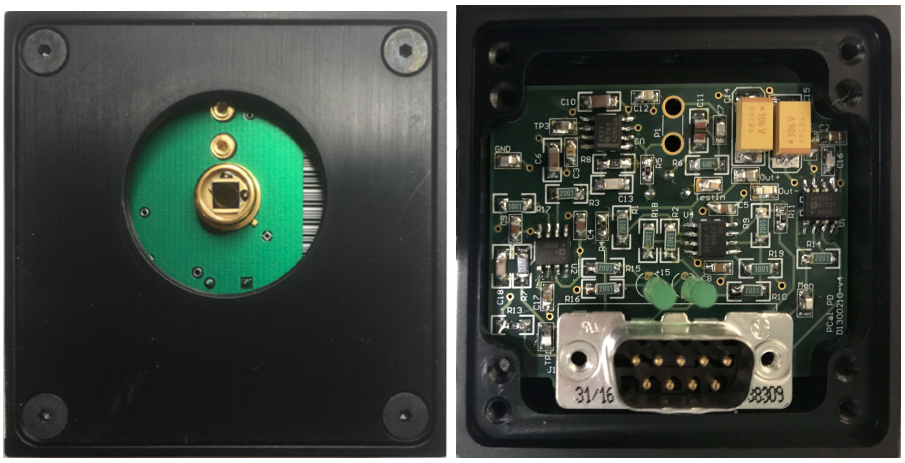

FIGURE 4.22: Picture of photodetector

Besides, we use 2-inch integrating sphere to detect the absolute power of the laser. Integrating sphere collect the light from sampled beam of beam sampler. The beam is scattered uniformly inside the sphere by the diffused material on the wall of sphere after many times of reflections inside the integrating sphere, and we mount a photodetector (TxPD) on the port of integrating sphere to detected the power reduced scattered light (Fig. 4.23). The advantage of using integrating sphere is to remove the angular properties of the incident beam and stabilized the power of detected laser beam. Our integrating sphere is made by Labsphere. Fig. 4.24 is the picture of 2-inch integrating sphere.

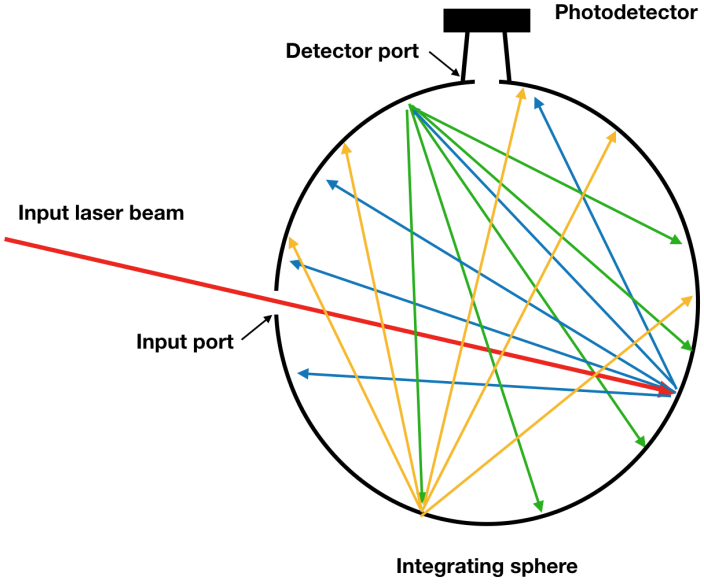

FIGURE 4.23: Principle of Integrating sphere: The beam is scattered uniformly inside the sphere by the diffused material on the wall of sphere after many times of reflections inside the integrating sphere, and we mount a photodetector on the port of integrating sphere to detected the power reduced scattered light.

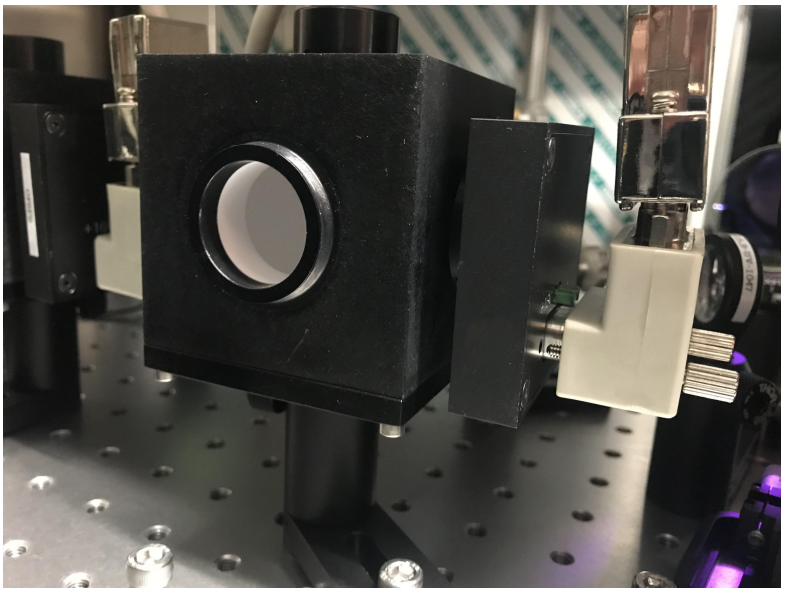

FIGURE 4.24: Picture of 2-inch integrating sphere

4.4 Receiver Module

The purpose of receiver module is to receive both of the laser power and monitor the beam positions. Fig. 4.25 shows the optical layout of Rx module. The optical components are mounted on a 600 mm×600 mm optical table. The picture of Rx module is shown in Fig. 4.26. We employ 6-inch integrating sphere and QPDs in Rx module. We will explain them in the following sections.

4.4.1 RxPD

A 6-inch integrating sphere is used in Rx module for absolute power measurement of the laser. Both of the laser beams are received by the integrating sphere. Since the beam radius in Rx module is around 5mm in Rx module, we need a large diameter hole at least 2 inch for the integrating sphere. We also mount a photodetector (RxPD) on the port of integrating sphere. The figure of 6-inch integrating sphere is made by Labsphere, and the picture is shown in Fig. 4.27.

4.4.2 Quadrant Photodetector

In order to monitor the beam position, we employ quadrant Photodetectors (QPDs) made by Thorlabs [37]. The part number is PDQ30C, and the specification is shown in Table. 4.10.

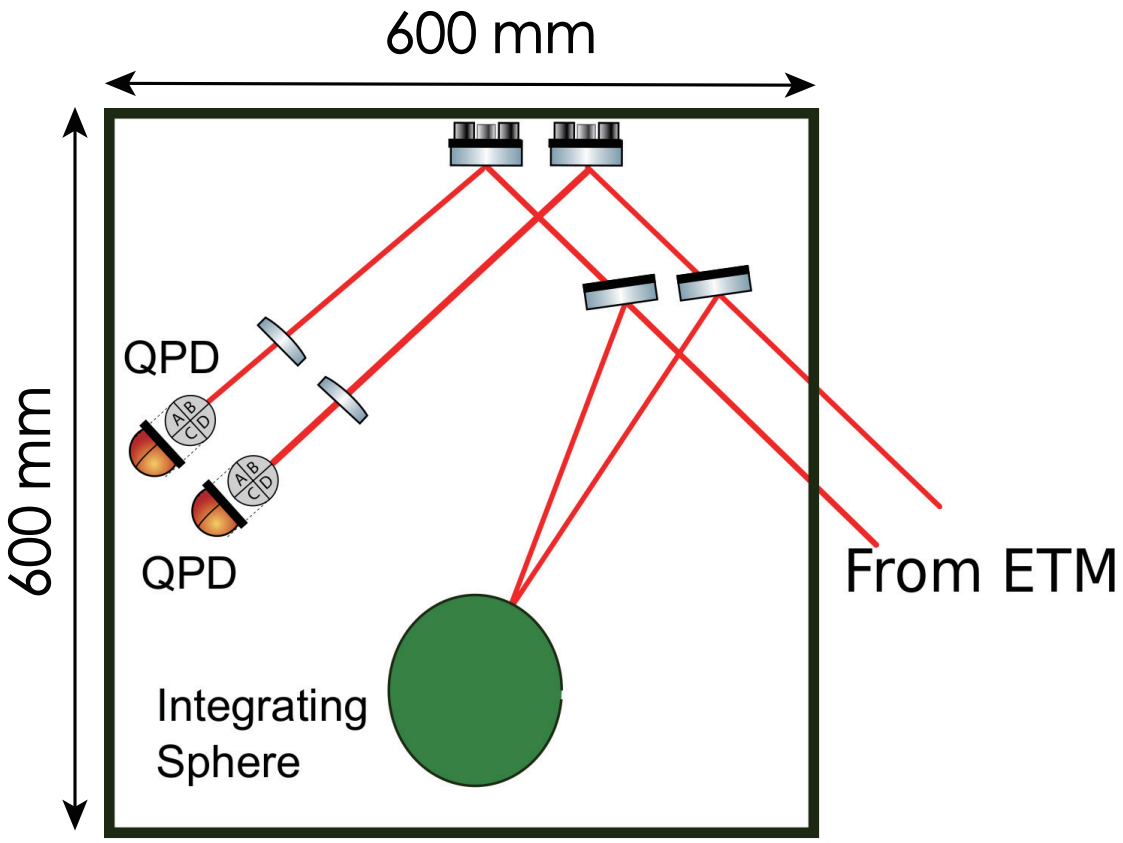

FIGURE 4.25: Optical layout of Rx module

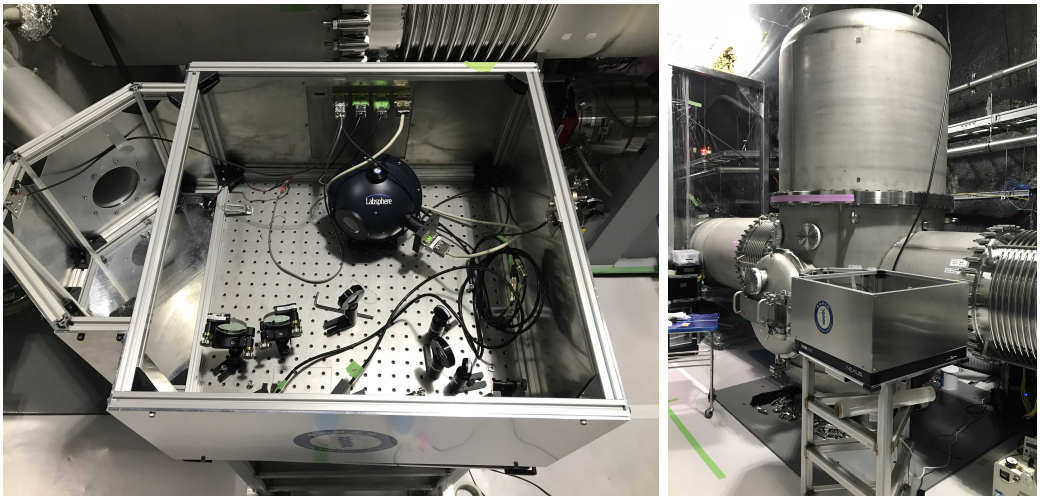

FIGURE 4.26: Picture of Rx module

Fig. 4.28 shows the schematic of QPD. It contains 4 photodiode for precise beam position measurement in the 1000 to 1700 nm infrared range. This sensor output 3 analog voltages shown in Eq. 4.11, and we can use this three voltages to monitor the beam position.

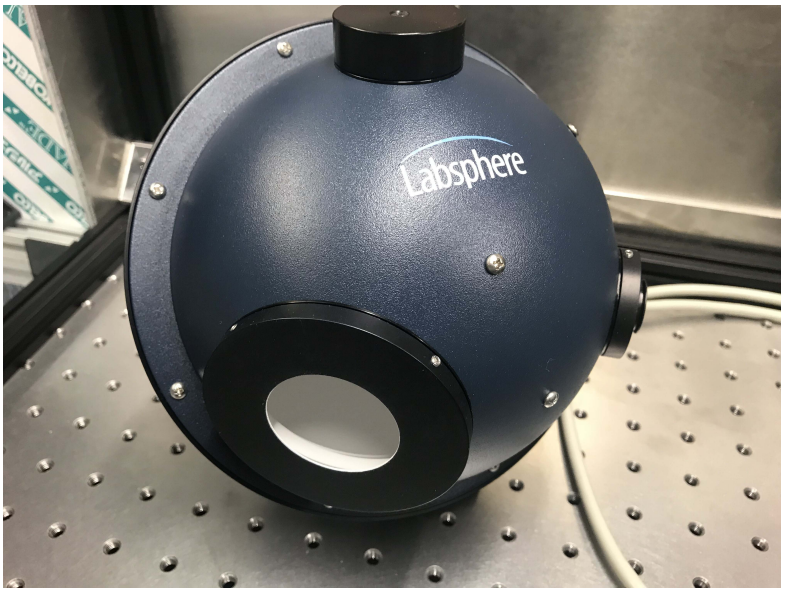

FIGURE 4.27: Picture of 6-inch integrating sphere

Parameters	Value	Unit
Substrate	InGaAs	
Wavelength	1000-1700	nm
Bandwidth	150	kHz
Recommended Spot size	$< \phi$ 0.5	mm
Output Voltage Range	$\pm$4 to $\pm$14	V
Size	50.8 x 30.5 x 16.5	mm

TABLE 4.10: Specification of QPD

FIGURE 4.28: QPD output

The picture of QPD is shown in Fig. 4.29.

$$\begin{aligned} \text{X-axis sensor: } & (Q2 + Q3) - (Q1 + Q4) \\ \text{Y-axis sensor: } & (Q1 + Q2) - (Q3 + Q4) \\ \text{SUM: } & (Q1 + Q2 + Q3 + Q4) \end{aligned} \tag{4.11}$$

FIGURE 4.29: Picture of QPD

4.5 Telephoto Camera

To analyze the beam position on the ETM surface, we employ the combination of telescope and high resolution camera, which is called telephoto camera (Tcam). The picture of two Pcal beams taken by Tcam is shown in Fig. 4.30, and the detail of Tcam is shown in [38].

4.6 Requirements

To calibrate gravitational wave signal accurately, relative power noise of the laser is one of the important issue. KAGRA interferometer has its sensitivity for detecting gravitational waves. We do not want our photon Calibrator become one of the noise source of KAGRA interferometer. Therefore, we need to define the noise requirements for the photon Calibrator.

Fig. 4.31 shows the target strain sensitivity of KAGRA. The displacement of the end test mass induced by photon Calibrator is described as

$$\Delta x(f) = \frac{2\Delta P \cos\theta}{c} \frac{1}{M(2\pi f)^2}, \tag{4.12}$$

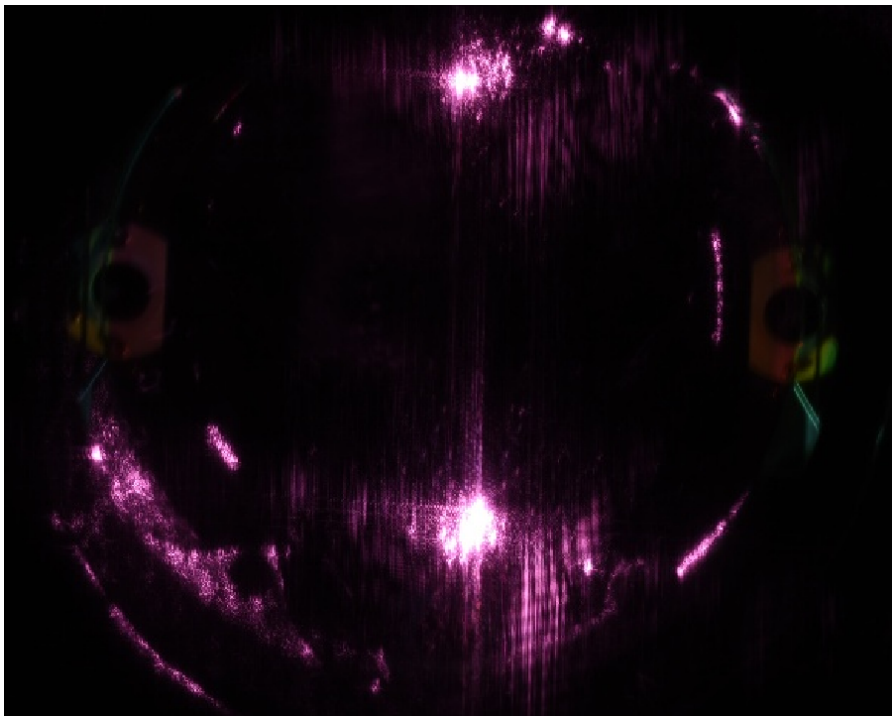

FIGURE 4.30: Picture of two Pcal beams taken by Tcam

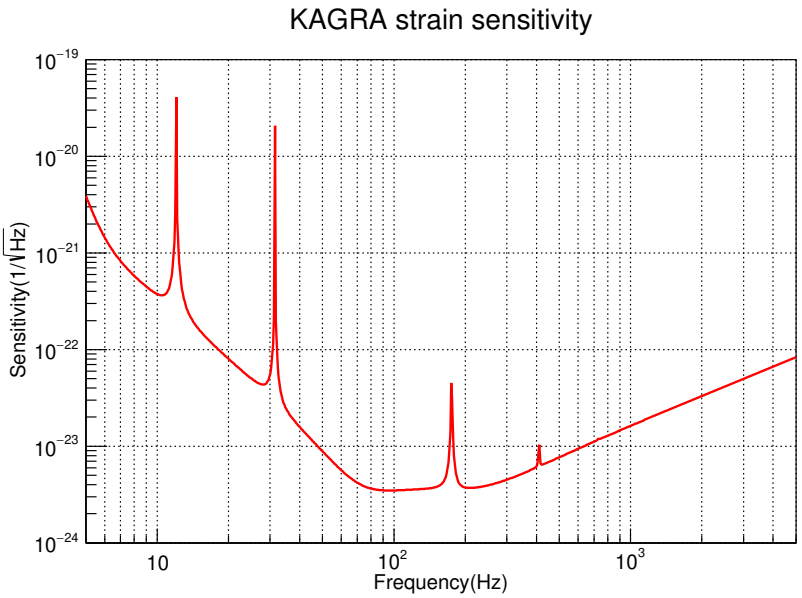

FIGURE 4.31: Target strain sensitivity of KAGRA

where ΔP is the modulated amplitude of laser, c is the speed of light in vacuum, θ is the incident angle of end test mass, M is the mass of end test mass, and f is the modulated frequency. The first term in the right-hand side expresses the force of the laser beam, and the second term is the transfer function from laser force to the mirror displacement.

The minimum displacement of end test mass sensed by KAGRA is

$$L(f) = h(f)L, \tag{4.13}$$

where $h(f)$ is the strain sensitivity of KAGRA, and the L is the arm-length of KAGRA interferometer. We require the noise of our photon Calibrator to be less than one-tenth of KAGRA target strain sensitivity. That is,

$$\Delta x(f) < \frac{1}{10} h(f)L \tag{4.14}$$

then we can get the noise requirement of photon Calibrator is

$$\Delta P < \frac{Mc(2\pi f)^2 L}{20\cos\theta} h(f) \tag{4.15}$$

, and the relative power noise (RPN) of the photon Calibrator is

$$\mathrm{RPN} \equiv \frac{\Delta P}{P} = \frac{Mc(2\pi f)^2 L}{20P\cos\theta} h(f). \tag{4.16}$$

Eq. 4.16 is the relative power noise requirement of our photon Calibrator. The parameters used in Eq. 4.16 is listed in Table. 4.1. Using KAGRA sensitivity in Fig. 4.31, we can get the requirement of relative power noise as shown in Fig. 4.32.

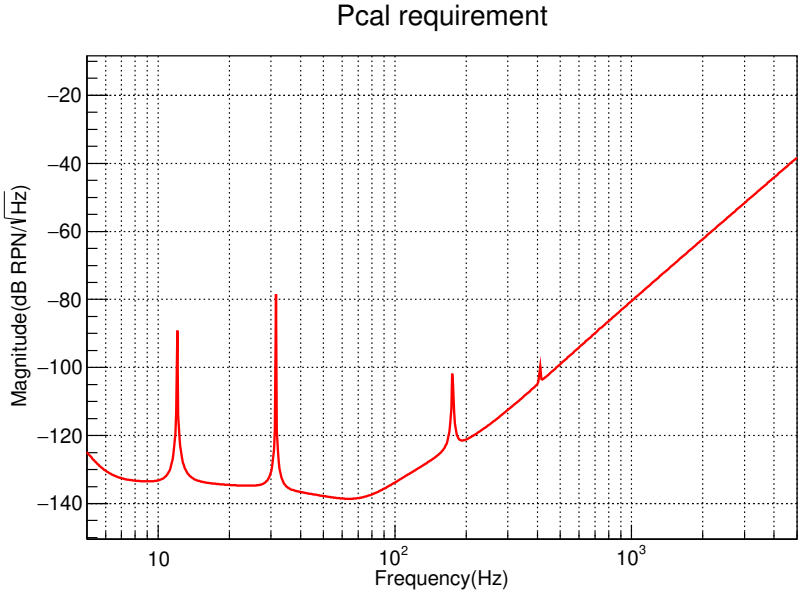

FIGURE 4.32: RPN Requirement of Pcal

4.7 Summary

In this chapter we introduced various calibration method and explain the reason why we need the photon Calibrator for calibration. Next, we introduce the how Pcal works, and then introduced Tx module, Rx module, Periscopes, and Tcam in the Pcal. For each module, we explain the function of each optical component, and give the specification of each optical component. Finally, we showed how to calculate the requirement of Pcal laser from sensitivity of KAGRA, and understand that we need to achieve the relative power noise level to below the calculated requirement.

Chapter 5

Optical Characterization for Power Stabilization System

5.1 Introduction

In this chapter, we calculate the beam width requirement of AOM and ETM, and measure the beam profile at these two positions. PCal uses AOM to modulate laser power. The optical rise time of AOM depends on laser beam width. For a beam size is 250 μm, the optical rise time is 77 ns. When the beam width increases to 0.75 μm, the optical rise time will increase to 230 ns. In order to decrease the optical rise time, we require the laser beam width at AOM to be 250 μm. Furthermore, we put the beam waist at ETM to maximize the mirror modulating efficiency. Since the Pcal beam is gaussian beam, the smaller the beam waist, the larger the divergence angle, which makes the beam size at Tx module become large, and we need to use large mirror or lenses, which is not very convenient. Therefore, by optimized beam width at ETM, the required beam width is 3.5 mm. Fig. 5.1 shows the schematic of optical characterization.

To achieve the required beam waist, first we characterize the laser, measure the output power and the beam profile of the laser to ensure our laser beam is gaussian beam. We already showed the result of power measurement in Sec. 4.3.1. Next, we check the laser beam profile using beam profiler. After we make sure that laser works as same as the specification, we calculate the modematching for AOM and ETM. To match the beam width requirement for AOM and ETM, we use JamMt software to calculate the specification of the lenses we need, and the position where it should be placed. After place the lenses, we measure the beam profile for AOM and ETM to characterize the beam width with our requirements.

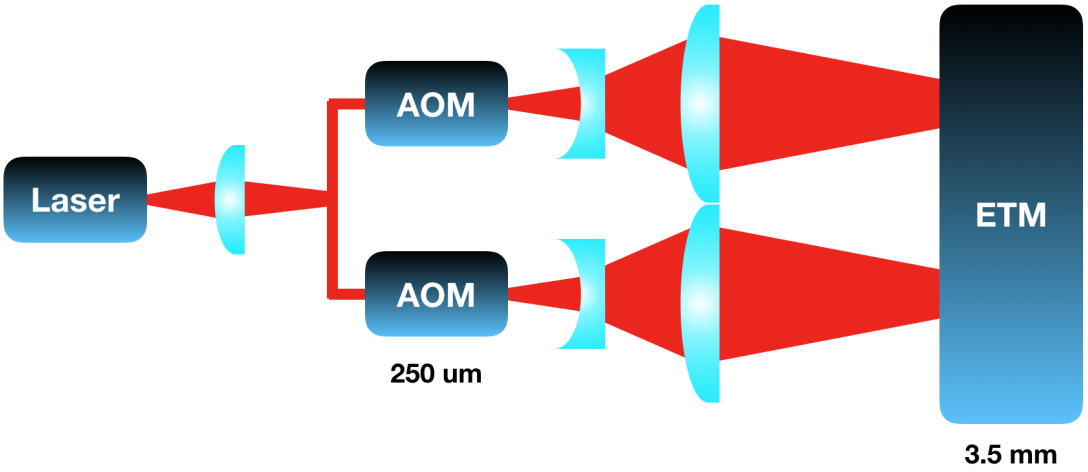

FIGURE 5.1: Schematic of optical characterization

In Sec. 5.2 we measure the beam profile of our laser. In Sec. 5.3 we use a software called JamMt to calculate the position and the focal length of the lenses. Then we measured the beam profile around AOM in Sec. 5.4, and the beam profile around ETM in Sec. 5.5.

5.2 Beam Profile

To measure the beam profile of our laser, we use two different type of beam profiler. One is BP209-VIS/M scanning-slit optical beam profiler made by Thorlabs [39], and the picture is shown in Fig. 5.2. The other is 13SKP501 tomographic beam profiler made by Melles Griot, and the picture is shown in Fig. 5.3. For the Thorlabs beam profiler, the beam diameter range of the beam sampler is 2.5 μm - 9 mm. The power limit of the beam sampler is shown in Fig. 5.4 [40]. On the other hands, the Melles Griot beam profiler is a old beam profiler which was produced over than 10 years ago, and we could not find the specification on the Melles Griot website.

.

For beam diameter at 500 μm, the maximum power limit of Thorlabs beam profiler is 0.6 W. Fig. 5.5 is the working screen of the beam profiler. The left table shows the beam position and beam width, the middle-top and right-top graph show the beam profile in x-axis and in y-axis, the middle-bottom graph shows the 3D beam profile, and the right bottom graph shows the 2D reconstruction beam profile.

In principle, the electric field of laser beam is in Gaussian distribution, which can be described as

FIGURE 5.2: Thorlabs BP209-VIS/M scanning-slit optical beam profiler

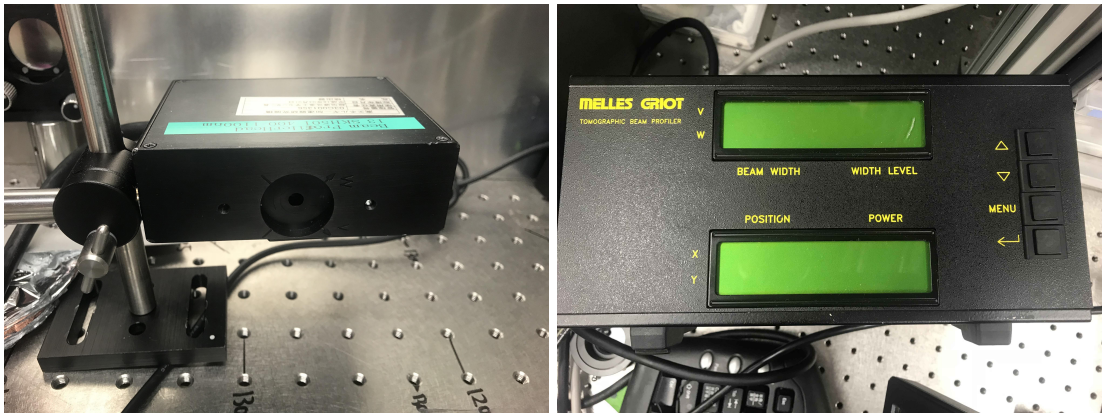

FIGURE 5.3: Melles Griot 13SKP501 tomographic beam profiler

$$P(x,z) = P_0 \mathrm{e}^{-\frac{2(x-r)^2}{w^2}} \tag{5.1}$$

where P_0 is the peak intensity, r is the beam position and $w(z)$ is the beam width. When circle of radius $x - r = w$, the ratio between that radius point and the peak is

$$\frac{P(x,z)}{P_0} = \mathrm{e}^{-2} = 0.135 = 13.5\% \tag{5.2}$$

Therefore, we take the 13.5 percent of the intensity peak as beam width. For the position at z along the beam (measured from the focus), the spot size w is given by

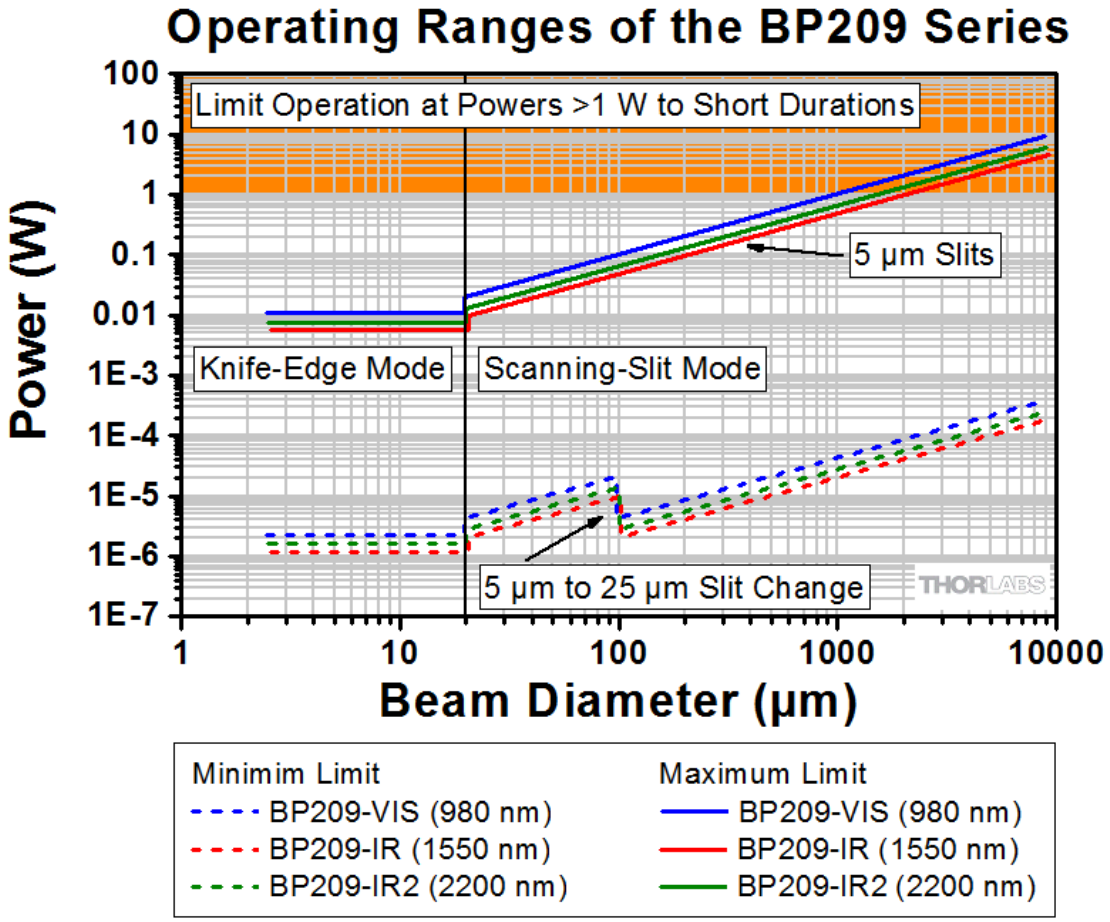

FIGURE 5.4: The power restriction of beam profiler

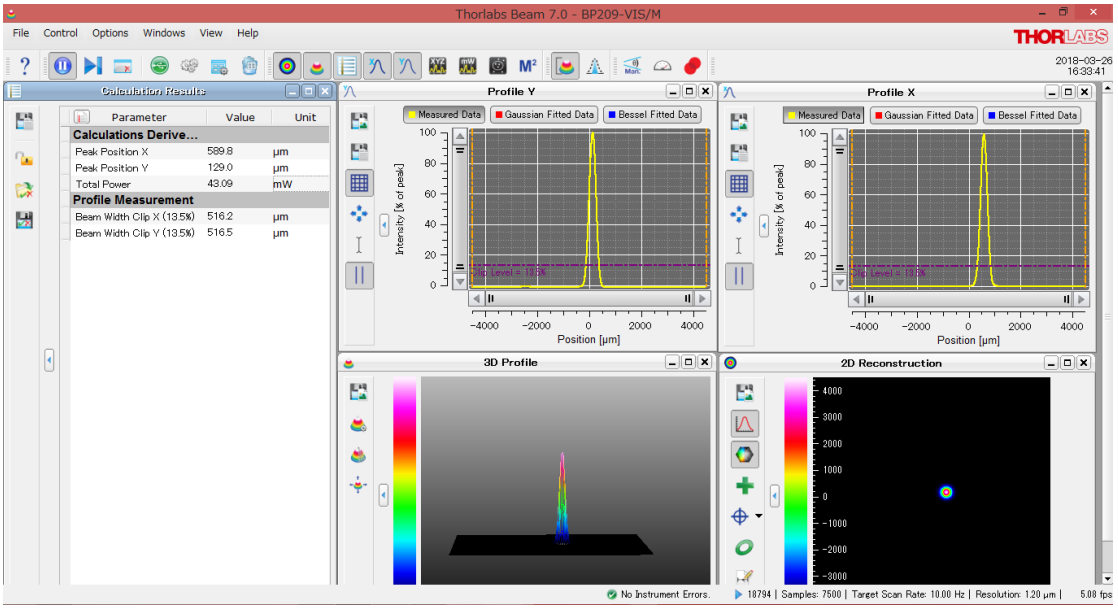

FIGURE 5.5: The screen of beam profiler

$$w(z) = w_0\sqrt{1+\left(\frac{z}{z_R}\right)^2} \tag{5.3}$$

$$= w_0\sqrt{1+\left(\frac{\lambda z}{\pi w_0^2}\right)^2} \tag{5.4}$$

where

$$z_R = \frac{\pi w_0^2}{\lambda} \tag{5.5}$$

is called the Rayleigh range, and the λ is the wave length of the laser. However, the practical laser beam might not be a ideal laser beam. Therefore, we use beam quality factor M^2 to describe the variance of laser beam. For the ideal laser beam, the beam quality factor is unity. We fit not only the beam width, but also the focus position z_0 and beam quality factor M^2. The fitting function can be written as

$$w(z) = w_0\sqrt{1 + \left(\frac{\lambda(z - z_0)M^2}{\pi w_0^2}\right)^2} \tag{5.6}$$

Measurement setup: I mount the beam profiler on a optical stand which can adjust the horizontal and vertical position, and connect the beam profiler to a computer. I mount the beam profiler at each different position on the laser path, and measure the beam profile and beam width. Since the beam profiler cannot receive the power larger than 0.6 W, we rotated the half-wave plate to reduce the laser power to below 0.6 W. When beam profiler received the laser beam, we can directly see the beam profile on the computer screen. We can also see the 13.5% beam width data, which we want to record, on the screen as shown in Fig. 5.5. After collecting the beam width data at each different point, I used Eq. 5.6 to fit the beam width in horizontal axis and vertical axis. The beam profile result measured by Thorlabs beam profiler is shown in Fig. 5.6, and the beam profile measured by Melles Griot beam profiler is shown in Fig. 5.7.

From the measured result, the horizontal and vertical axis beam width value are consistent in Thorlabs beam profiler, but two value are slightly different from Melles Griot beam profiler result. Since the beam profiler of Melles Griot is large, inconvenient to be placed in the optical system, and not easy to mount it perfectly perpendicular to the beam from the beam profiler stand. Therefore, we use the Thorlabs beam profiler in the following measurement. The beam width of the laser is 265 μm, and we use this value for the mode matching of AOM and ETM.

5.3 Mode Matching and JAMMT

The beam width requirement of AOM is 250 μm. After understanding the beam width, we need to know where to place the lens and AOM. We used JamMT (Just another mode matching tool), which is a JAVA mode matching tool, to do mode matching [41].

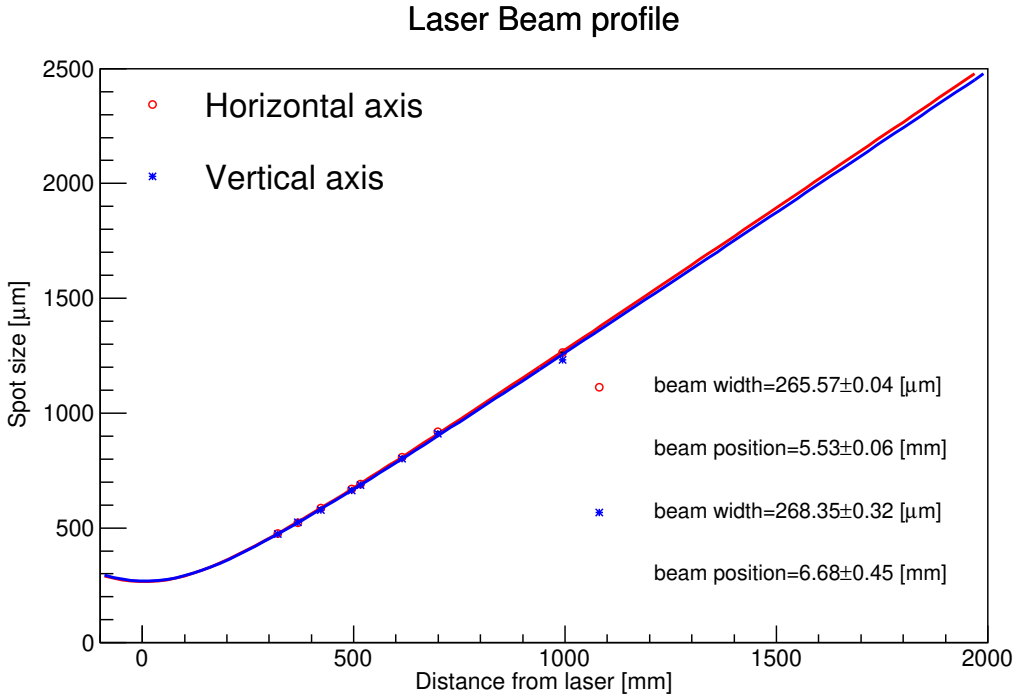

FIGURE 5.6: Beam profile of laser (Thorlabs)

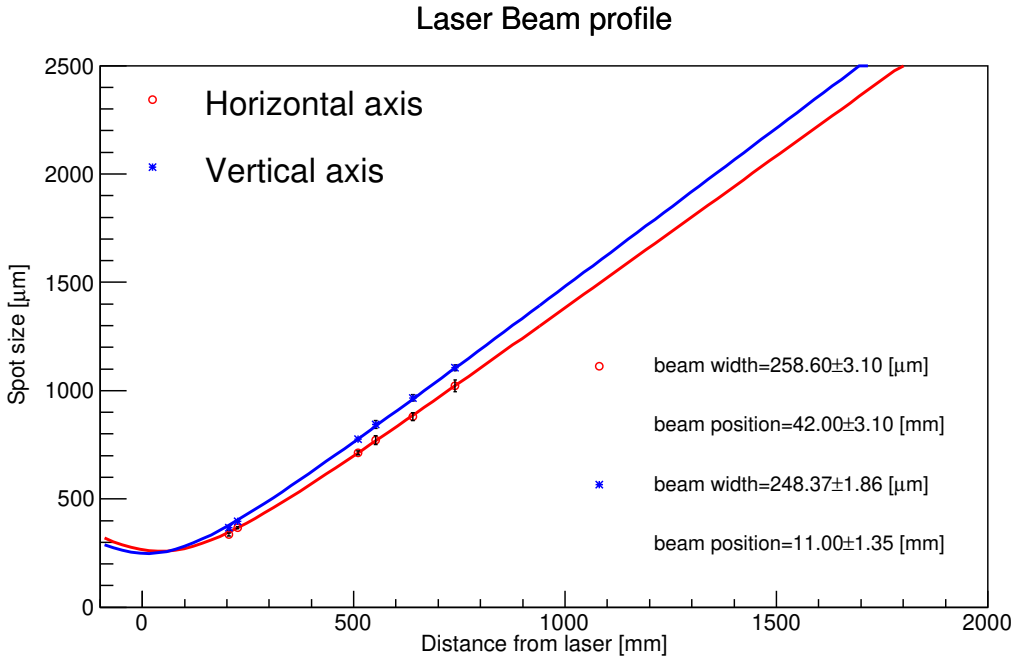

FIGURE 5.7: Beam profile of laser (Melles Griot)

For the first mode matching to AOM. we decided to use one 1-inch positive lens which is made by CVI laser optics. The mode matching result is shown below.

The mode matching result shows that if we place PLCX-25.4-99.9-UV-1053 lens, whose focus is 229.077 mm, at the z=361 mm position, the beam waist would be 250.086 μm

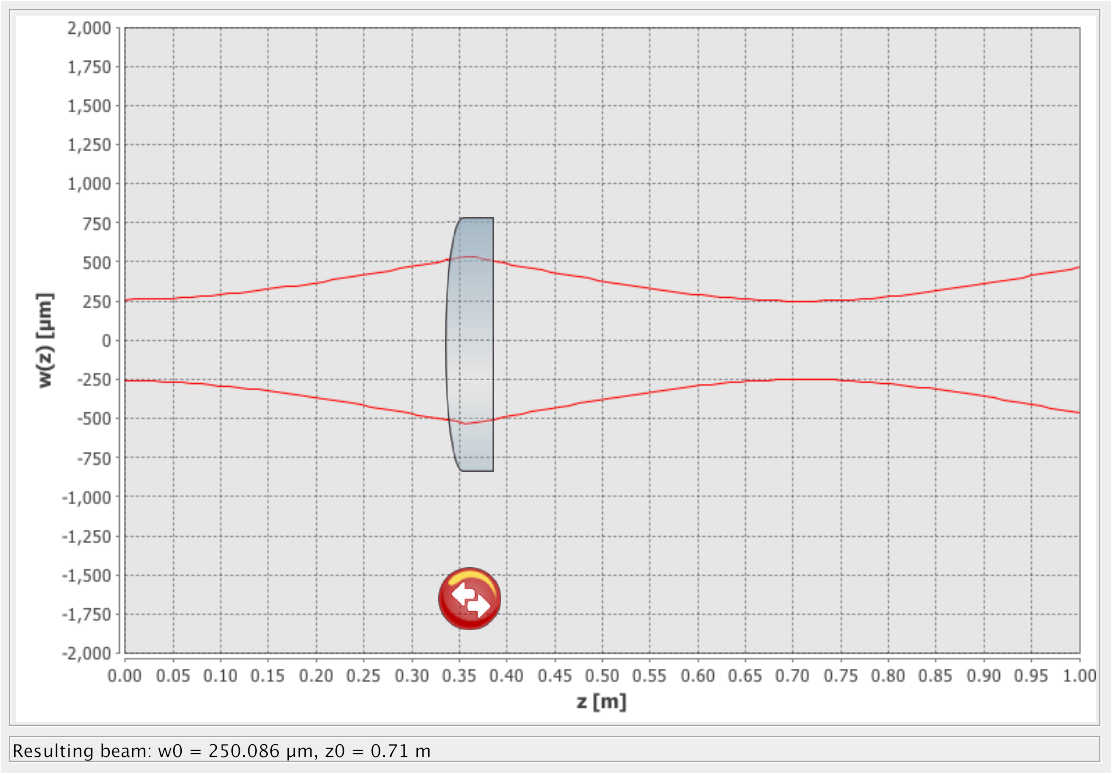

FIGURE 5.8: JamMT mode matching of AOM

at the z=710 mm position. Therefore the AOM should be placed in z=710 mm position.

Beside AOM, we also need to do the mode matching for end test mass. The laser beam at end test mass should be the beam waist. Since laser beam is gaussian beam, the smaller the beam waist, the larger the beam divergence angle. If we use the small beam waist at the end test mass, then the beam width at the transmitter module would be large, and we need to use large mirror in our transmitter module. Since the large mirror is expensive and inconvenient to setup, we need to make the beam width at trasmitter module as small as possible. The Gaussian beam spot size can be described as

$$w(z) = w_0\sqrt{1+\left(\frac{\lambda z}{\pi w_0^2}\right)^2} \tag{5.7}$$

The minimum beam spot at 36 m can be written by

$$\left.\frac{dw(z)}{dw_0}\right|_{z=36\mathrm{m}} = 0. \tag{5.8}$$

From Eq. 5.7 and Eq. 5.8, we can get the minimum beam waist at end test mass is

$$-\frac{2w_0\left(\frac{\lambda z}{\pi w_0^2}\right)\frac{\lambda z}{\pi w_0^3}}{\sqrt{1+\left(\frac{\lambda z}{\pi w_0^2}\right)^2}}+\sqrt{1+\left(\frac{\lambda z}{\pi w_0^2}\right)^2}\Bigg|_{z=36\text{m}}=0 \tag{5.9}$$

$$\frac{2\lambda^2 z^2}{\pi^2 w_0^4}=1+\left(\frac{\lambda z}{\pi w_0^2}\right)^2\Bigg|_{z=36\text{m}} \tag{5.10}$$

$$w_0=\sqrt{\frac{\lambda z}{\pi}}\Bigg|_{z=36m}=3.46\text{mm}\div 3.5\text{mm}. \tag{5.11}$$

Therefore, from Eq. 5.11, we require the beam waist at test mass is 3.5 mm, and we use 1-inch negative lens and 2-inch positive lens to do this mode-matching.

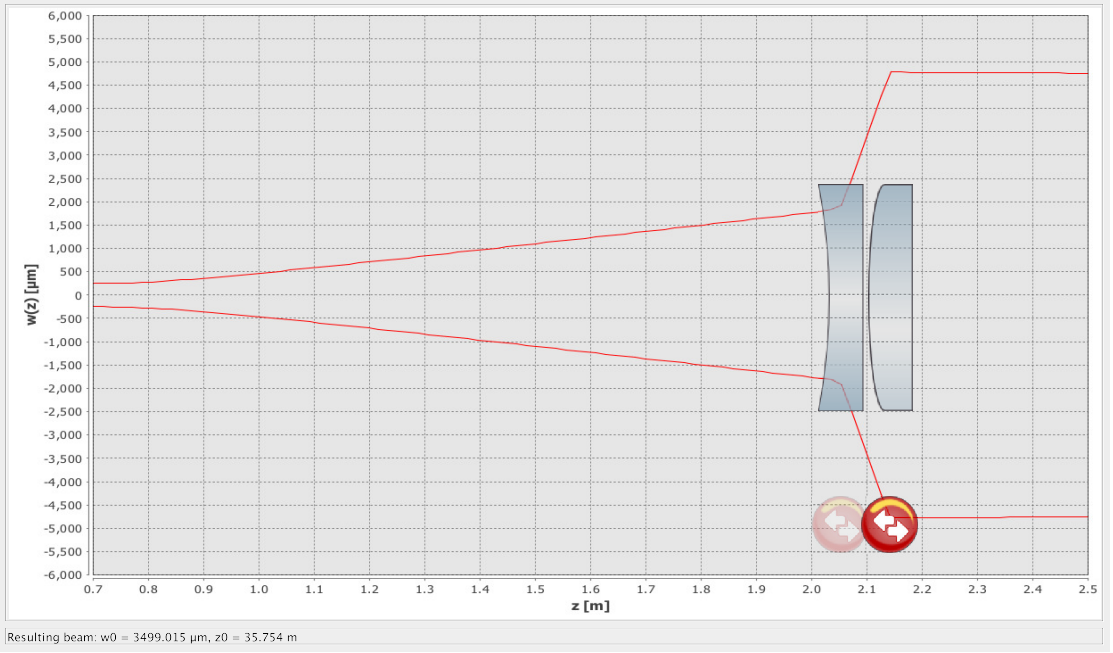

FIGURE 5.9: JamMT mode matching of ETM

The mode matching result shows that if we place PLCC-25.4-25.8-UV-1047 one negative lens, whose focus is -57.38 mm, at the z=2136 mm position, and place PLCX-50.8-62.5-UV-1047 positive lens, whose focus is 143.22 mm, at the z=2226 mm position, the beam waist would be 3.499 mm at the z=35.754 m position. Therefore we should place the negative and positive lenses at the simulated position and measure the beam waist. The schematic of beam waist is shown in Fig. 5.10

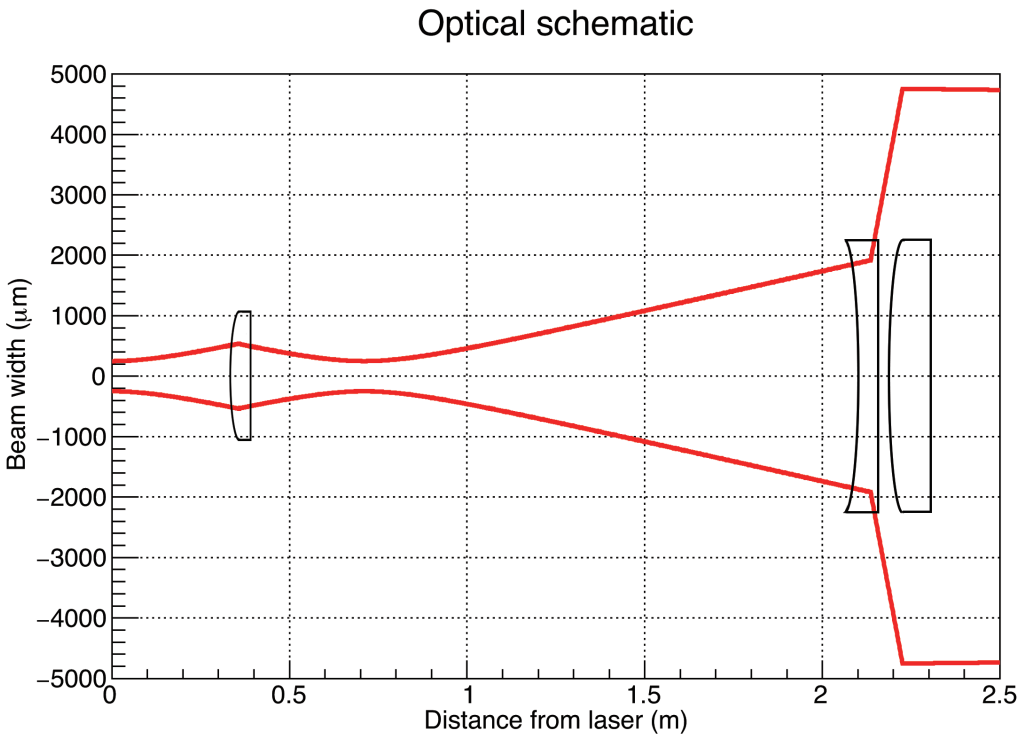

FIGURE 5.10: Schematic of Pcal beam width

5.4 Beam profile around AOM

After we place a PLCX-25.4-99.9-UV-1053 positive lens to focus the beam, we need to measure the beam profile at the AOM position. In order to measure the beam quality, it is necessary to measure the beam width at the focus position. The measured result is shown in Fig. 5.11 and Fig. 5.12.

From the result, the beam width is focused at the desire value, i.e. 250 μm, and the beam quality is closed to the given value 1.1. We found that the error of beam profile in vertical axis is larger than in horizontal axis. We investigate it by collecting beam profile data with 60 times and plot it into histogram. Fig. 5.13 show the histrogram of beam profile. From the result, we can see that in X axis, there is one peak in the graph, but for the y axis there are two peaks. These two peaks affect the fitting result of the gaussian beam and cause the larger error than X axis. We suspect this two peaks effect come from the beam profiler itself. The actual reason need more investigation.

As a result, the beam profile of the laser and the information of the lens is summarized in the Table. 5.1 and Table. 5.2.

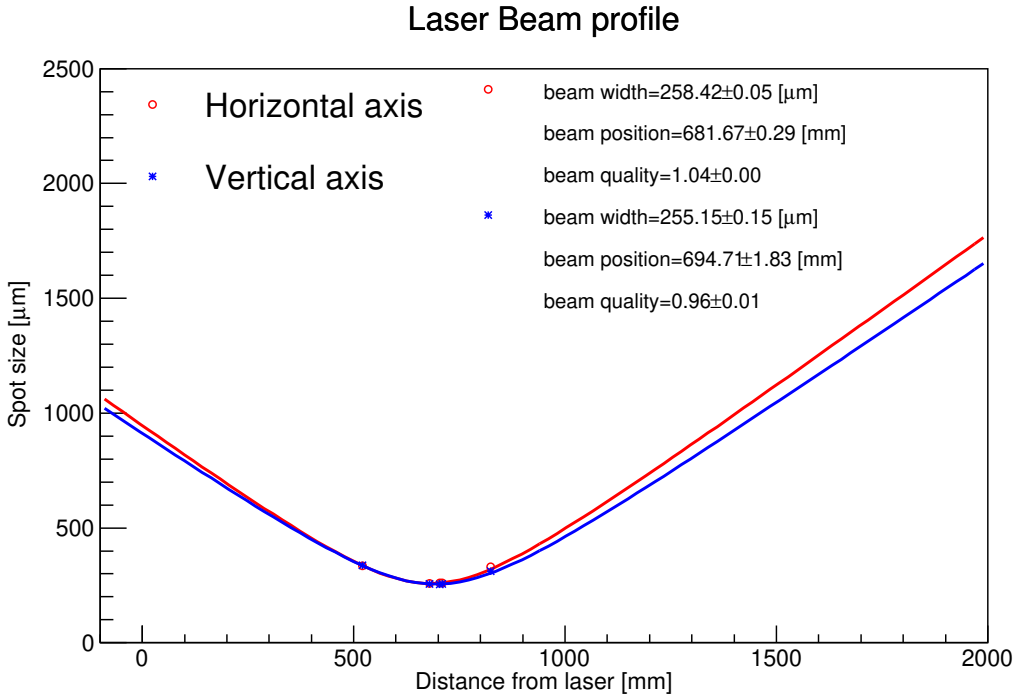

FIGURE 5.11: Beam profile around AOM position (Path1)

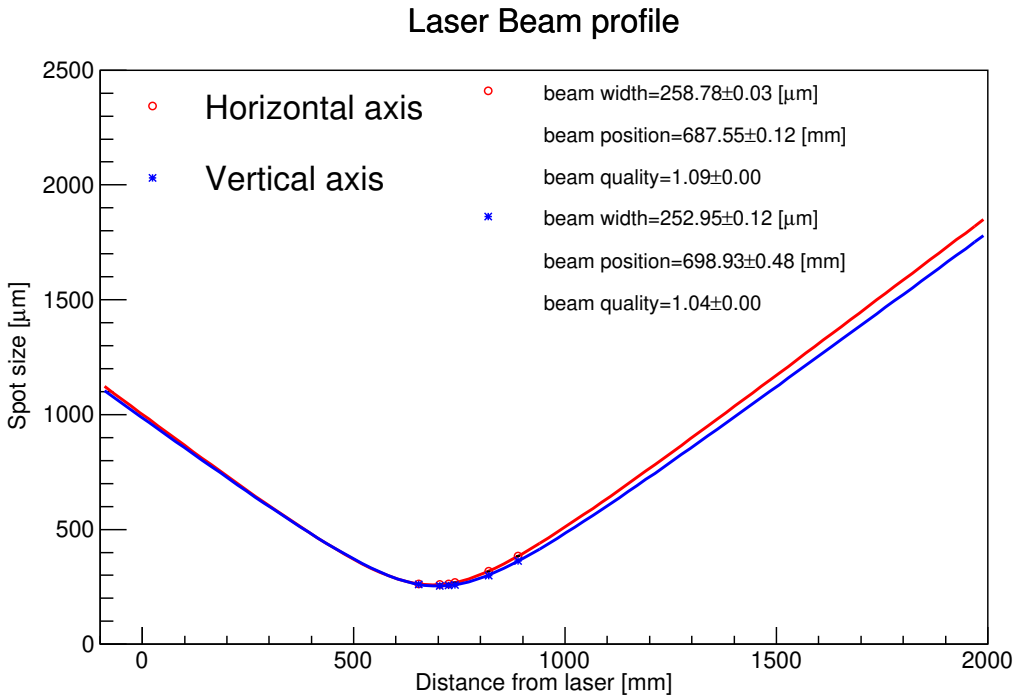

FIGURE 5.12: Beam profile around AOM position (Path2)

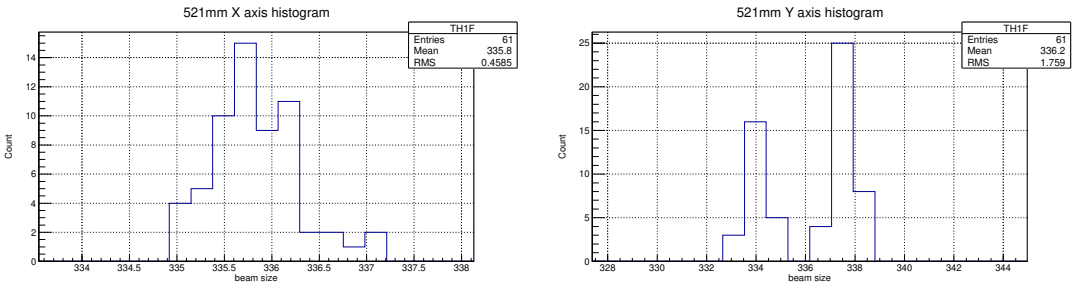

FIGURE 5.13: Histogram of beam profile data with 60 data

Characteristic	Path1	Path2
Laser beam width H axis	265.57±0.04 μm	
Laser beam width V axis	268.35±0.32 μm	
Beam width at AOM position H axis	258.41±0.04 μm	258.78±0.03 μm
Beam width at AOM position V axis	255.14±0.15 μm	252.95±0.12 μm
Beam quality H axis	1.03±0.00	1.09±0.00
Beam quality V axis	0.96±0.01	1.04±0.00

TABLE 5.1: Beam Profile of laser

Part number	Diameter (mm)	Focal length (mm)	z(mm)	ω_0 (mm)
PLCX-25.4-99.9-UV-1053	25.4	229.077	361	0.25
PLCC-25.4-25.8-UV-1047	25.4	-57.38	2136	-
PLCX-50.8-62.5-UV-1047	50.8	143.22	2226	3.5

TABLE 5.2: Specification of the lenses

5.5 Beam profile of 72 meter optics

5.5.1 Overview

From Eq. 5.11 and Fig. 5.9 we expect to have 3.5 mm beam waist at the 35.7 m position, and 5 mm. We want to check whether our system is consistent with the designed value or not. Therefore, when we measured the laser power map at five positions in Sec. 7.2, we also measured the beam profile at the same time.

5.5.2 Setup

We mounted the beam profile at 1. Tx module, 2. EYA chamber (Tx side), 3. EYC chamber (ETM), 4. EYA chamber (Rx side), 5. Rx module. The position is shown in Fig. 5.14.

We measured the beam profile 10 times with 5 second time interval. We average 10 data and calculate the mean and the standard deviation of the beam profile. The aperture size of our beam profiler is 9 mm, however, there is an area which could not detect

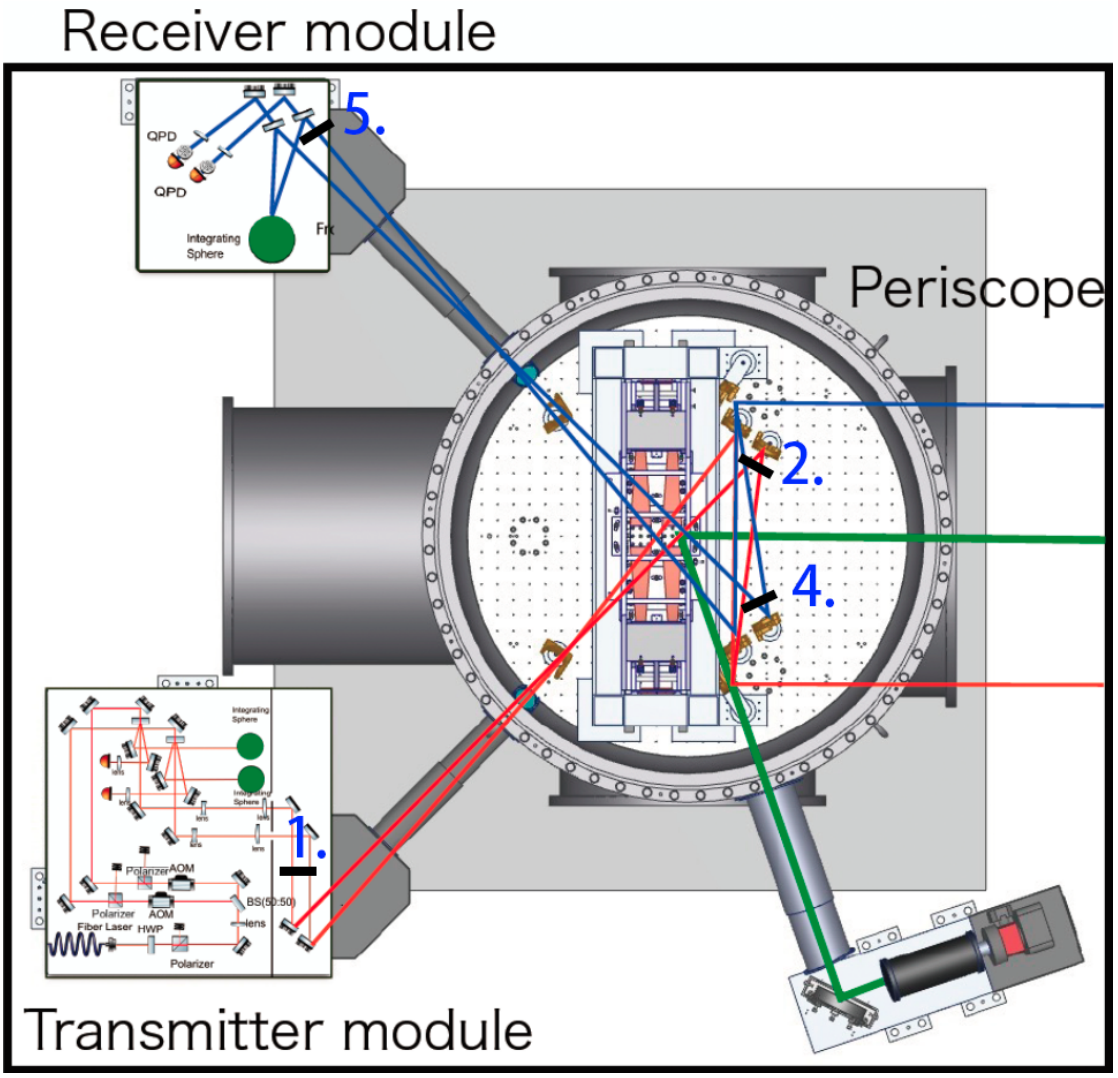

FIGURE 5.14: Measure positions at EYA chamber

laser power due to some instrument issue, so the usable region of the beam profiler is about 5 mm. Since our beam diameter is larger than 5mm (the smallest beam radius on EYC is around 3.5 mm), we can only measure the beam profile around the peak, and use Gaussian distribution equation Eq. 5.1 to fit the peak amplitude, beam position and beam width. For x axis data, we fit the beam position from 0 μm to 4500 μm, on the other hand, for y axis, we fit the beam position from -4500 μm to 0 μm. This is because we can not use the region which could not detect the laser power for fitting, and the adjacent region also have some systematic error, since we can see the beam deformation at there After measuring beam width, I measured the distance between each measurement position and use Eq. 5.6 to fit the beam width for 72 meters optics.

5.5.3 Result

The result of beam profiles at each position are shown in Fig. 5.15, Fig. 5.16, Fig. 5.17, Fig. 5.18, Fig. 5.19. The distance from the laser output to each measurement position are listed in Table. 5.3

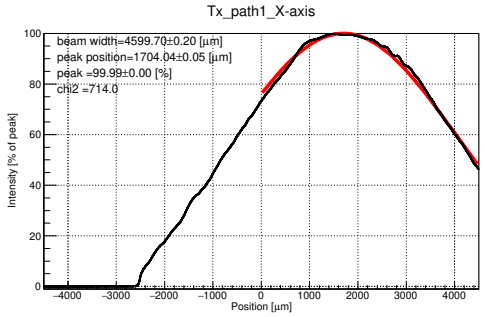

(a) Tx path1 x-axis

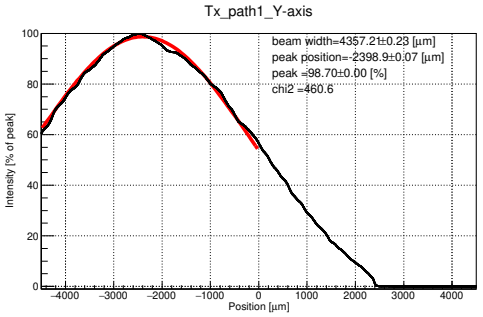

(b) Tx path1 y-axis

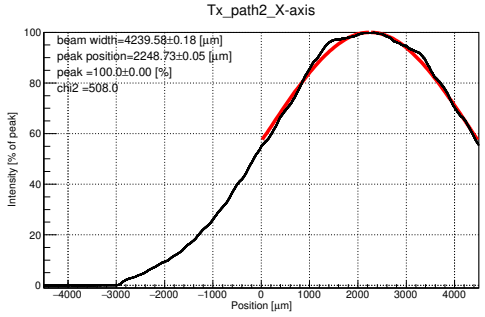

(c) Tx path2 x-axis

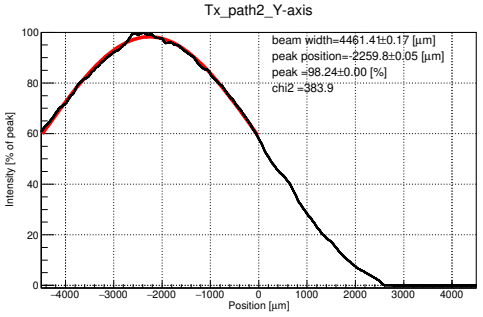

(d) Tx path2 y-axis

FIGURE 5.15: Tx Beam profile

	Path1 (m)	Path2 (m)
Tx	2.764	2.584
EYA(Tx)	5.626	3.855
EYC	41.479	41.149
EYA(Rx)	77.076	76.884
Rx	79.864	79.464

TABLE 5.3: Distance from the laser

From Fig. 5.15 and Fig. 5.16, we can find there is some wave structure at the peak of the beam at the Tx module and EYA(Tx side), but from Fig. 5.17 ,Fig. 5.18 and Fig. 5.19 we did not see this kind of wave structure. This phenomenon may cause by the reflection between two mode matching lenses. If there is some reflection between mode matching lenses, the reflected beam contaminate the peak of the beam, causing the wave structure at the peak. But for the beam at EYC and Rx module, since the

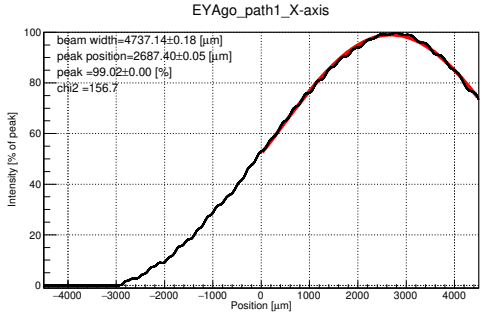

(a) EYA(Tx) path1 x-axis

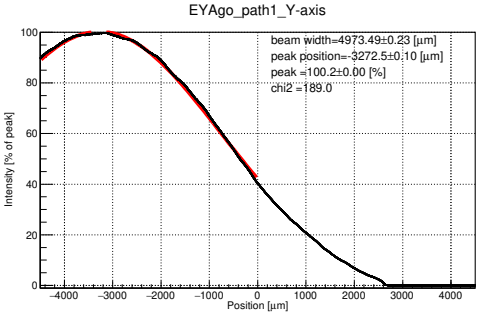

(b) EYA(Tx) path1 y-axis

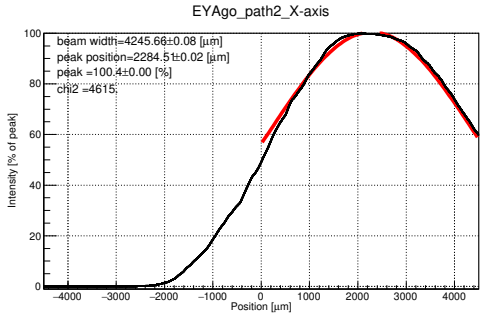

(c) EYA(Tx) path2 x-axis

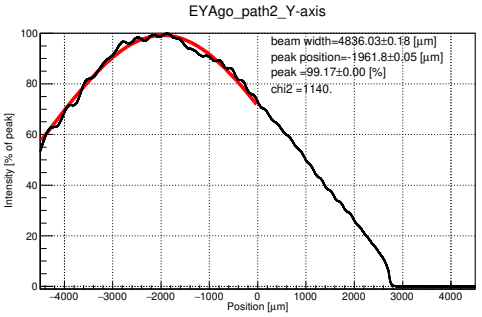

(d) EYA(Tx) path2 y-axis

FIGURE 5.16: EYA(Tx) Beam profile

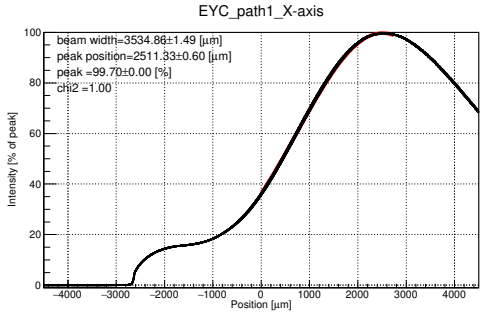

(a) EYC path1 x-axis

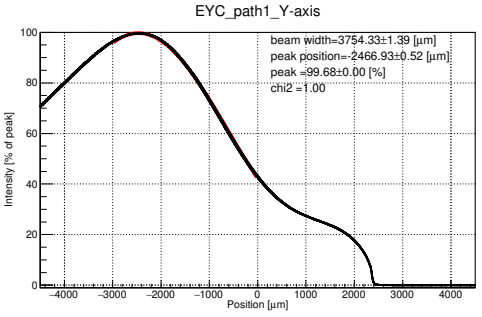

(b) EYC path1 y-axis

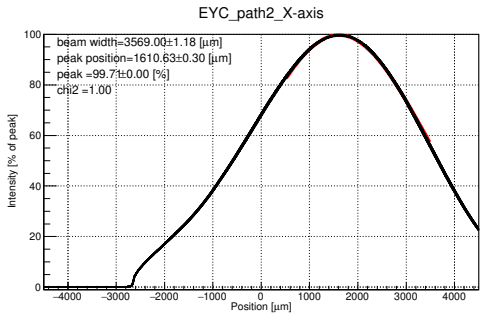

(c) EYC path2 x-axis

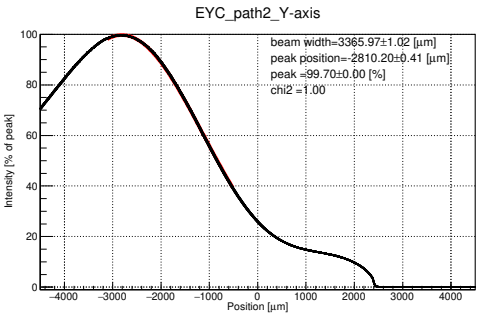

(d) EYC path2 y-axis

FIGURE 5.17: EYC Beam profile

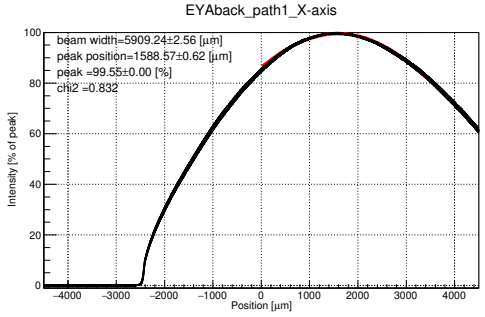

(a) EYA(Rx) path1 x-axis

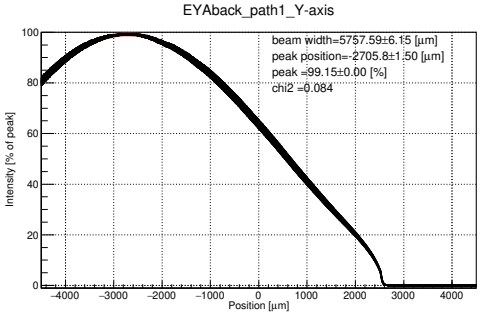

(b) EYA(Rx) path1 y-axis

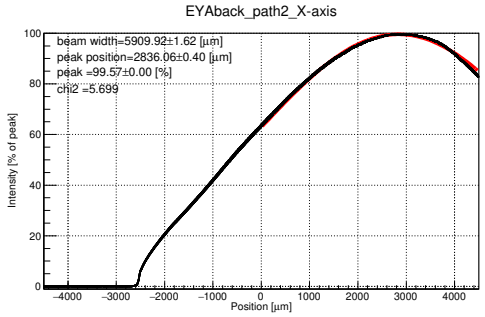

(c) EYA(Rx) path2 x-axis

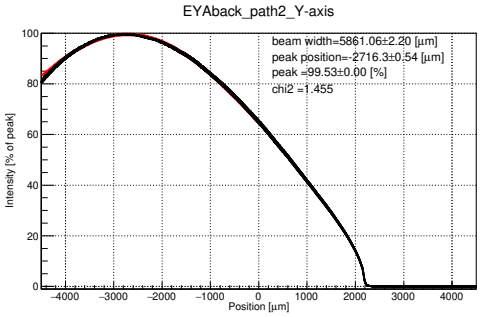

(d) EYA(Rx) path2 y-axis

FIGURE 5.18: EYA(Rx) Beam profile

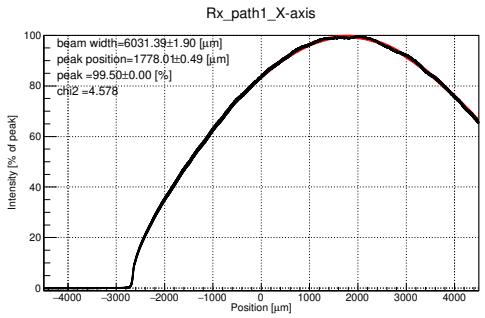

(a) Rx path1 x-axis

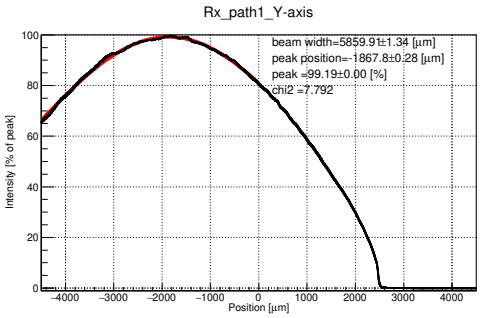

(b) Rx path1 y-axis

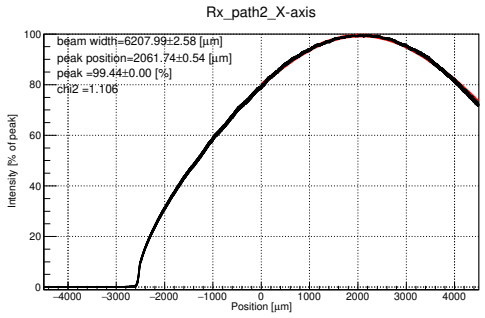

(c) Rx path2 x-axis

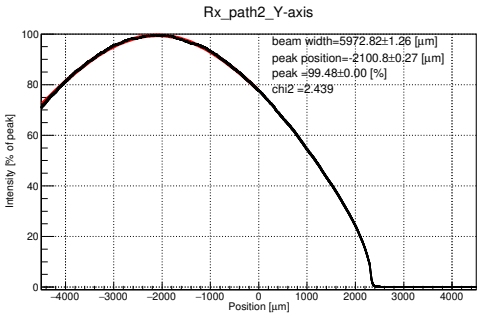

(d) Rx path2 y-axis

FIGURE 5.19: Rx Beam profile

distance is far away from Tx module, the wave structure at the peak spread out to large radius region. Therefore, we can see the Airy disk pattern in EYC, and Rx module.

Using beam profile data, Table. 5.3 and equation Eq. 5.6, we can make the plot of beam width.

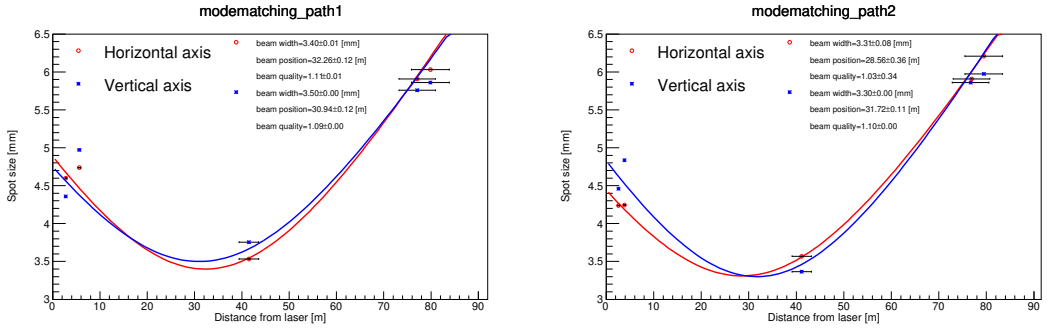

(a) Path1 (b) Path2

FIGURE 5.20: Beam width of 72 meters optics

5.6 Summary

The characteristic of the laser optics is discussed in this chapter. First show the reason why we have the beam profile requirement at the AOM and ETM position. Next, I measured the beam profile, checked the beam width of the laser. The beam waist of our laser is 265 μm. Then, I did the mode matching for the AOM and ETM, and calculated where the lenses should be placed. After that, I placed the lenses and measured the beam profile at the AOM position. The beam waist at the AOM position is around 250 μm, which meet the requirements. Finally, I measured the beam profile for 72 meters Photon Calibrator system, and showed the beam width at sapphire mirror position is around 3.5 mm, which match our requirement.

Chapter 6

Optical Follower Servo

6.1 Introduction

This chapter describes and discusses about a active controller called Optical Follower Servo (OFS), which is used for control and reduce the relative power noise of Pcal laser beam and the harmonic noise which results from the generation of sinusodial signals. We feedback the PD signal to injected signal and sent it to OFS to adjust gain and offset. The output of OFS controls AOM, which modulates laser power. The schematic of the OFS loop is shown in Fig. 6.1.

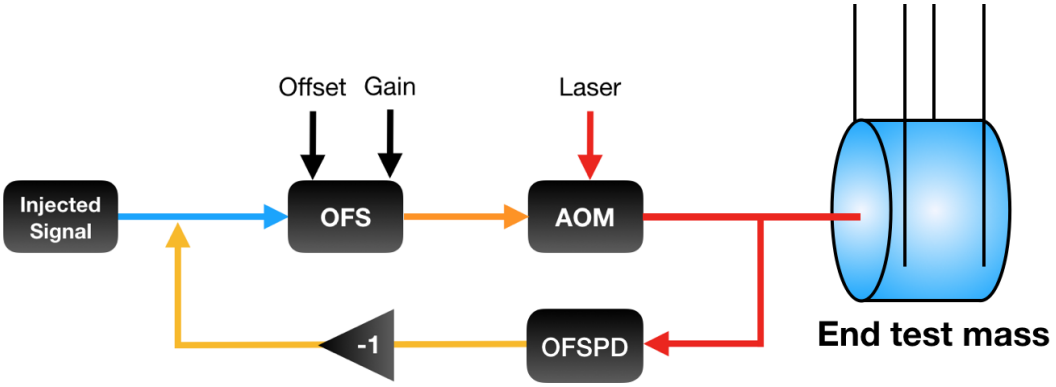

FIGURE 6.1: Schematic of OFS loop

The transfer function of this OFS circuit is shown in Fig. 6.2. The unity gain frequency (UGF) of this circuit is 8 kHz, which means OFS loop can be controlled below 8 kHz. The phase margin is 60 degrees, which assure the negative feedback loop being stable.

Optical Follower Servo consist of two part: Optical Follower Servo chassis itself and a Interface chassis. Optical Follower Servo chassis reduce the noise of the laser beam, and the Interface chassis send the readout signal of the detector to digital system for

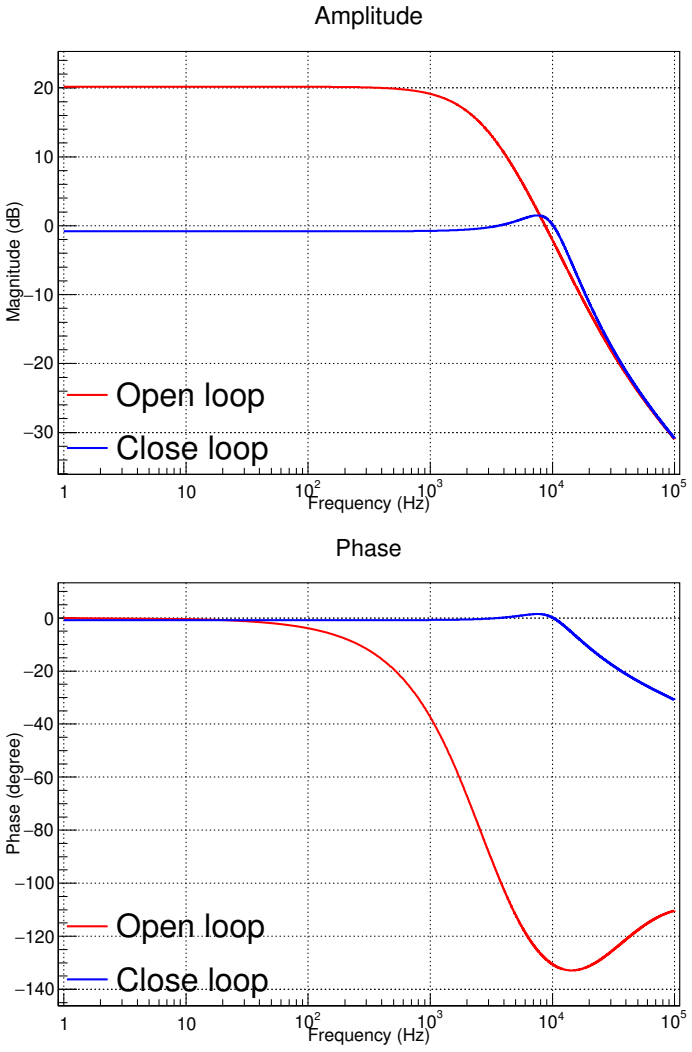

FIGURE 6.2: Transfer function of OFS

monitoring and saving the data. The OFS board is designed by the LIGO Pcal group [42][43][44][45], and we place the OFS board and interface board into OFS and Interface chassis as shown in Fig. 6.3.

This chapter is divided into five main sections. The first section we introduce OFS chassis and show the electric circuit and the pictures of OFS chassis. The second section we explain the circuit and listed up the test procedure of OFS chassis. The third section we introduce Interface chassis and show the electric circuit and the pictures of Interface chassis. The fourth section we explain the circuit and listed up the test procedure of Interface chassis. The fifth section is the measured result of the test procedure.

FIGURE 6.3: Optical Follower Servo and Interface chassis

6.2 Circuit of Optical Follower Servo

Optical Follower Servo board consist of front board and back board. Front board contains a variable gain amplifier, low-pass filters to remove the high frequency noises, and relay for switching the loop. Back board contains a set of regulator to generate the suitable voltage for operation amplifier and relay. Fig. 6.4 and Fig. 6.5 show the picture of OFS front board and back board. The circuit of OFS front board and back board is shown in the following pages. The detail of the circuit will be discussed in Sec. 6.3

6.3 Test of Optical Follower Servo

1. **DC test**

(a) We use ±18 V for the power supply in Optical Follower Servo (OFS). In order to provide ± 15V for the operational amplifier(opamp) and ± 12V for the relay, we use LM317 [46] and LM337 [47] regulator to control the output DC voltage and use LEDs as indicators.

The output voltage of LM317 could be adjusted from 1.25 V to 37 V, and the maximum output current is 1.5 A.Fig. 6.6 shows the operation method of LM317. It has 3 pins: V_{in}, V_{out}, and Adj. The voltage between V_{out}, and Adj is 1.25 V. This voltage generate a current, passing through R_H and R_L and reach the ground. Therefore, we can adjust the output voltage of LM317 by changing the value of R_H and R_L. Moreover, there is some non-negligible static current in *Adj* pin, so the output voltage of LM317 can be

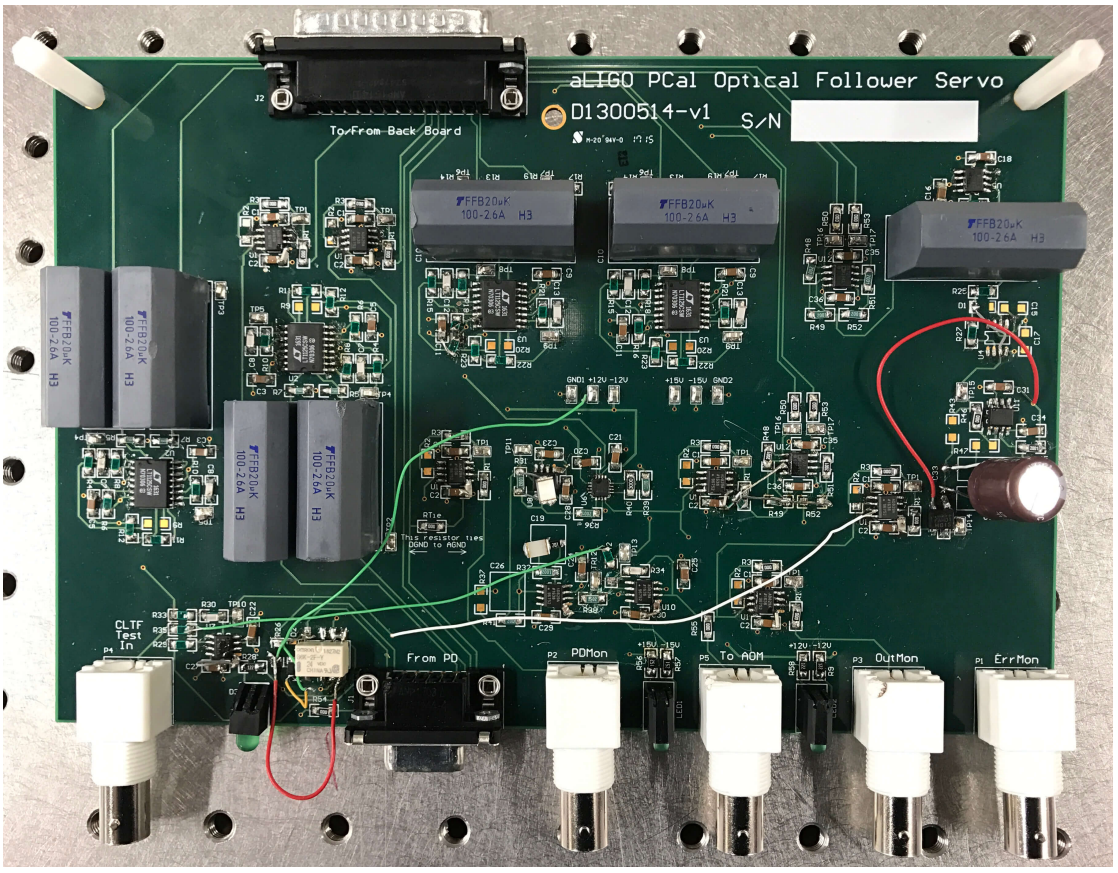

FIGURE 6.4: Optical Follower Servo front board

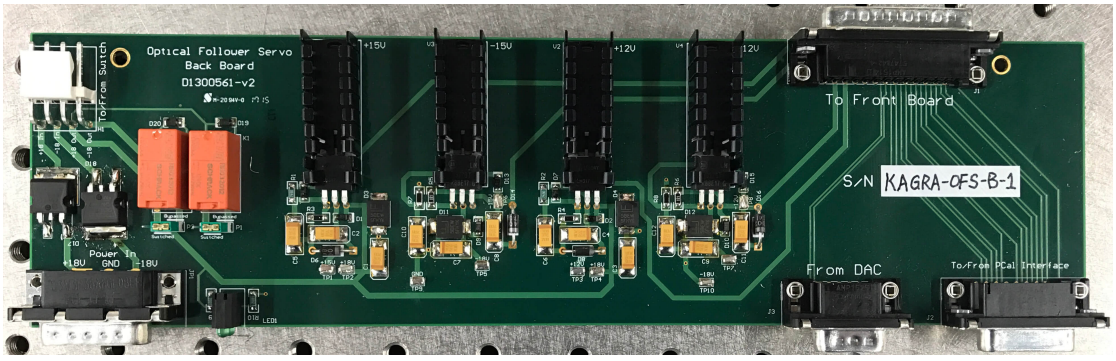

FIGURE 6.5: Optical Follower Servo back board

written as

$$V_{out} = 1.25(1 + \frac{R_L}{R_H}) + I_{Adj}R_L \tag{6.1}$$

For LM337, it is simply the inverse of LM317, so the output voltage of LM337 can be written as

$$V_{out} = -1.25(1 + \frac{R_L}{R_H}) + I_{Adj}R_L \tag{6.2}$$

Fig. 6.7 shows the circuit for generating ±15 V and ±12 V. Using Eq. 6.1 and Eq. 6.2,

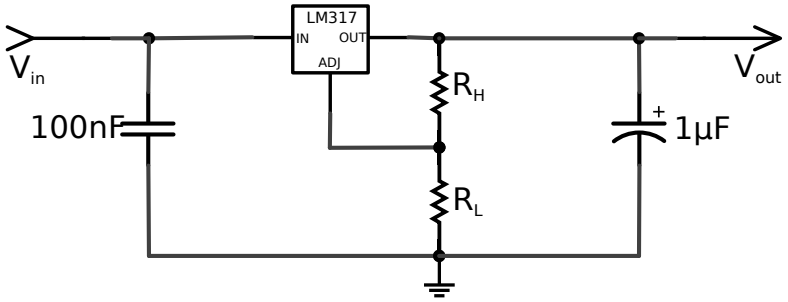

FIGURE 6.6: Operation method of LM317

we can calculate the output voltage from the circuit.

$$\begin{aligned}
\textbf{+15V:}\quad & 1.25 \times (1 + 2.67 \times 10^3/249) + 2.67 \times 10^3 \times 46 \times 10^{-6} && = 14.77\ [V] \\
\textbf{-15V:}\quad & -[1.25 \times (1 + 1.33 \times 10^3/120) + 1.33 \times 10^3 \times 65 \times 10^{-6}] && = -15.19\ [V] \\
\textbf{+12V:}\quad & 1.25 \times (1 + 2.1 \times 10^3/249) + 2.1 \times 10^3 \times 46 \times 10^{-6} && = 11.88\ [V] \\
\textbf{-12V:}\quad & -[1.25 \times (1 + 1.02 \times 10^3/120) + 1.02 \times 10^3 \times 65 \times 10^{-6}] && = -11.94\ [V]
\end{aligned} \tag{6.3}$$

Therefore, we are able to generate the ±15V and ±12V.

Next, we turned on the power supply, adjust DC voltage to ±18 V and checked the LED status of ±15 V and ±12 V in the front panel. The picture of LED is shown in Fig. 6.8

LED label	KEK		KAGRA	
	OFS1	OFS2	OFS1	OFS2
±15 V	on	on	on	on
±12 V	on	on	on	on

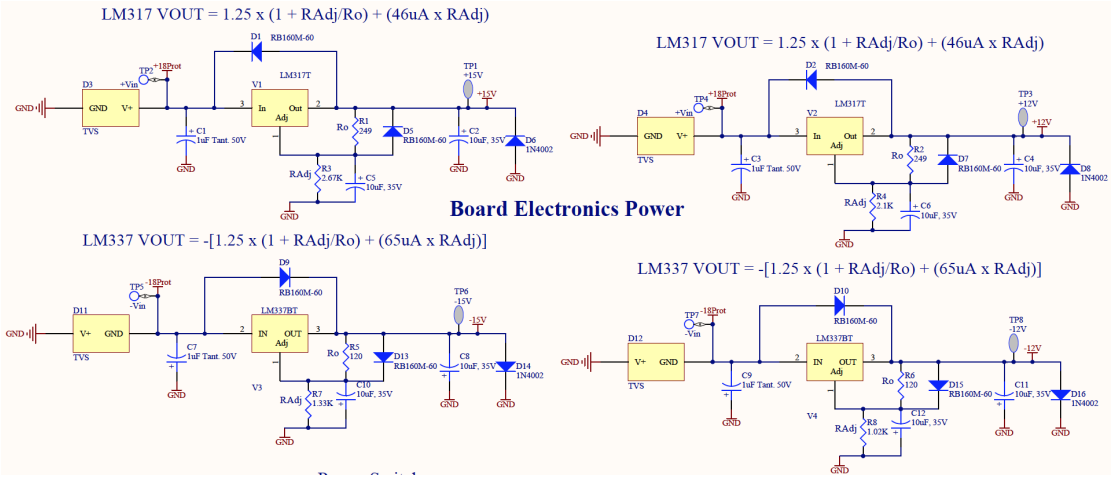

FIGURE 6.7: Circuit of DC voltage generating in OFS [43]

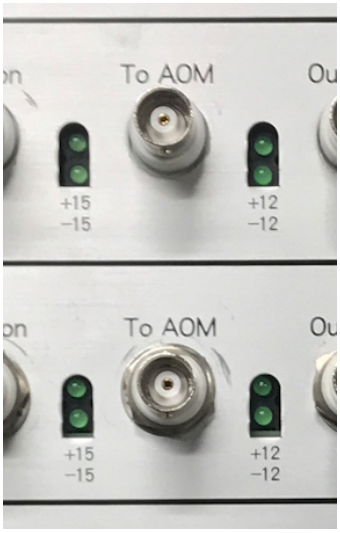

FIGURE 6.8: ±15 V and ±12 V LED in OFS board

(b) To enable the photodetector circuit, we simply provide ±15 V output for the opamp in the photodetector from the LM317 and LM337. We check whether we can receive ±15 V from photodetector power supply connector.

PD power supply	**KEK**		**KAGRA**	
	OFS1	OFS2	OFS1	OFS2
+15 V	14.81 V	14.81 V	14.81 V	14.81 V
-15 V	-14.99 V	-15.03 V	14.98 V	15.03 V

(c) **Loop Switch test:**

We use a dual-pole-dual-throw (DPDT) relay to control the switch of the loop in OFS. The circuit of relay is shown in Fig. 6.9. When the closed-loop configuration is set, the the loop LED will be lightened, and we will read 12 V at loop switch response port.

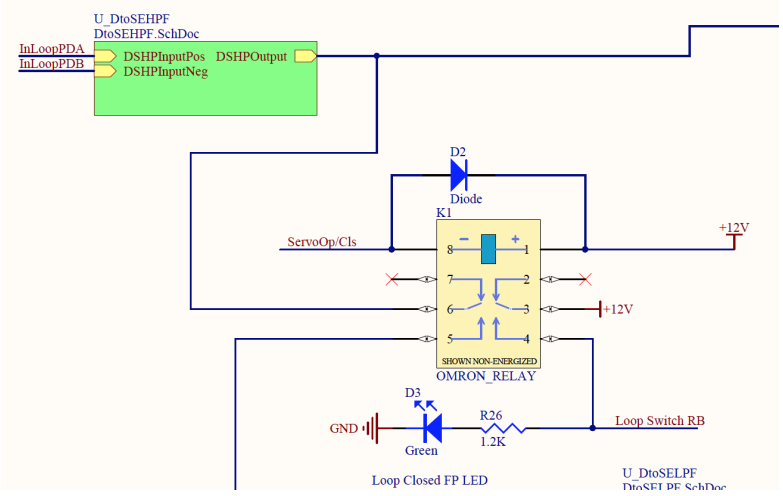

FIGURE 6.9: OFS loop relay [42]

Loop closed	**KEK**		**KAGRA**	
	OFS1	OFS2	OFS1	OFS2
Loop LED	on	on	on	on
Loop response	11.90 V	11.90 V	11.87 V	11.90 V

2. **Functional Tests**

(a) **PD Signal Tests:**

In this part we test the monitor of PD signal and the transfer function from PD to OFS output. Fig. 6.10 shows the circuit of this part. We send the swept sine signal from input of PD. We use voltage followers to send the PD signal to a BNC connector. Fig. 6.11 shows the circuit of voltage follower. The output voltage directly follows the input voltage. The advantage of using voltage follower is that voltage follower has high input impedance, which draws very little current and does not disturb the original circuit. Therefore, the readout signal of PD monitor should be identical as PD signal.

In the next stage, a inverting amplifier is used for summing the signal of PD, offset, and excitation signal. Fig. 6.12 shows the circuit of inverting amplifier. The output signal of the inverting amplifier is given as

$$V_{\text{out}} = -\frac{R_{\text{f}}}{R_{\text{in}}} V_{\text{in}} \tag{6.4}$$

In our circuit, $R_{\text{f}} = R_{\text{in}} = 5k\Omega$, so the gain is unity and phase is inverted. This signal is sent to error monitor to monitor the summation of PD, offset, and excitation signal.

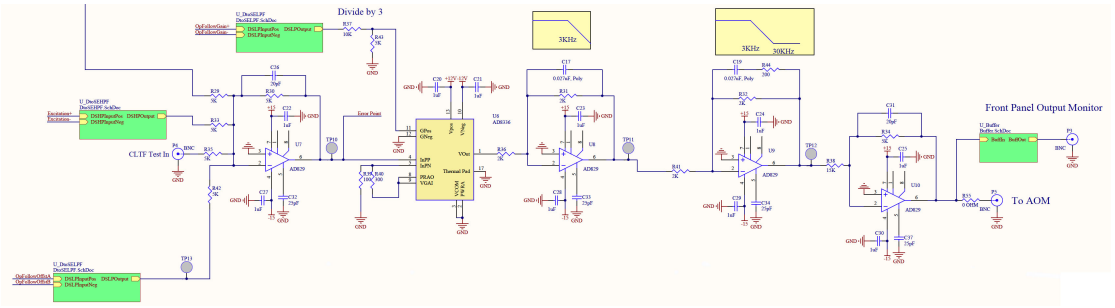

FIGURE 6.10: Amplifier and filters in OFS circuit

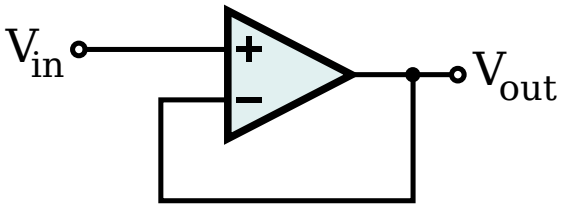

FIGURE 6.11: Voltage follower

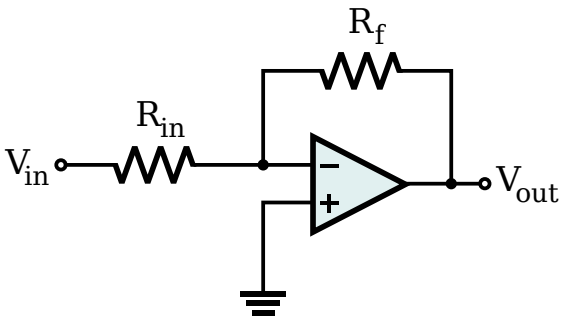

FIGURE 6.12: Inverting amplifier

A variable gain amplifier and a set of filters are used after inverting amplifier. We use AD8336 amplifier, which is a low noise, single-ended, linear in dB variable gain amplifier. The VGA gain is depend on the preamplifier. Fig. 6.13 shows the circuit of preamplifier. The gain of preamplifier is given as

$$G_{PRA} = 1 + \frac{R_{FB2}}{R_{FB1}} \tag{6.5}$$

and the composite gain of VGA is

$$Composite\ Gain[\text{dB}] = G_{PRA} + [V_{\text{GAIN}}\ (\text{V}) \times 49.9\ \text{dB/V}] + 4.4\ \text{dB}. \tag{6.6}$$

where the V_{GAIN} is the input voltage to the gain of VGA. We divided the gain voltage by 3 in our circuit. In our circuit $R_{FB1} = 100\Omega$, $R_{FB2} = 300\Omega$, so the preamplifier gain

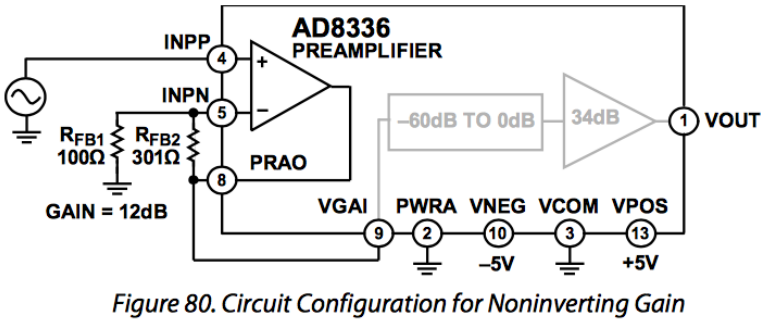

FIGURE 6.13: Preamplifier

is 12 dB. Then the composite gain can be written as

$$Composite\ Gain[\text{dB}] = [V_{\text{GAIN}}\ (\text{V})/3 \times 49.9\ \text{dB/V}] + 16.4\ \text{dB}. \tag{6.7}$$

After signal pass the VGA, it follows by a set of low pass filters. The general form of the low pass filters can be shown as in Fig. 6.14. The transfer function of the low pass

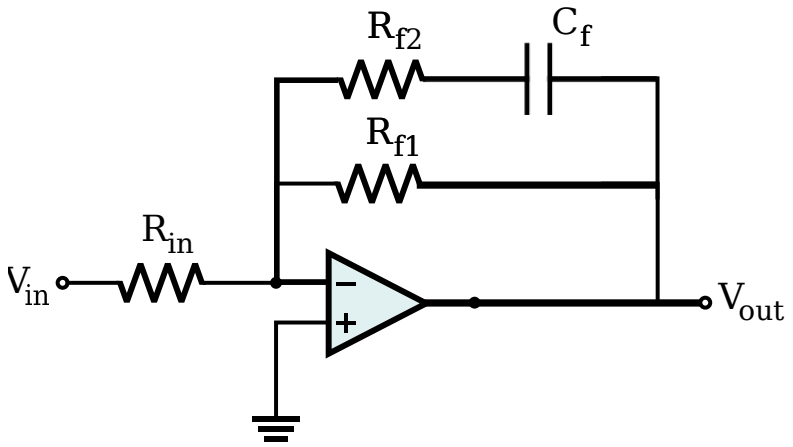

FIGURE 6.14: Op-Amp Low pass filter

filter can be written by

$$\frac{V_{out}}{V_{in}} = -\frac{R_{\rm f}}{R_{\rm in}}\left(\frac{1+j\omega C_{\rm f}R_{\rm f2}}{1+j\omega C_{\rm f}(R_{\rm f1}+R_{\rm f2})}\right) \tag{6.8}$$

, where the gain is $-R_{\rm f}/R_{\rm in}$, and a pole is at $f = 1/2\pi C_{\rm f}(R_{\rm f1}+R_{\rm f2})$ and a zero is at $f = 1/2\pi C_{\rm f}R_{\rm f2}$. There are 4 low pass filters in our circuit, and we listed the information of each filters in Table. 6.1.

$R_{\rm in}$	$R_{\rm f1}$	$R_{\rm f2}$	$C_{\rm f}$	gain	poles	zeros
5kΩ	5kΩ	0Ω	20pF	1	1.59 MHz	
2kΩ	2kΩ	0Ω	0.027μF	1	2.947 kHz	
2kΩ	2kΩ	200Ω	0.027μF	1	2.679 kHz	29.473 kHz
15kΩ	5kΩ	0Ω	20pF	1/3	1.59 MHz	

TABLE 6.1: OFS low pass filters

From Table. 6.1, we can see there are 2 poles around 3 kHz, and 1 zero at 30 kHz, and we can use the equation of VGA and filters to calculate the amplitude and phase of the open-loop transfer function. When the gain level is set at -0.9 V. The DC gain of total transfer function is

$$G = -0.9/3 \times 49.9 + 16.4 + 20\log_{10}\frac{1}{3} = -8.11\ [dB] \tag{6.9}$$

and the phase is

$$P = Arg\left[\left(\frac{1}{1+j\omega\times 20\times 10^{-12}\times 5\times 10^{3}}\right)\left(\frac{1}{1+j\omega\times 27\times 10^{-9}\times 2\times 10^{3}}\right)\left(\frac{1+j\omega\times 27\times 10^{-9}\times 200}{1+j\omega\times 27\times 10^{-9}\times 2.2\times 10^{3}}\right)\left(\frac{1}{1+j\omega\times 20\times 10^{-12}\times 5\times 10^{3}}\right)\right] \tag{6.10}$$

We can calculate that phase at 3 kHz is -88.14° and at 30 kHz is -125.93°. In the practical circuit, we use DAC to provide gain and offset DC voltage to OFS. In order to prevent the high frequency noise from DAC contaminates the gain and offset DC voltage, low-pass filters, whose pole is at 800 mHz, were placed after the input port of gain and offset. However, in the excitation channel, since we need to inject modulated signal, the low-pass filter cannot be placed after excitation channel. Therefore, we might see the high frequency noise from digital system at excitation channel.

We will check these value by measure the transfer function from PD input to four output port: PD monitor, Err monitor, To AOM connector, Output monitor.

PD tests	**KEK**		**KAGRA**	
	OFS1	OFS2	OFS1	OFS2
PD monitor amplitude	0 dB Flat	0 dB Flat	0 dB Flat	0 dB Flat
Err monitor amplitude	0 dB Flat	0 dB Flat	0 dB Flat	0 dB Flat
To AOM DC amplitude	-8.15 dB	-8.02 dB	-8.12 dB	-8.03 dB
To AOM phase at 3kHz	-86.79°	-87.58°	-88.30°	-87.69°
To AOM phase at 30kHz	-125.54°	-123.66°	-125.20°	-124.78°
Output monitor DC amplitude	-8.15 dB	-8.00 dB	-8.10 dB	-8.03 dB
Output monitor phase at 3kHz	-86.79°	-87.59°	-88.29°	-87.69°
Output monitor phase at 30kHz	-124.95°	-123.24°	-125.22°	-125.02°

(b) **Excitation Signal test:**

The excitation port is use to send the modulated signal into AOM. It combines with PD signal using the inverting amplifier shown in Fig. 6.12. Therefore, the transfer function from PD signal to OFS output is same as from excitation port to OFS output. We test the result by measuring the transfer function from excitation port to To AOM connector.

Excitation tests	**KEK**		**KAGRA**	
	OFS1	OFS2	OFS1	OFS2
DAC input DC amplitude	-8.16 dB	-8.11 dB	-8.12 dB	-8.06 dB
DAC input phase at 3 kHz	-86.83°	-87.60°	-88.25°	-87.81°
DAC input phase at 30 kHz	-125.20°	-125.65°	-126.73°	-124.95°
CLTF input DC amplitude	-8.16 dB	-8.11 dB	-8.16 dB	-8.06 dB
CLTF input phase at 3 kHz	-87.15°	-87.19°	-88.37°	-87.81°
CLTF input phase at 30 kHz	-126.78°	-125.88°	-124.66°	-125.14°

(c) **Gain tests:**

This section tests the gain of variable gain amplifier AD8336. From Eq. 6.7, by changing gain value from -1.8 V to 1.8 V, we can change the gain from -14 dB to 46 dB. Consider the amplitude decrease to one third in the following low-pass filter, and the input of PD is differential input which gain is 2, the total visibal gain can be changed from -17 dB to 42 dB. We test the result by changing the gain value of variable gain amplifier.

Gain voltage	**KEK**		**KAGRA**	
	OFS1	OFS2	OFS1	OFS2
-1.8 V	-16.19 dB	-16.65 dB	-16.36 dB	-16.59 dB
0 V	12.31 dB	12.23 dB	12.29 dB	12.38 dB
+1.8 V	41.63 dB	41.41 dB	41.58 dB	41.58 dB

(d) **Offset Input Test:**

Offset is use for sending DC level to "To AOM" connector in order to control AOM. In this section we test the offset performance by changing offset value. We set the gain voltage to -0.1875 V, and measure the DC value of "To AOM". The ratio between output and input should be 1.5.

Input voltage	**KEK**		**KAGRA**	
	OFS1	OFS2	OFS1	OFS2
0 V	-7.2 mV	-10 mV	-1.44 mV	40.1 mV
1 V	1.50 V	1.51 V	1.46 V	1.55 V
2 V	2.98 V	3.00 V	2.88 V	3.00 V

6.4 Circuit of Interface chassis

Interface board consist of front board and back board. Front board contains a set of differential to single converter, single to differential converter, and a relay. Differential to single converters converts the differential PD signal to single signal for the BNC connector, and single to differential converter convert the single ended temperature signal to differential signal in order to meet the input requirement of digital system. The relay is used for controlling the beam shutter. Back board contains a set of regulator to generate the suitable voltage for operation amplifier and relay, same as optical follower servo back board. The pictures of interface boards are shown in Fig. 6.15 and Fig. 6.16. The circuit of OFS front board and back board is shown in the following pages.

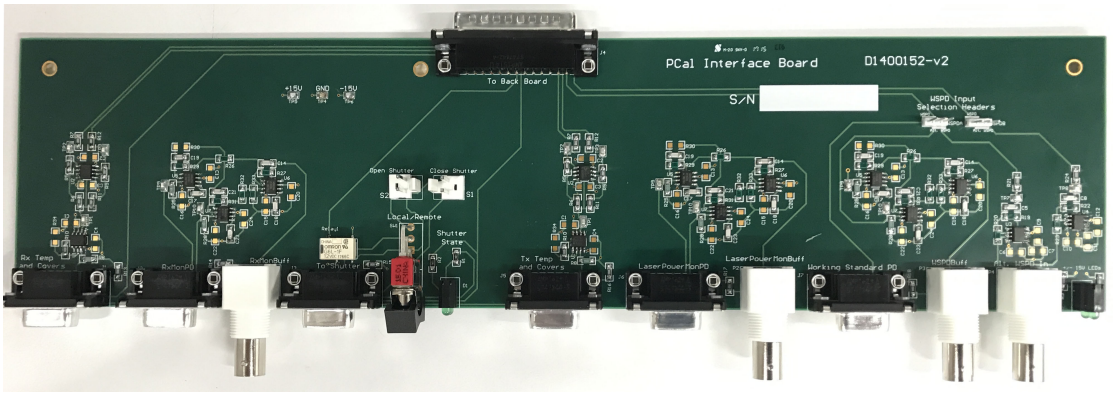

FIGURE 6.15: Interface chassis front board

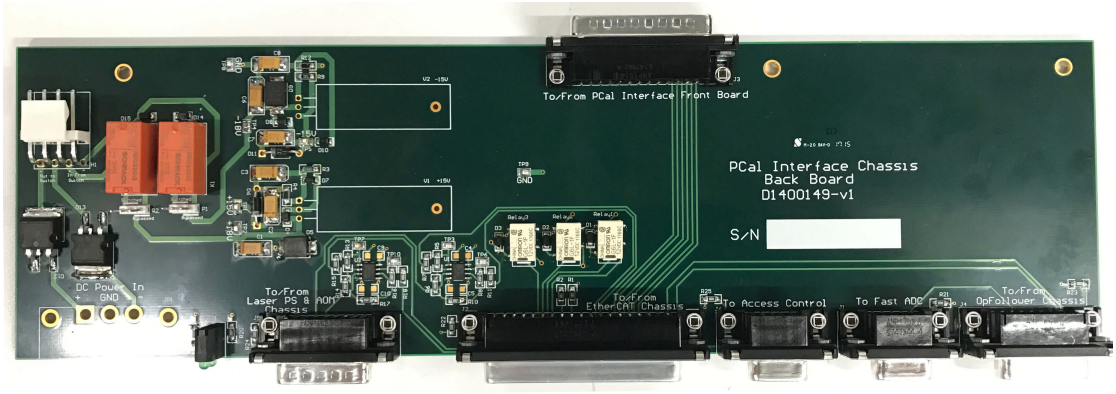

FIGURE 6.16: Interface chassis back board

6.5 Tests of Interface chassis

For the test of Interface chassis, we also followed the test procedure from LIGO Pcal Interface Chassis Test Procedure[48], and we change some expected results which matches

our modification of the circuit.

1. **Electrical Tests**

(a) We also provide ± 18 V for the interface chassis power supply. The relay in interface chassis do not need ± 12 V, so we only need to generate ± 15 V for the operational amplifiers. We use the LM317 and LM337 to generate ± 15 V, which is the same method as used in OFS back board. We turned on the power supply and check the LED status at the front panel. The picture of LED in interface board is shown in Fig. 6.17.

FIGURE 6.17: Power supply LED in Interface board

LED label	**KEK**		**KAGRA**	
	IF1	IF2	IF1	IF2
±15V	on	on	on	on

(b) Continuity Checks: Interface module sends the detector value and OFS value to the digital system. To check whether interface chassis is working normally, we need to check whether the original designed shorted pins are really shorted or not.

i. **OFS** & **PD Continuity tests:**

Connector	**KEK**		**KAGRA**	
	IF1	IF2	IF1	IF2
OFS gain	connected	connected	connected	connected
OFS offset	connected	connected	connected	connected
OFS Osc monitor	connected	connected	connected	connected
Loop switch	connected	connected	connected	connected
OFSPD readout	connected	connected	connected	connected
TxPD readout	connected	connected	connected	connected
RxPD readout	connected	connected	connected	connected
Error monitor	connected	connected	connected	connected

ii. **Interlock Continuity tests:**

There is also a interlock control system in interface module. We connect the Tx and Rx "Temp and Interlock" connectors to the interlocks in Tx and Rx module. If all of the interlock are shorted, the interface module will short the interlock of the laser and enable the laser. If we break one of the interlock, the interlock of laser will open and unable the laser. First, we short both Tx and Rx interlock, check the laser interlock status. Then we remove one of the interlock and check the laser interlock status again.

Laser interlock test	**KEK**		**KAGRA**	
	IF1	IF2	IF1	IF2
Short Tx and Rx interlock	connected	connected	connected	connected
Remove one interlock	not-connected	not-connected	not-connected	not-connected

iii. **WSPD Continuity tests:**

This section test if interface module can send the signal from working standard to the digital system.

Connectorc	**KEK**		**KAGRA**	
	IF1	IF2	IF1	IF2
WSPD readout	connected	connected	connected	connected

(c) **Relay Functions and OFS loop control tests:**

Interface module uses relay to control beam shutters. It has remote and local two modes. By connecting or terminating shutter power in the interface module, we can control the shutter remotely. Turn the switch in front of interface module from remote mode to local mode, we can control the beam shutter by the buttons on the interface chassis.

Connector	**KEK**		**KAGRA**	
	IF1	IF2	IF1	IF2
Shutter open readout	15V	15V	15V	15V
Shutter closed readout	15V	15V	15V	15V
Loop closed readout	15V	15V	15V	15V
Remote control power supply	15V	15V	15V	15V
Remote control shutter controller	15V	15V	15V	15V
Local control power supply	15V	15V	15V	15V
Local control shutter controller	0V	0V	0V	0V
Local control shutter controller (push open button)	15V	15V	15V	15V
Local control power supply (push closed button)	0V	0V	0V	0V

(d) **Photodiode input tests:**

i. **Signal Tests:**

In this test, we want to check if the interface module can successfully transfer the modulated signal from TxPD, RxPD and working standard into digital system without any deformation. The transfer function is expected to be unity.

Connector	**KEK**		**KAGRA**	
	IF1	IF2	IF1	IF2
TxPD to DGS	0dB Flat	0dB Flat	0dB Flat	0dB Flat
TxPD monitor readout	0dB Flat	0dB Flat	0dB Flat	0dB Flat
RxPD to DGS	0dB Flat	0dB Flat	0dB Flat	0dB Flat
RxPD monitor readout	0dB Flat	0dB Flat	0dB Flat	0dB Flat
WSPD to DGS	0dB Flat	0dB Flat	0dB Flat	0dB Flat
WSPD monitor readout	0dB Flat	0dB Flat	0dB Flat	0dB Flat

ii. **Alternate WSPD Input Test:**

Interface module provides an additional input for the working standard. Changing the jumpers from "WSPD" position, to the Alt. WSPD position, we can send the working standard value from the "Alt. WSPD" BNC. Since "Alt. WSPD" BNC is not differential input signal, the amplitude output signal from interface module is double of input signal, i.e., 6 dB gain.

Connector	**KEK**		**KAGRA**	
	IF1	IF2	IF1	IF2
WSPD DGS readout	5.96 dB Flat	5.96 dB Flat	5.98 dB Flat	5.98 dB Flat
Alt.WSPD BNC readout	6.02 dB Flat	6.02 dB Flat	6.02 dB Flat	6.02 dB Flat

iii. **Power to PD tests:**

This test check if interface module provides the correct DC power for the TxPD, RxPD, and WSPD. The Op-amp in the PD circuit requires ±15V to work normally.

Connector	**KEK**		**KAGRA**	
	IF1	IF2	IF1	IF2
TxPD +15V	14.80 V	14.78 V	14.81 V	14.79 V
TxPD -15V	-15.00 V	-15.02 V	-15.00 V	-15.02 V
RxPD +15V	14.80 V	14.78 V	14.81 V	14.79 V
RxPD -15V	-15.01 V	-15.02 V	-15.00 V	-15.02 V
WSPD +15V	14.80 V	14.78 V	14.81 V	14.79 V
WSPD -15V	-15.00 V	-15.02 V	-15.00 V	-15.02 V

(e) **Temperature Sensor tests:**

We install the temperature sensor inside Tx and Rx module to monitor their temperature. In this test we check the if the interface module correctly transfer the temperature

readout to the digital system. We test it with sending 1 mA current to the input of temperature monitor input of Tx and Rx. Since transimpedence resistance is 10 kΩ, and the circuit has differential output, we will read 20 V at the output to digital system.

Connector	**KEK**		**KAGRA**	
	IF1	IF2	IF1	IF2
Tx	20.00 V	20.00 V	20.01 V	20.00 V
Rx	20.00 V	20.00 V	20.01 V	20.00 V

6.6 Summary

We imported Optical Follower Servo system from LIGO and made two Optical Follower Servo board and two Interface boards in order to control two Acousto-Optic Modulators. Optical Follower Servo is an active controller which is able to control and correct the noise in the Pcal beams. Interface chassis plays a role of communicating between digital system and Photon Calibrator. We performed Optical Follower Servo Chassis test procedure and Interface Chassis test procedure in KEK lab and in KAGRA site. Both of the OFS chassis and Interface chassis pass the test procedure in KEK lab and in KAGRA site, and we can successfully use them for the integration test.

Chapter 7

Integration test

7.1 Purpose of Integration test

Practically in Pcal operation, we use OFS chassis to control the AOM, use Interface chassis to send the power to the beam shutter from digital system, and send the value from photodetectors and the temperature sensors to the digital system. Therefore, the integration test, which combine the Pcal, OFS, and digital system together is important. We use the Motif Editor and Display Manager (MEDM) (Fig. 7.1) to control the Photon Calibrator remotely.

From the MEDM screen, we can set the current of the laser, read the power and the current from the laser module. We can control the beam shutters switch, OFS loop switch, gain and offset of the OFS. Once the laser is turned on and OFS parameter is set, we can read the OFSPD value, TxPD value, and RxPD value from the screen. We can also send the excitation signals from digital system when measuring transfer function or sending calibration lines. The temperature of the laser, Tx module and Rx module are also shown on the MEDM screen.

7.2 Power map

7.2.1 Overview

In the Photon Calibrator system, two laser beams are sent from Tx module to the periscope in EYA chamber. After passing four periscopes in the EYA chamber, two laser beams pass through 36 meter tube and injected to the end test mass. After reflected from end test mass, two laser beam pass though 36 meter tube again, sending to the

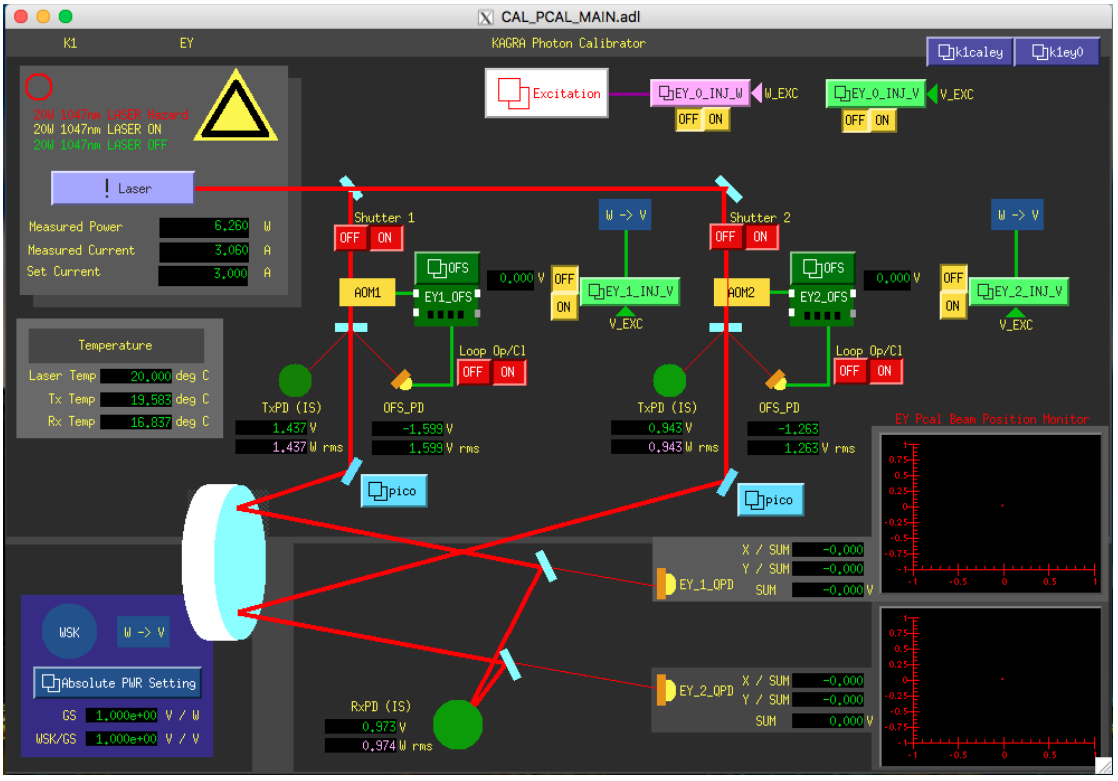

FIGURE 7.1: MEDM for Photon Calibrator

EYA chamber, passing four periscopes and finally go to Rx module. We measured the power of two laser beams ar the output of Tx module and in Rx module, and we found that there is some power losses in the light path. The loss of the laser power corresponds to the efficiency of modulating ETM, and the uncertainty of the power loss corresponds to the systematic error of Pcal. We want to know which part of the laser path causes power losses.

7.2.2 Setup

Fig. 7.2 shows the instrument setup around EYA chamber and the exact measurement positions. We measure the laser power at 5 positions. (1) Tx module, (2) EYA chamber (Tx side), (3) EYC chamber (ETM) (is not shown in Fig. 7.2), (4) EYA chamber (Rx side), (5) Rx module.

7.2.3 Result

The measurement result is shown in Table. 7.1. From the result, we can see that the laser power start has some losses when they are emitted to the EYC chamber. We

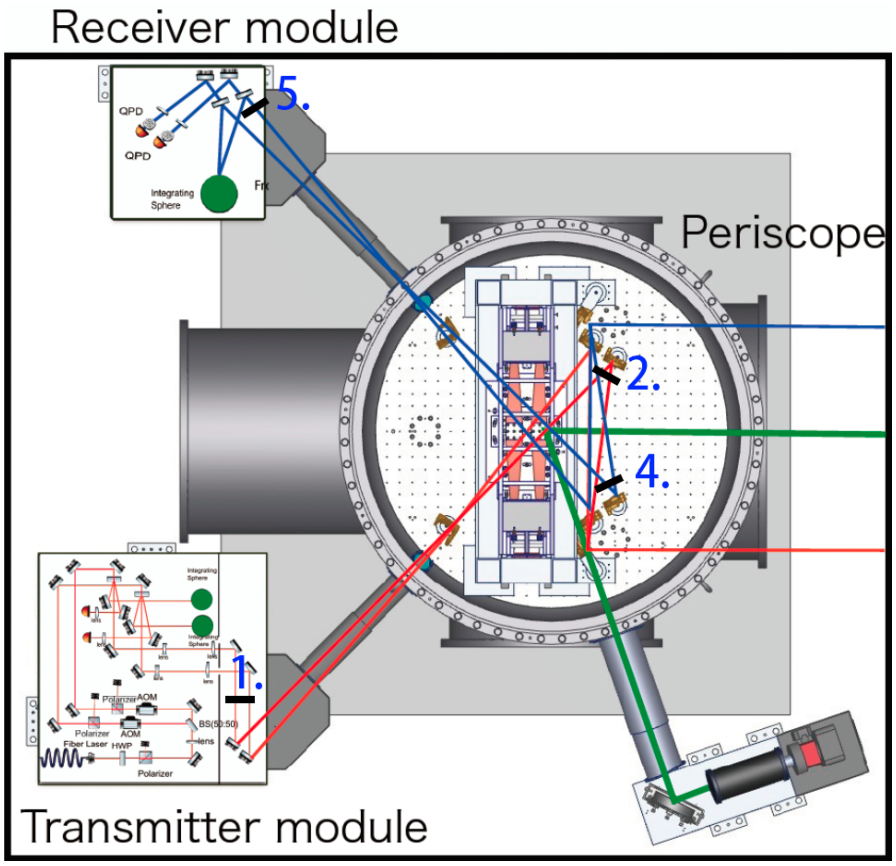

FIGURE 7.2: EYA chamber

	Path1	Path2
Tx	0%	0%
EYA (Tx side)	0%	0%
EYC	2.1%	3.1%
EYA (Rx side)	7.2%	11.9%
Rx	7.7%	12.4%

TABLE 7.1: Power losses map

checked the beam shape of at each position. Fig. 7.3 shows the beam shape using laser sensor card.

We can see that in Tx module and the EYA(Tx side), the beam shape are still circular shape. However, in EYC chamber, we can see there are Airy disk pattern in front of end test mass. At EYA(Rx side) and Rx module, the Airy disk pattern become larger. The aperture of out power meter (Fig. 4.14) is 28 mm, and the side of squared sensor card is 52 mm. From Fig. 7.3(g), Fig. 7.3(h), Fig. 7.3(i), Fig. 7.3(j), we can estimate that the Airy disk pattern diameter is around 33 mm, larger than the aperture of power meter. Therefore, we think that the main reason of the loss of the Photon Calibrator is

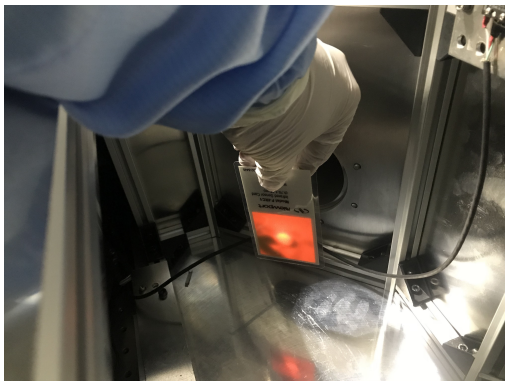

(a) Tx path1

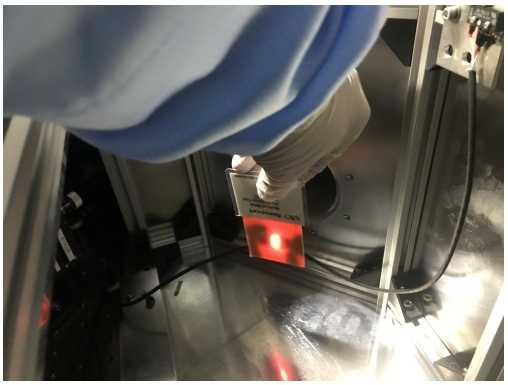

(b) Tx path2

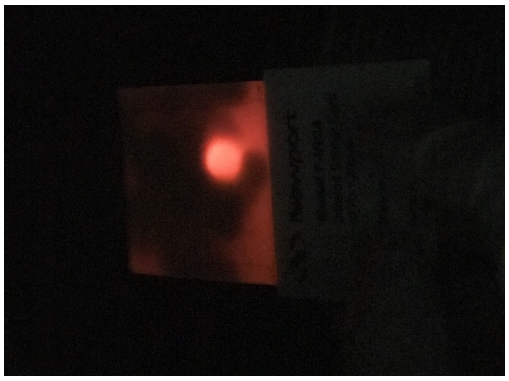

(c) EYA(Tx side) path1

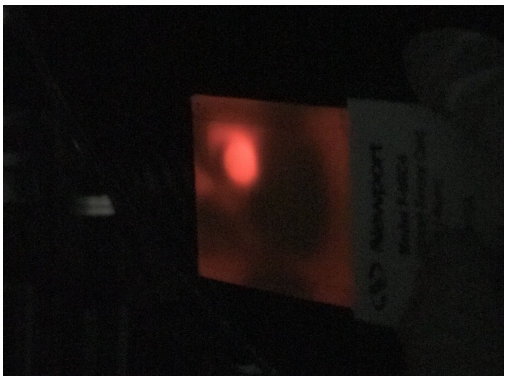

(d) EYA(Tx side) path2

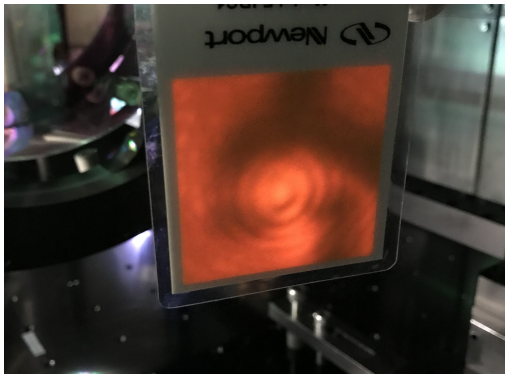

(e) EYC

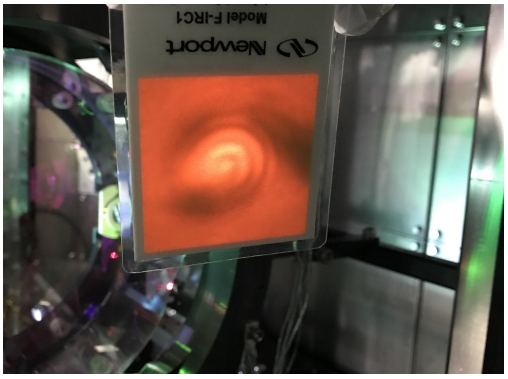

(f) EYC

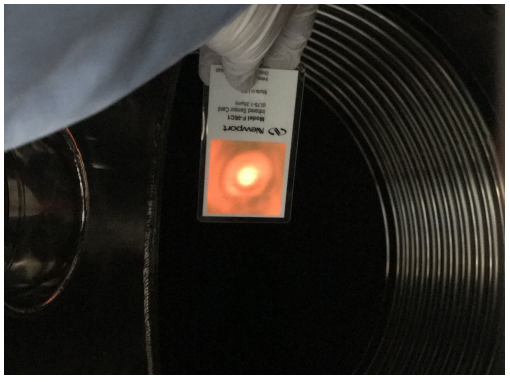

(g) EYA(Rx side) path1

(h) EYA(Rx side) path2

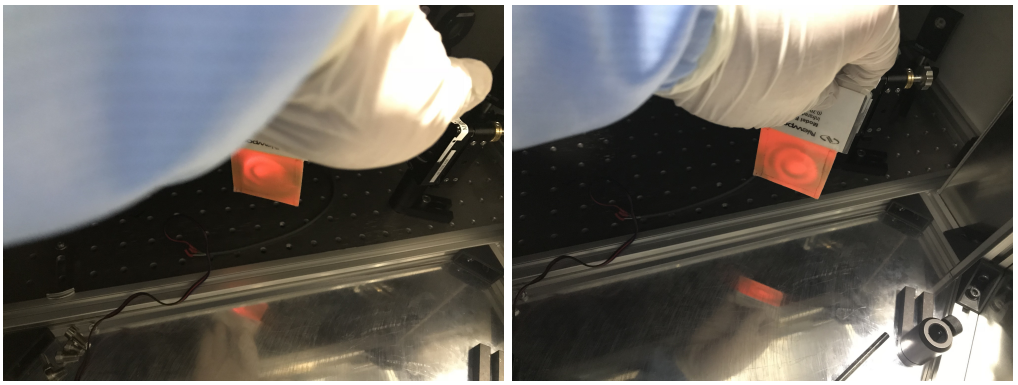

(i) Rx path1 (j) Rx path2

FIGURE 7.3: Beam shape

because the aperture size of the power meter cannot detected all of the laser beam due to the large Airy disk pattern.

The Airy disk is due to the optical aberration of the two modematching lenses in Tx module. The 5 monochromatic aberrations are spherical aberration, coma, defocus, astigmatism, and image distortion. The main aberration of our Airy disk is due to spherical aberration. The reason why spherical aberration happens is because the laser beam at the center and near edge of the lens cannot be focused to one point (Fig. 7.4). The beam shape of spherical aberration is shown as Fig. 7.5, which can also be seen in our beam shape.

7.3 AOM Efficiency

7.3.1 Overview

An acousto-optic modulator (AOM) use the acousto-optic effect to diffract the laser beam using sound wave at radio frequency (RF). The efficiency of AOM is related to the optical efficiency of Pcal laser power. When RF is not sent to AOM, the laser beam directly pass the AOM (0th beam). When a RF signal is sent to AOM, a sound wave in the crystal is created which generate a periodic change in index of refraction of the crystal and form a diffraction grating. When a laser beam injected into the diffraction grating, the laser beam is diffracted (1st beam). This phenomenon is called acousto-optic effect. The schematic figure of operating principle is shown in Fig. 7.6)[50].

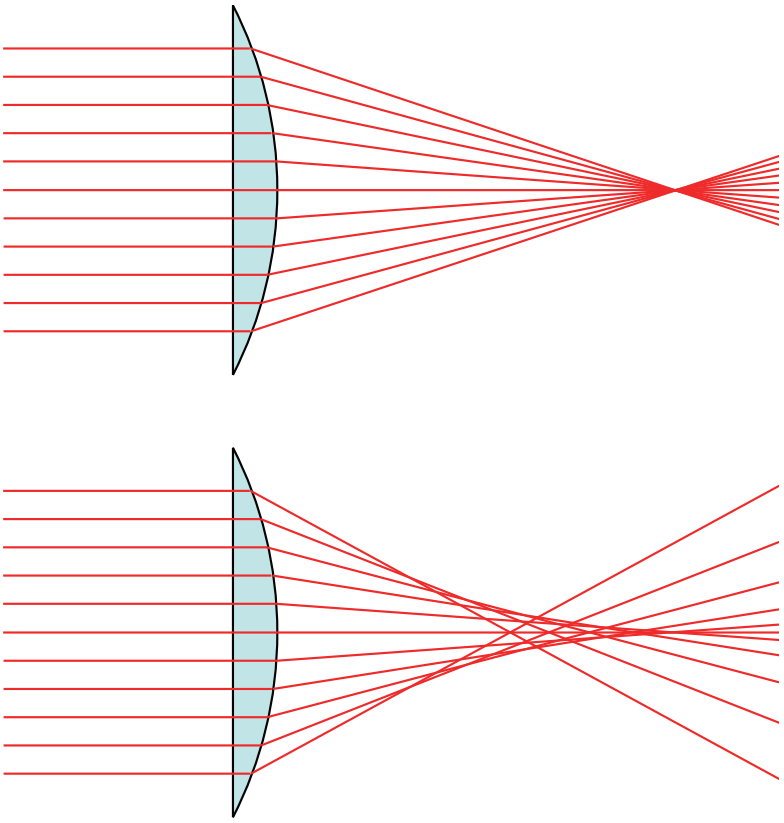

FIGURE 7.4: Spherical aberration [49]

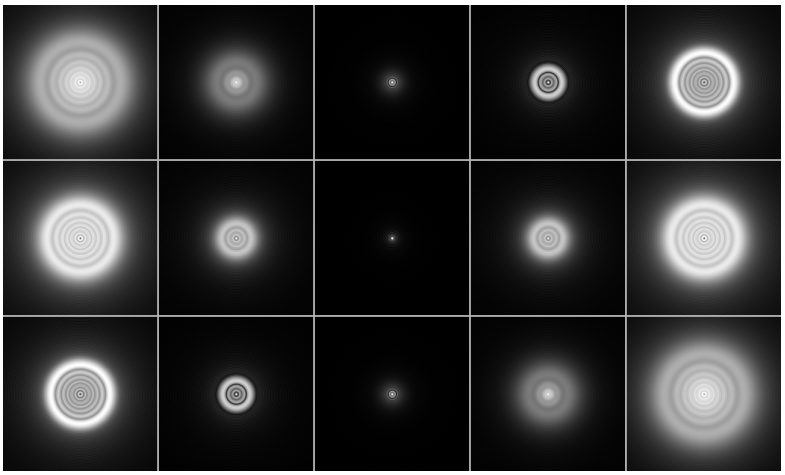

FIGURE 7.5: Spherical aberration disk [49]

The diffraction efficiency (DE) of AOM is defined as the ration of the output zeroth order beam (RF off) and the first order beam (RF on).

$$DE = \frac{I_{1st}}{I_{0th}} \tag{7.1}$$

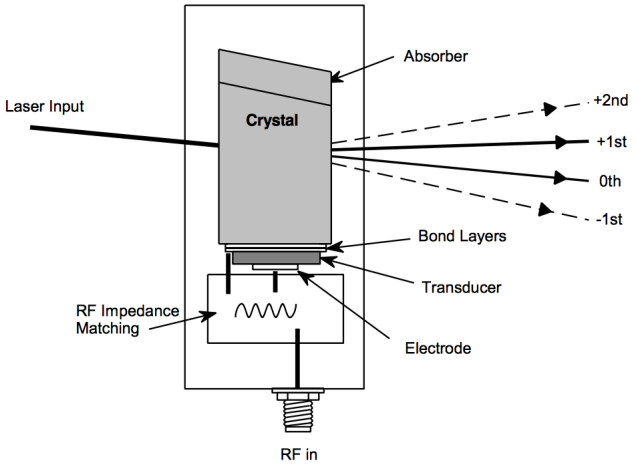

FIGURE 7.6: Operating principle of AOM

, and insertion losses (IL) caused by the absorption in the bulk material and the losses at the AR coated surface is define as

$$IL = 1 - \frac{I_{0th}}{I_{laser}} \tag{7.2}$$

Therefore, the total transmittance of the AOM can be written as

$$\text{Total transmittance} = DE \times (1 - IL)\% \tag{7.3}$$

To understand the transmittance of AOM, I measure the relationship between the voltage given to AOM and the 1st order beam power. The AOM efficiency can be described as

$$\epsilon = P_{max} \sin^2(\frac{2\pi}{4V_{max}} V) \tag{7.4}$$

, where the P_{max} is the maximum AOM efficiency and the V_{max} is the corresponding voltage. In this section we measure the insertion losses and diffraction efficiency of the AOM.

7.3.2 Setup

We send 0.5 V to the AOM driver, and we adjust the angle of the AOM to see the diffracted beam after AOM. We can distinguish zeroth order beam and first order beam by turn off the AOM power supply, then we block zeroth order beam and use power meter to measure the power of first order beam. We adjust AOM position and the incident angle of the laser beam to maximize the first order beam.

After we fixed the alignment of AOM, we can start measuring insertion losses and diffraction efficiency. First we turn off the RF signal of AOM, and put a power meter in front of AOM to measure the input laser power, then we put the power meter after AOM to measure zeroth order laser power in RF off situation. Using Eq. 7.2 we can calculate the insertion losses. Next, we turn on the RF signal and send 0.5 V to the AOM, we can see the zeroth order beam and the first order beam exist (second order beam may also exists). Block all the beams except for the first order beam, and use power meter measure the first order beam. Use Eq. 7.1 to calculate the diffraction efficiency. The total transmittance is given by Eq. 7.3.

Note that the beam width near AOM is the beam waist point. If we put power meter at the focus point, the power meter might burn, so it is better to use mirror to change the beam direction and enlarge the distance measuring position. Beside, the laser power is not stable, so if we measure the power before AOM and after AOM in the different time, the calculated insertion losses are unreliable. However, when we measure the laser power before AOM, it is impossible to measure the laser power after AOM simultaneously. Therefore, it is better to minimize the measurement time to prevent the unstablized laser power affect the measured result.

7.3.3 Result

We measured the AOM efficiency in KEK and in KAGRA, the result is shown in the Table. 7.2.

		Insertion Losses	Diffraction Efficiency	Total transmittance
Path1	KEK	10.9%	91.9%	81.9%
	KAGRA	15.5%	92.6%	78.2%
Path2	KEK	2.5%	86.4%	84.1%
	KAGRA	3.1%	84.9%	82.3%

TABLE 7.2: AOM efficiency

From Table. 7.2, we found that the insertion losses of both path in KAGRA site is larger than in KEK lab test. We wondered that the dust contaminated the AOM crystal surface. We used IR viewer to check the AOM surface, and found there are scattering light on the both AOM surface. The pictures are shown in Fig. 7.7(a) and Fig. 7.7(b). Then we opened the AOM cover and check the scattering light on the AOM crystal again. Fig. 7.8(a) and Fig. 7.8(b) show two AOMs with cover opened, and Fig. 7.9(a) and Fig. 7.9(b) are the pictures under IR viewer. Fig. 7.10 is the removed AOM cover. We can see that there is scattering light on the crystal surface of both AOM, therefore,

we cleaned the AOM crystal surface and measure AOM efficiency again. The result is shown in table Fig. 7.3.

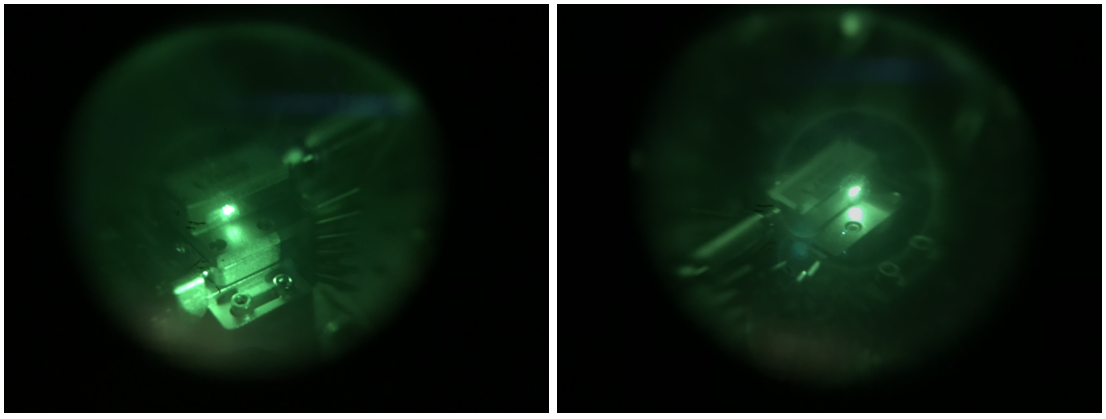

(a) AOM1 (b) AOM2

FIGURE 7.7: AOM viewed by IR viewer

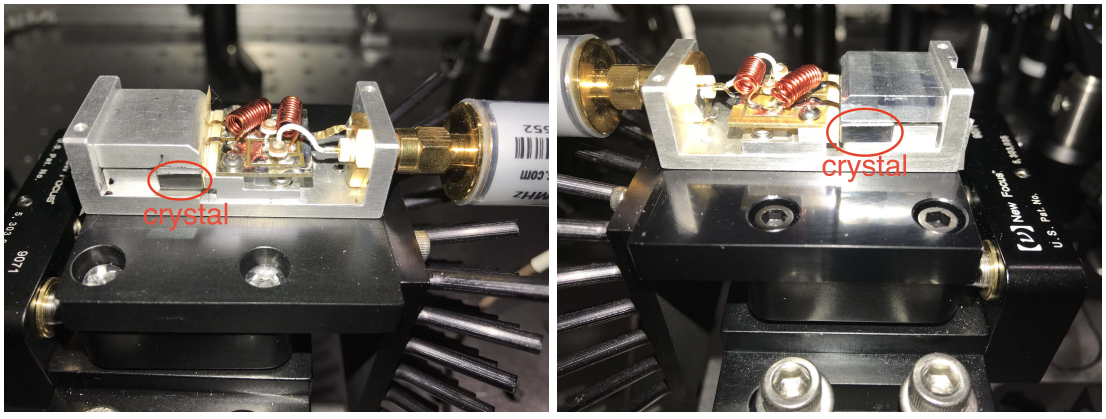

(a) AOM1 (b) AOM2

FIGURE 7.8: Cover opened AOM

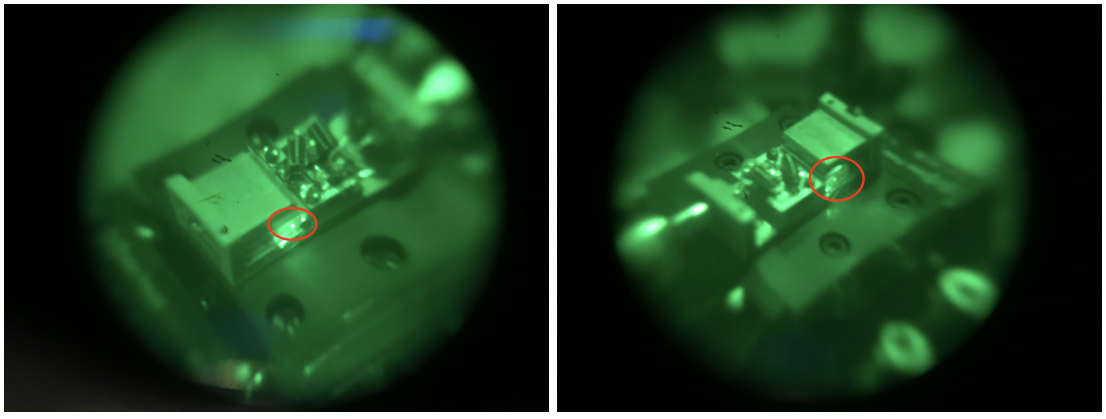

(a) AOM1 (b) AOM2

FIGURE 7.9: AOM viewed by IR viewer (cover opened)

FIGURE 7.10: AOM cover

		Insertion Losses	Diffraction Efficiency	Total transmittance
Path1	KEK	10.9%	91.9%	81.9%
	KAGRA	9.1%	93.5%	85.0%
Path2	KEK	2.5%	86.4%	84.1%
	KAGRA	2.6%	84.7%	82.5%

TABLE 7.3: AOM efficiency (after cleaning AOM surface)

After cleaning AOM surface, the insertion losses for path1 decreased from 15.5% to 9.1%, and for path2 it also decreased from 3.1% to 2.6%. The diffraction efficiency didn't change too much. We can conclude that the dust on the AOM crystal surface will increase the insertion losses. The rest of the insertion losses may due to the reflection of AOM surface and the absorption of TeO2 crystal.

7.4 Transfer function

To understand the performance of Photon Calibrator, we need to measure the transfer function. We send the modulated signal to OFS, and observe how much modulation amplitude we can get from photodetector. The ratio of photodetector signal over input signal is the transfer function. To fully understand the transfer function of Pcal, first we need to understand the transfer function of the digital system, which we use to measure the transfer function. When we measure the transfer function of Pcal, we need to remove the transfer function effect caused by digital system. Next, we need to measure the transfer function of AOM and each photodetector to understand the gain of each stage. Finally, we can measure the transfer function of Pcal and compare the measured result to the expected value.

7.4.1 Digital system and analog filters

To send signals to control Pcal and read the photodetector result from Pcal, we use digital system. Digital system generate analog signal from Digital-Analog Converter (DAC). The analog signal pass through a a anti-imaging (AI) filters to remove the imaging effect, then sent to Pcal. The analog signal from Pcal is sent to analog anti-aliasing (AA) filter, then sent to Analog-Digital Converter (ADC). The schematic of digtal system signal transfer is shown in Fig. 7.11. The anti-imaging and anti-aliasing filters are low-pass filters to remove the high frequency imaging and aliasing effect. The poles and zeros are shown in Table. 7.4 and Table. 7.5.

FIGURE 7.11: Digtal system

Type	Frequency [Hz]	Q-value
gain = 0.9993461		
pole	7681.5821	
pole	10486.359	49605.226
pole	856088.77	
zero	62978.311	67067911

TABLE 7.4: Analog anti-aliasing & anti-imaging filter

Type	Frequency [Hz]	Q-value
gain = 1		
pole	2895.34	1.1373
pole	5395.62	7.64573
zero	8192	666
zero	16384	555

TABLE 7.5: Digital anti-aliasing & anti-imaging filter

The transfer function of these 4 filters are shown in Fig. 7.12. When we use digital system to measure transfer function, we want to remove the transfer function of digital system to see the real transfer function of our measuring object. Therefore, we apply inverse analog AA, AI, and digital AA, AI filters in the original digital transfer function. The inverse AA, AI filters are shown in Table. 7.13. The transfer function of th digital system after applying inverse filters is shown in Fig. 7.14.

From Fig. 7.14, we can see by employ inverse AA, AI filters, the transfer function of digital system become flat in both amplitude and phase digram. However, at high

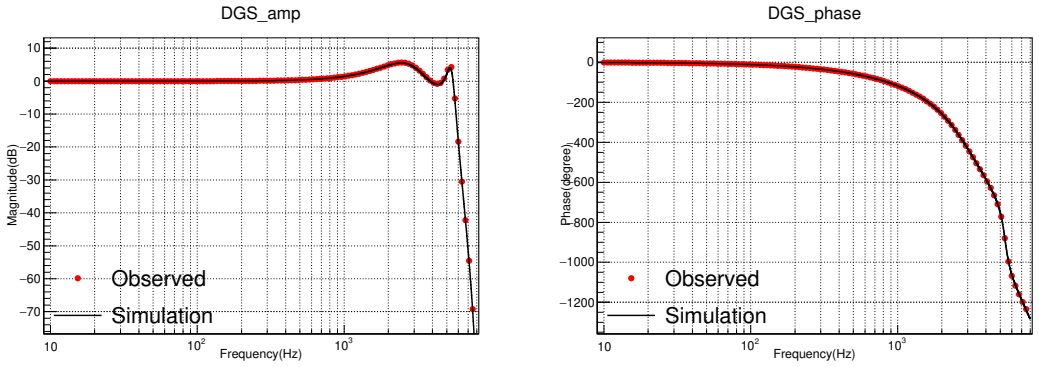

(a) Amplitude (b) Phase

FIGURE 7.12: Transfer function of digital system

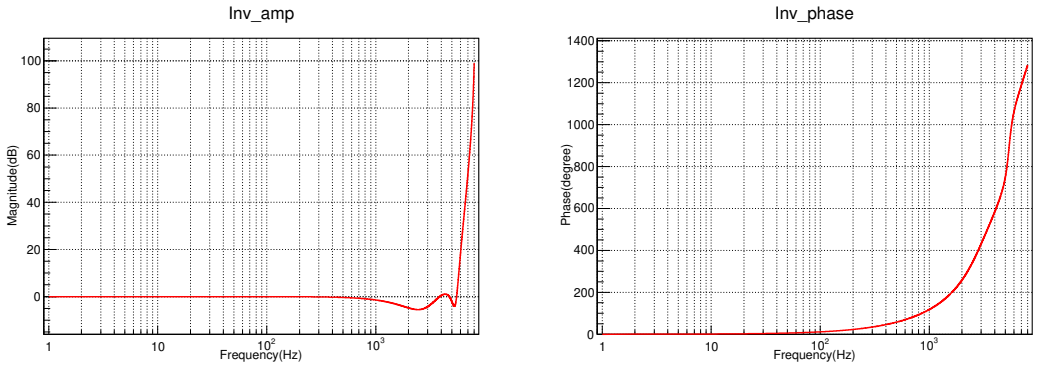

(a) Amplitude (b) Phase

FIGURE 7.13: Transfer function of inverse filters of digital system

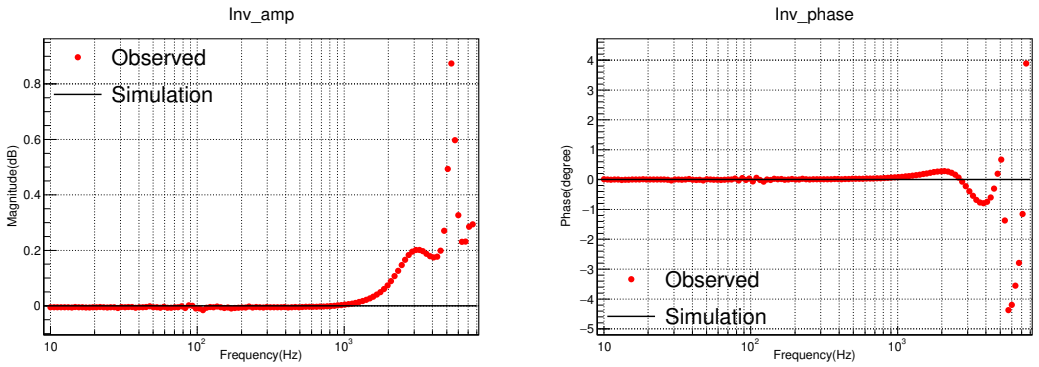

(a) Amplitude (b) Phase

FIGURE 7.14: Sum of digital system filters and inverse filters

frequency region we still cannot remove the AA, AI filter effect to make the transfer function flat. We think this reason is because the poles and zeros in the AA, AI filters may have some drift so they slightly change from the designed value. But at least we improved the transfer function below 1 kHz, and the deviation at high frequency region

is not too large. We will apply the inverse AA, AI filters in the Pcal transfer function measurements.

7.4.2 AOM transmittance and Transfer function of the photodetectors

7.4.2.1 Overview

Fig. 7.15 shows the open-loop control of Pcal. We use digital system to set the gain and offset for OFS, and use OFS to control the AOM. The AOM controls the laser power,and the laser power is read out by a photodetector. If we want to decrease the noise of the laser , we need to use closed-loop setup. Fig. 7.16 shows the closed-loop feedback control of Pcal. We negatively feedback the readout of photodetector to injected signal. If there is no injected signal, we simply use offset of OFS to control the photodetector readout. To understand the transfer function of the Pcal, we need to understand the AOM transmittance, and the transfer function of each detectors.

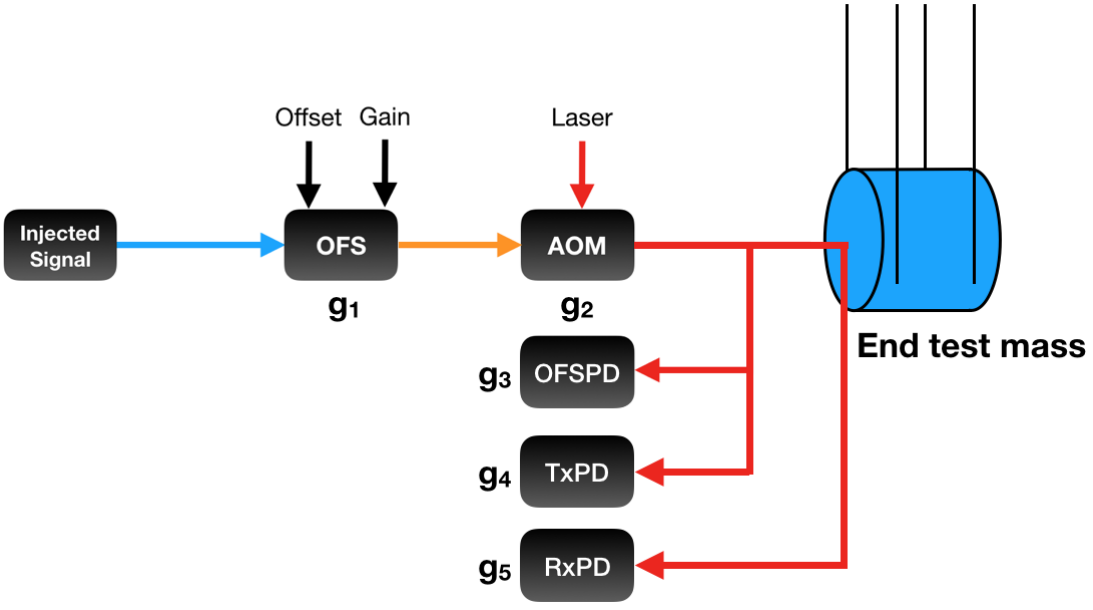

FIGURE 7.15: Open-loop feedback control

7.4.2.2 Setup

Set the loop control to be the closed-loop. Put a power meter on the output area of Tx module and make sure it receives total power of the laser. Turn on the laser to 20 watts, and increase the offset from 0 V with 0.2 V step. Record the "ToAOM" connector value, power meter value, OFSPD value, and TxPD value. Using "ToAOM" connector

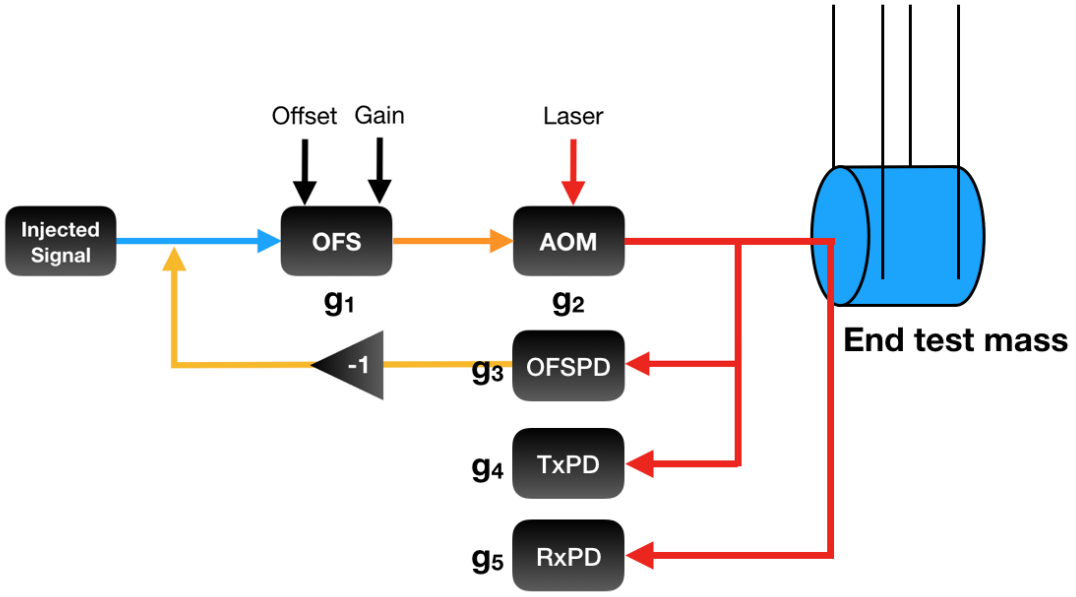

FIGURE 7.16: Closed-loop feedback control

value and power meter value we can make AOM transmittance plot, and using power meter value, OFSPD value, and TxPD value we can make the plots of transfer function of OFSPD and TxPD. Since we put the power meter at the output part of Tx module and blocked the beam which goes to the Rx module, we cannot read the RxPD value at the same time. Next, we remove the power meter from Tx module and do the same measurement again. Read OFSPD, TxPD and RxPD at the same time, we can measure the transfer function of RxPD.

7.4.2.3 Result

Fig. 7.17 is the result of AOM transmittance. We use linear function to fit the region around the working point in order to check the linear gain. We choose the region where input voltage to AOM is from 0.15 V to 0.3 V. Fig. 7.18(a), Fig. 7.18(b), and Fig. 7.18(c) show the transfer function of each photodetectors, and we use linear function to fit the data and calculate the gain of the detectors.

The AOM transmittance and the gain of each detector is listed in Table. 7.6.

	AOM transmittance [W/V]	OFS [V/W]	TxPD [V/W]	RxPD [V/W]
Path1	23.7	1.09	1.08	0.41
Path2	20.4	0.94	0.79	0.43

TABLE 7.6: AOM transmittance and transfer function of each detectors

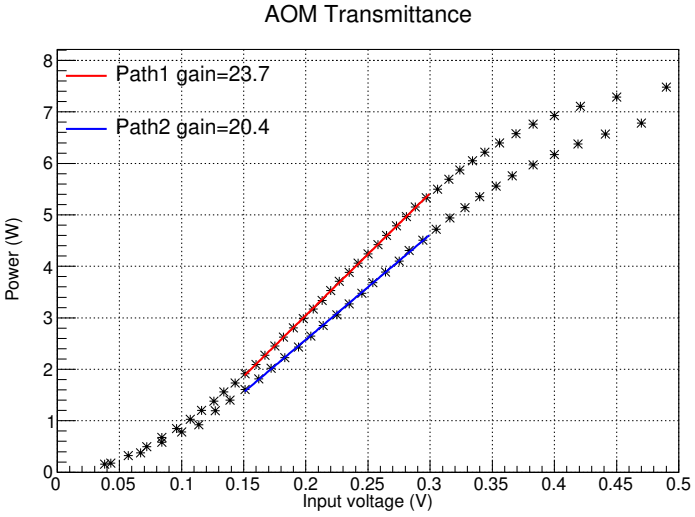

FIGURE 7.17: AOM transmittance. Red and blue lines show the result for path1 and path2. We use linear function to fit AOM transmittance in the range of input voltage of AOM between 0.15V to 0.3V

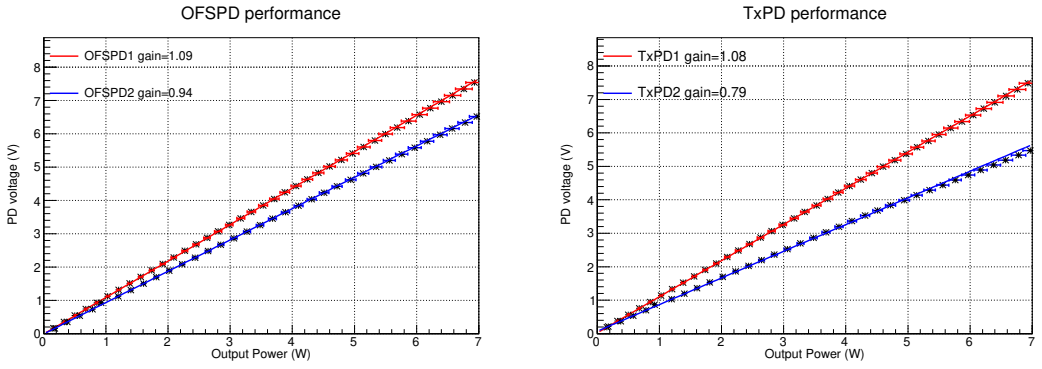

(a) OFSPD

(b) TxPD

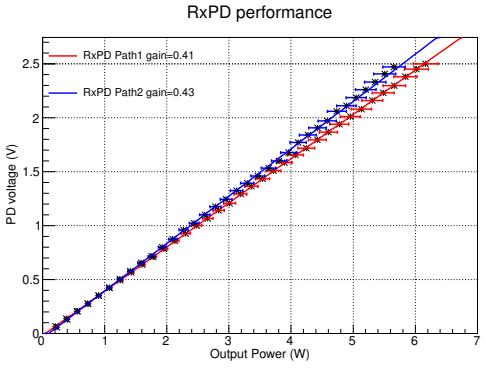

(c) RxPD

FIGURE 7.18: Transfer function of each detector. Red and blue lines show the result for path1 and path2. We calibrated the output power of Tx module to the readout value of photodetectors. The systematic error of our power meter calibration is 2.2% [51]

Using the gain of each detectors, we can calculate the gain of transfer function of Photon Calibrator in the following section.

7.4.3 Zigzags in the transfer function of Digital system

7.4.3.1 Overview

Before measuring transfer function of Pcal, first we want to understand the transfer function of digital system itself. According to Sec. 7.4.1, the transfer function of the digital system is flat but has some poles and zeros in the high frequency region. However, when I measure the transfer function, I found the zigzag shape in the low frequency region. Therefore, I investigated this problem by changing the parameters in diaggui, which is a software for measuring transfer function, noise spectrum and so on.

7.4.3.2 Setup

Connect DAC and ADC together, and use diaggui to measure the transfer function of the digital system. First we changed the average times from 10 times to 20 times, 30 times and compare the result. Next, we changed the measurement time. Measurement time can be set by cycles and seconds. To use cycles or seconds depends on the frequency. If the measurement time in cycle is larger than in seconds for the certain frequency it will use cycle as the measurement time, and vice versa. For instance, for a 100 Hz sine wave signal, 10 cycles equals 0.1 second. If we set the measurement time to be 10 cycles and 0.1 second, The frequency below 100 Hz will use 10 cycles as the measurement time, and the frequency above 100 Hz will use 0.1 second as the measurement time. We changed the measurement time from 10 cycles to 20 cycles, and changed the measurement time from 0.1 second to 0.2 second and compared the difference. To calculate the error of transfer function, I measured the coherence function of the transfer function simultaneously. The statistical error of the transfer function is defined in Eq. 7.5 and Eq. 7.6.

$$\frac{\mathrm{d}(|TF|)}{|TF|} = \sqrt{\frac{1-C}{2CN}} \tag{7.5}$$

$$\mathrm{d}\angle(TF) = \sqrt{\frac{1-C}{2CN}} \quad [rad] \tag{7.6}$$

where N is number of average times, and C is coherence function given by

$$C_{xy} = \frac{|G_{xy}(f)|^2}{G_{xx}(f)G_{yy}(f)} \tag{7.7}$$

where $G_{xy}(f)$ is the cross-spectral density between x and y, and $G_{xx}(f)$ and $G_{yy}(f)$ the power spectral density of x and y.

7.4.3.3 Result

First, we change the number of average times from 10 times to 20 and 30 times, measure the amplitude, phase and the coherence function The result is shown in Fig. 7.19 and Fig. 7.20.

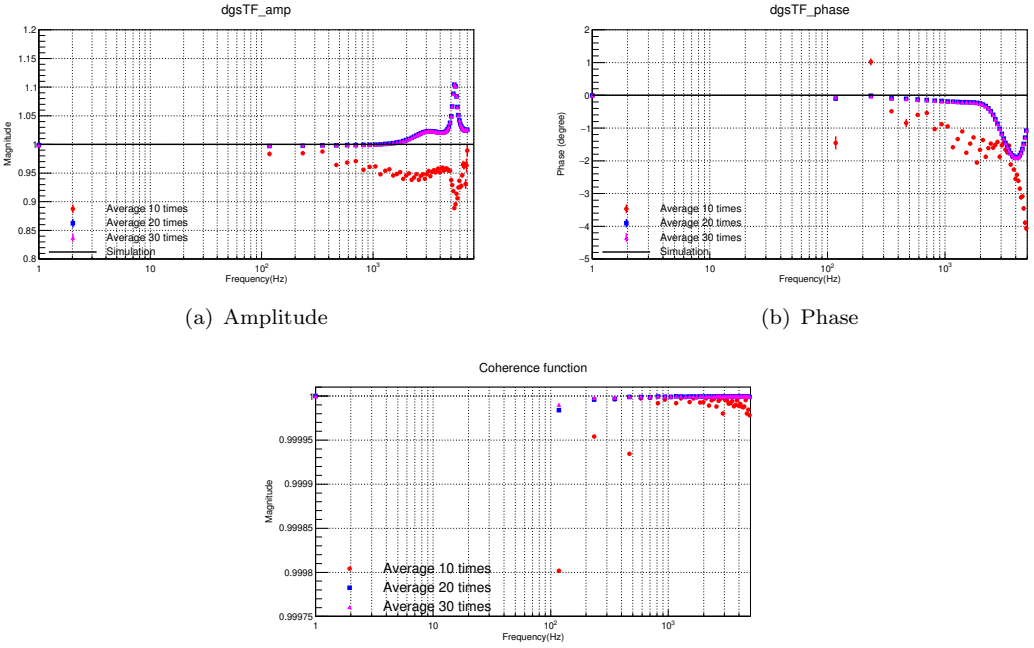

(a) Amplitude

(b) Phase

(c) Coherence

FIGURE 7.19: Transfer function of digital system (Change: average times) (Sweep type: linear)

From Fig. 7.19 and Fig. 7.20 we can see that the result of averaging 10 times has many zigzag shape in both amplitude figure and phase figure, but average 20 or 30 times has the smooth result no matter we use linear sweep type or log sweep type. We can also find there is large zigzags in the coherence function. We think that the coherence function is not large and stable enough so it cause the unstabilized transfer function. When the digital system calculates transfer function, it applies window function to pick up the peak of frequency. In the 10 average times measurement, it might apply the window function to the edge of data which is not the sinusoidal wave region. This would cause the appearance of zigzag shape in transfer function. We understand by increasing average times we are able to remove the zigzag shape.

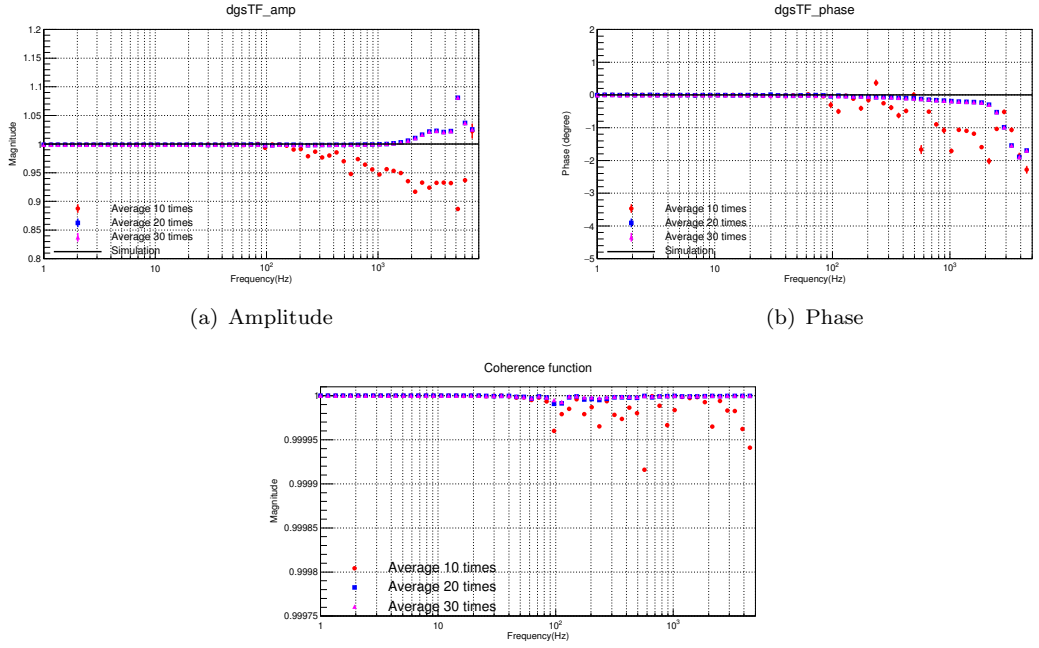

(a) Amplitude

(b) Phase

(c) Coherence

FIGURE 7.20: Transfer function of digital system (Change: average times) (Sweep type: log)

Next we investigate the error of digital system transfer function. We subtracted the transfer function of averaging 20 and 30 times, and compare it to the root-mean-square of statistical error calculated from coherence function. If the two values are identical, then there is no systematic error of digital system transfer function. The result is plot in Fig. 7.21. We then plot the subtraction of 20 and 30 times into a histogram. The result is shown in Fig. 7.22.

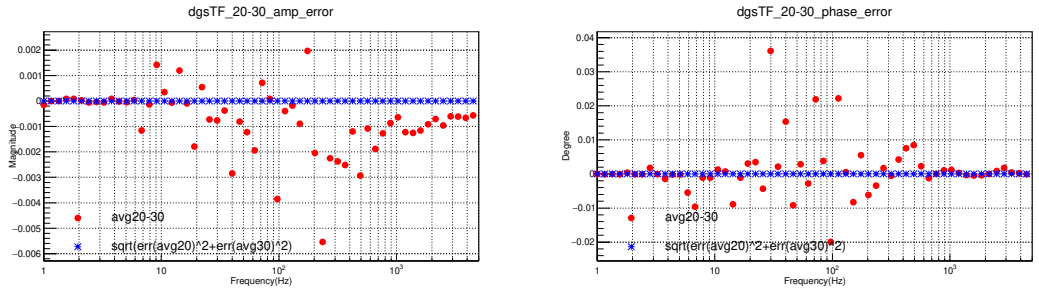

(a) Amplitude

(b) Phase

FIGURE 7.21: Error of TF in DGS. Red points show the subtraction of DGS value between 20 times and 30 times average. Blue points show the summation of error in 20 times and 30 times average measurement

From the result, we can understand that the systematic error of digital system start from around 6 Hz. These effect might be related to the edge effect of diaggui software, which should be investigate further.

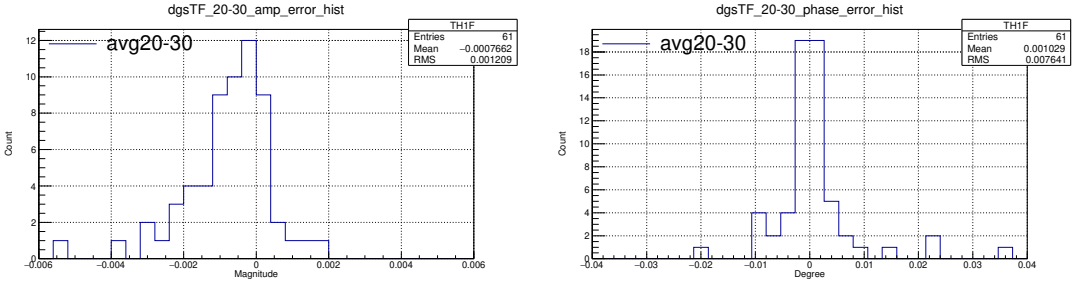

(a) Amplitude (b) Phase

FIGURE 7.22: Histogram of subtraction of 20 times and 30 times average.

Next, we set the average times in average 10 times and change measurement time with 3 situations: 10 cycles-0.1 s, 20 cycles-0.1 s, 10 cycles-0.2 s. We also measure the transfer function and the coherence function. Fig. 7.23 shows the result.

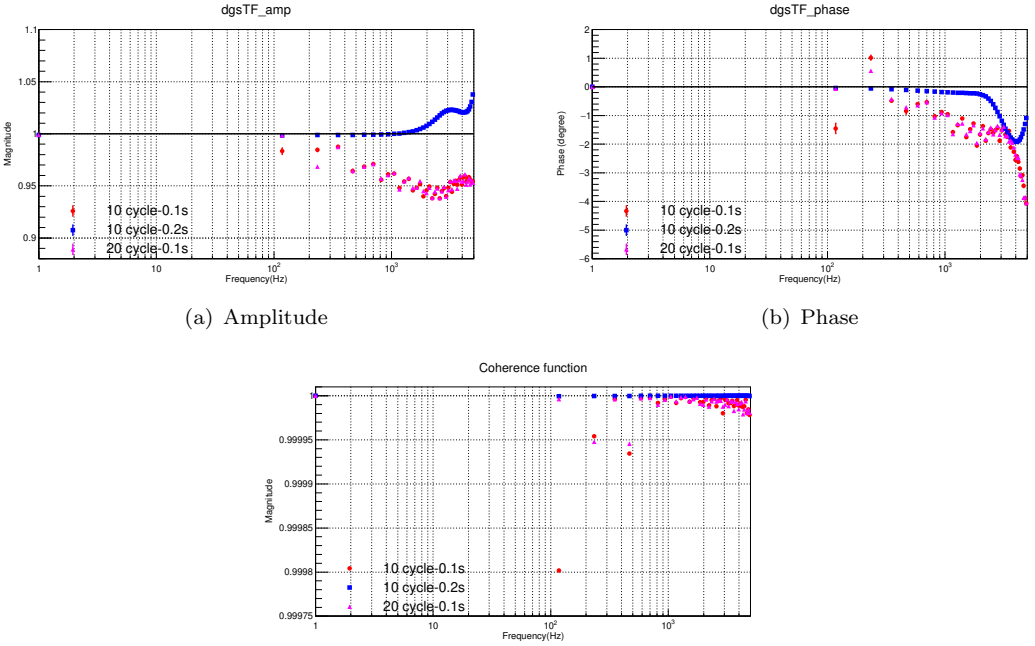

(a) Amplitude (b) Phase

(c) Coherence

FIGURE 7.23: Transfer function of digital system (Change: measurement time) (Sweep type: linear)

From Fig. 7.23, we found that the changing measurement time from 10 cycles to 20 cycles only improve the low frequency which below 100 Hz. But by changing measurement time from 0.1 s to 0.2 s, we can successfully remove the zigzag shape at the high frequency region. Therefore, we understand that the zigzag shape in the transfer function can be removed by increasing average times or measurement time. For the measurement time, Increasing cycles improve the low frequency region, and increasing seconds will improve high frequency region. However, if we increasing too much average times or

measurement time, it will take too much time to finish one measurement. Therefore, from the measured result, we use 10 cycle-0.2 s-10 average times in our following transfer function measurement.

7.4.4 Pcal transfer function

7.4.4.1 Overview

After understanding the transfer function of digital system, we can start measuring the transfer function of Photon Calibrator. In Sec. 7.4.2 we have measured the gain of each detector. We can use these value to calculate the gain of each detector. Fig. 7.15 and Fig. 7.16 shows the diagram of open loop and closed loop setup. In open-loop configuration, the gain of transfer function in each detectors are simply

$$\textbf{OFSPD: } g_1 g_2 g_3 \tag{7.8}$$

$$\textbf{TxPD: } g_1 g_2 g_4 \tag{7.9}$$

$$\textbf{RxPD: } g_1 g_2 g_5 \tag{7.10}$$

In the closed loop configuration, the gain of transfer function in each detectors are

$$\textbf{OFSPD: } \frac{g_1 g_2 g_3}{1 + g_1 g_2 g_3} \tag{7.11}$$

$$\textbf{TxPD: } \frac{g_1 g_2 g_4}{1 + g_1 g_2 g_3} \tag{7.12}$$

$$\textbf{RxPD: } \frac{g_1 g_2 g_5}{1 + g_1 g_2 g_3} \tag{7.13}$$

where g_1 is the gain of OFS, g_2 is the gain of AOM, g_3 is the gain of OFSPD, g_4 is the gain of TxPD, and g_5 is the gain of RxPD.

From Table. 7.6 and Eq. 7.8, Eq. 7.9, Eq. 7.10, Eq. 7.11, Eq. 7.12, Eq. 7.13, we can calculate the gain of transfer function for each detector in both open-loop and closed-loop. The calculated gain is shown in Table. 7.7.

7.4.4.2 Setup

Open-loop: Set the laser power to 20 W and open the OFS control loop. Set the gain value to be 0 dB, 20 dB, 30 dB, and adjust the offset value to make the "To AOM" value be 0.23 V. Open the diaggui set the amplitude to 5 mV, and measure the transfer function from injection port to OFSPD1, OFSPD2, TxPD1, TxPD2, and RxPD.

Gain	Detector	Open-loop [dB]	Closed-loop [dB]
0 dB	OFSPD1	35.10	-0.15
	OFSPD2	35.02	-0.20
	TxPD1	32.51	-0.23
	TxPD2	31.00	-1.71
	RxPD	32.19	-1.76
20 dB	OFSPD1	48.41	-0.03
	OFSPD2	45.82	-0.04
	TxPD1	48.33	-0.11
	TxPD2	44.31	-1.55
	RxPD	45.50	-1.62
30 dB	OFSPD1	58.39	-0.01
	OFSPD2	55.80	-0.01
	TxPD1	58.31	-0.09
	TxPD2	54.29	-1.52
	RxPD	55.48	-1.59

TABLE 7.7: DC Gain of each detectors

Closed-loop: Set the laser power to 20 W and close the OFS control loop. Set the gain value to be 6.8 dB, 20 dB, 30 dB, and adjust the offset value to make the "To AOM" value be 0.23 V. Open the diaggui set the amplitude to 1 V, and measure the transfer function from injection port to OFSPD1, OFSPD2, TxPD1, TxPD2, and RxPD.

7.4.4.3 Result

The open loop transfer function results are shown in Fig. 7.24(6.8 dB gain), Fig. 7.25(20 dB gain), Fig. 7.26(30 dB gain), and the result of closed loop transfer function results are shown in Fig. 7.27(6.8 dB gain), Fig. 7.28(20 dB gain), Fig. 7.29(30 dB gain).

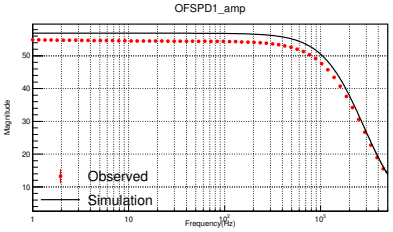

(a) OFSPD1 Amplitude

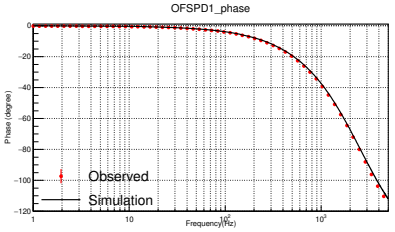

(b) OFSPD1 Phase

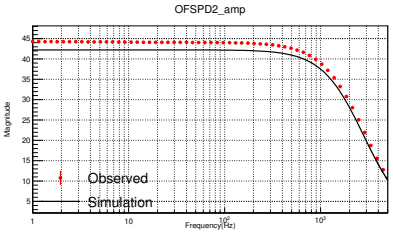

(c) OFSPD2 Amplitude

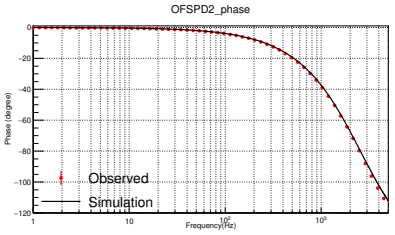

(d) OFSPD2 Phase

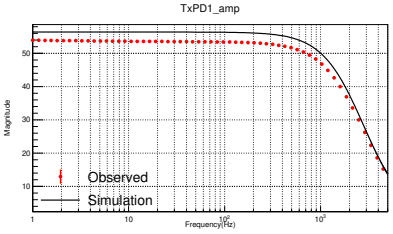

(e) TxPD1 Amplitude

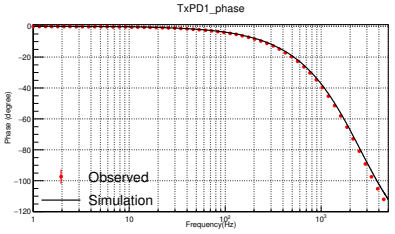

(f) TxPD1 Phase

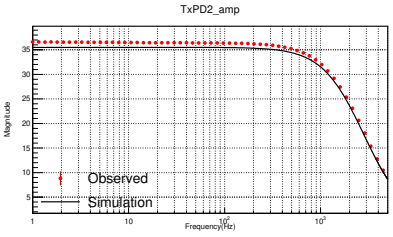

(g) TxPD2 Amplitude

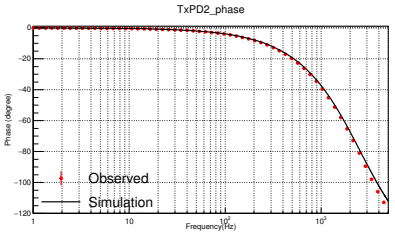

(h) TxPD2 Phase

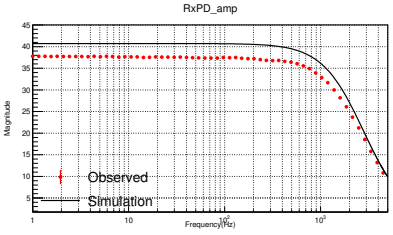

(i) RxPD Amplitude

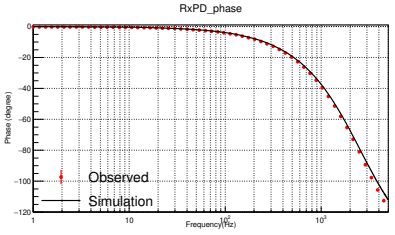

(j) RxPD Phase

FIGURE 7.24: Open loop Transfer function with 6.8 dB gain

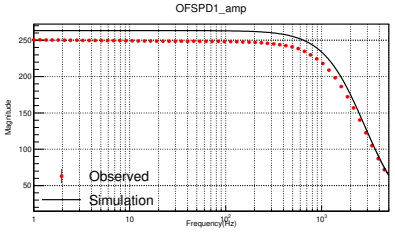

(a) OFSPD1 Amplitude

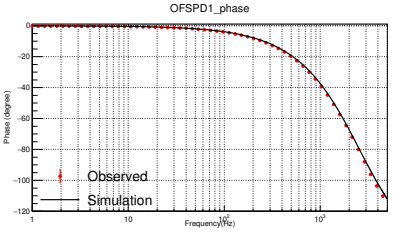

(b) OFSPD1 Phase

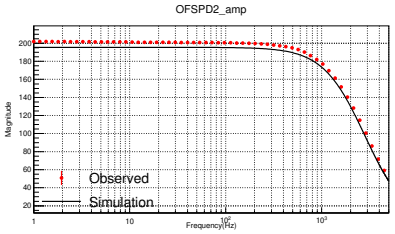

(c) OFSPD2 Amplitude

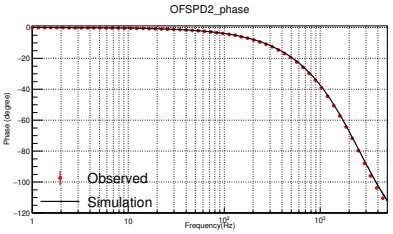

(d) OFSPD2 Phase

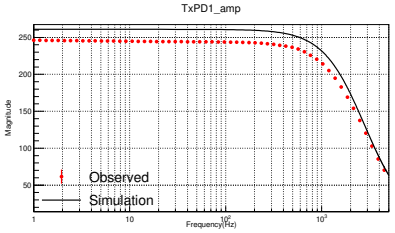

(e) TxPD1 Amplitude

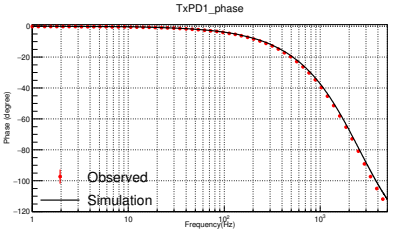

(f) TxPD1 Phase

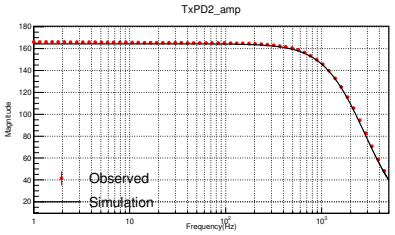

(g) TxPD2 Amplitude

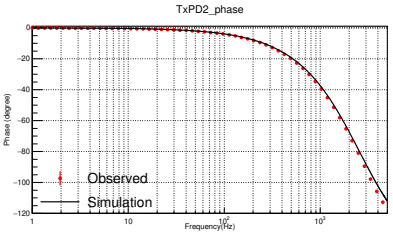

(h) TxPD2 Phase

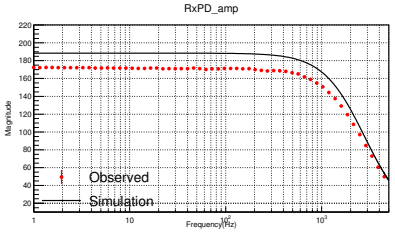

(i) RxPD Amplitude

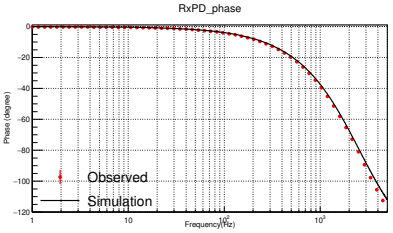

(j) RxPD Phase

FIGURE 7.25: Open loop Transfer function with 20 dB gain

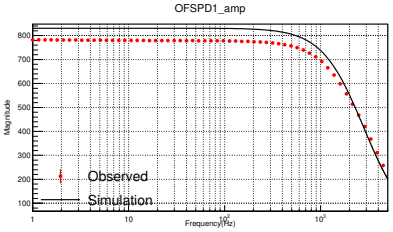

(a) OFSPD1 Amplitude

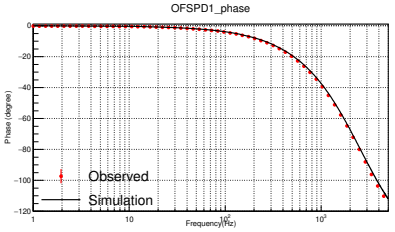

(b) OFSPD1 Phase

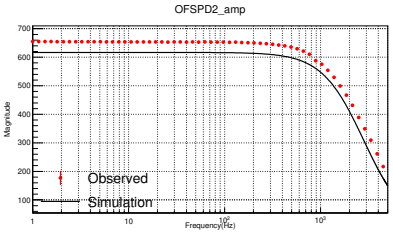

(c) OFSPD2 Amplitude

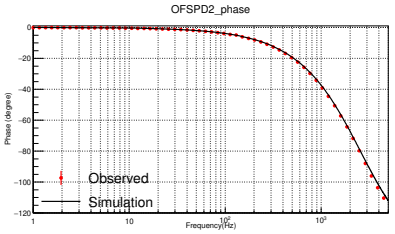

(d) OFSPD2 Phase

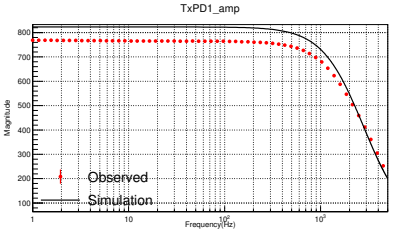

(e) TxPD1 Amplitude

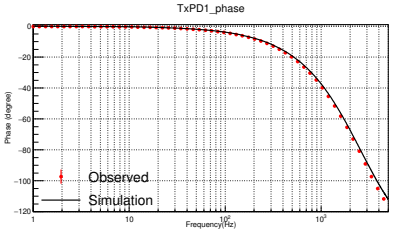

(f) TxPD1 Phase

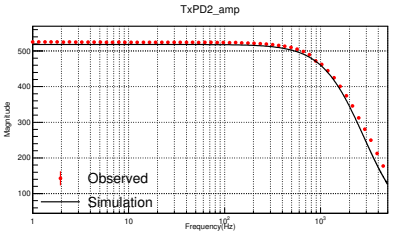

(g) TxPD2 Amplitude

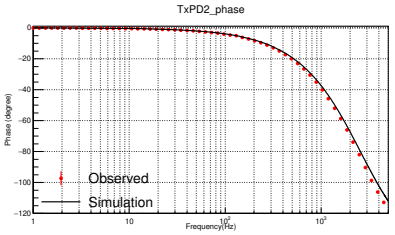

(h) TxPD2 Phase

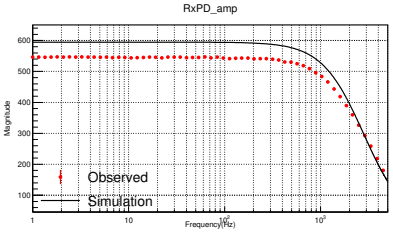

(i) RxPD Amplitude

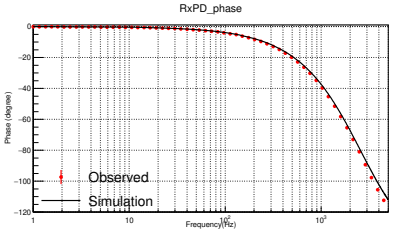

(j) RxPD Phase

FIGURE 7.26: Open loop Transfer function with 30 dB gain

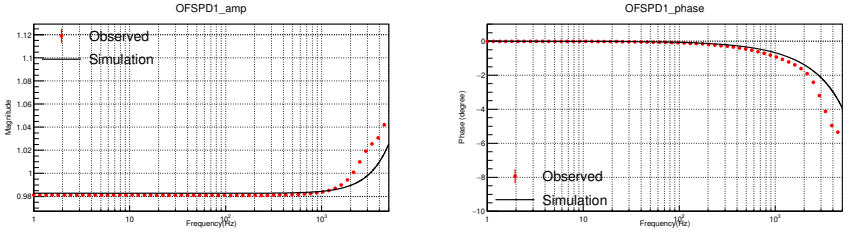

(a) OFSPD1 Amplitude

(b) OFSPD1 Phase

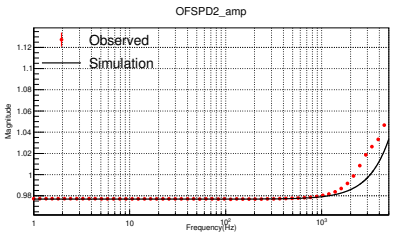

(c) OFSPD2 Amplitude

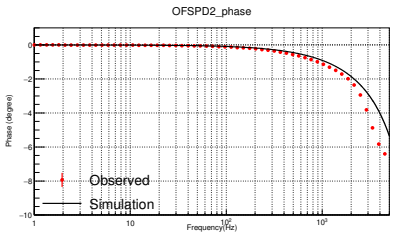

(d) OFSPD2 Phase

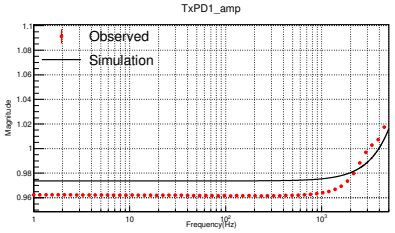

(e) TxPD1 Amplitude

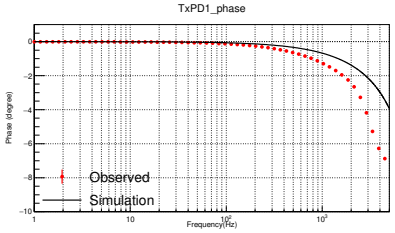

(f) TxPD1 Phase

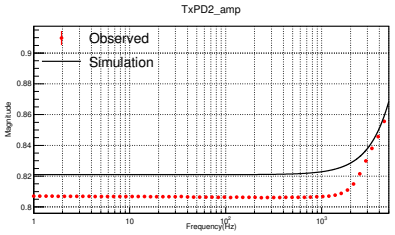

(g) TxPD2 Amplitude

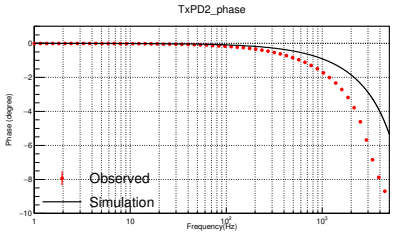

(h) TxPD2 Phase

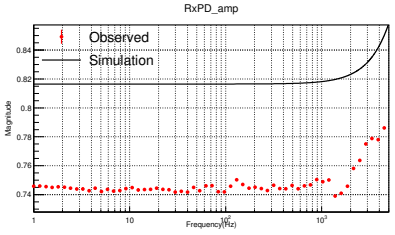

(i) RxPD Amplitude

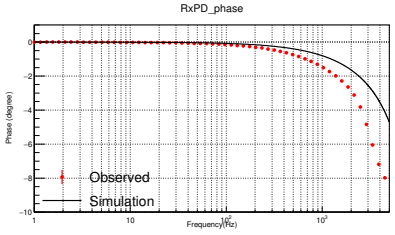

(j) RxPD Phase

FIGURE 7.27: Closed loop Transfer function with 6.8 dB gain

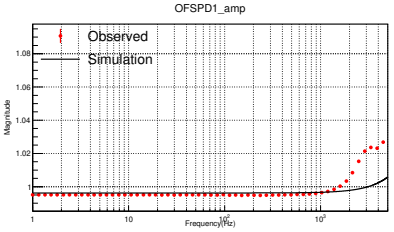

(a) OFSPD1 Amplitude

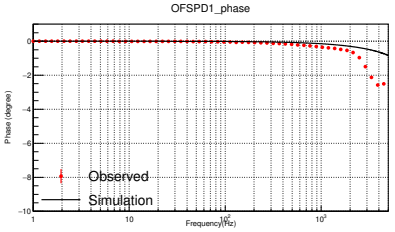

(b) OFSPD1 Phase

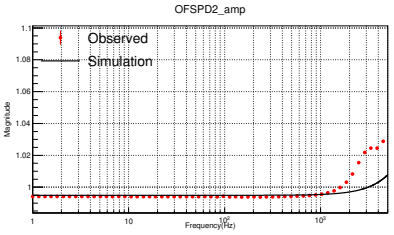

(c) OFSPD2 Amplitude

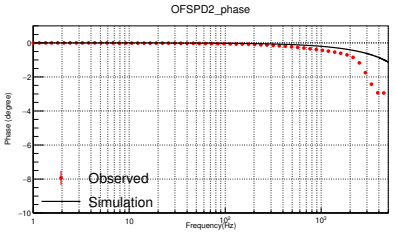

(d) OFSPD2 Phase

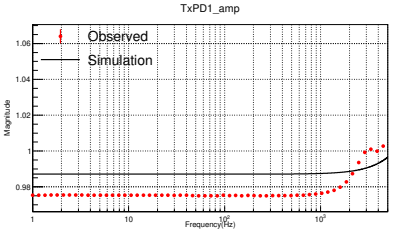

(e) TxPD1 Amplitude

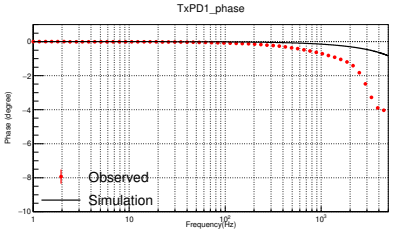

(f) TxPD1 Phase

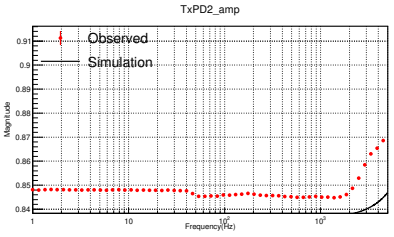

(g) TxPD2 Amplitude

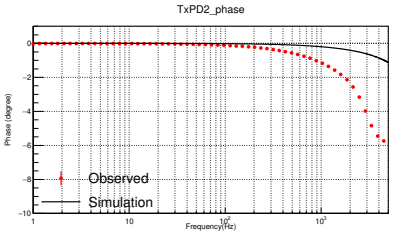

(h) TxPD2 Phase

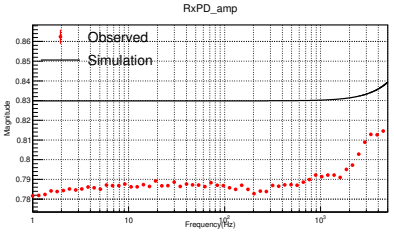

(i) RxPD Amplitude

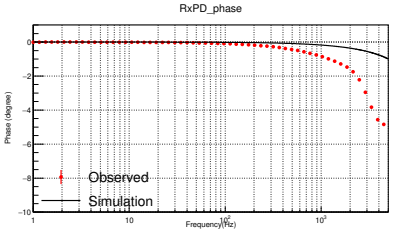

(j) RxPD Phase

FIGURE 7.28: Closed loop Transfer function with 20 dB gain

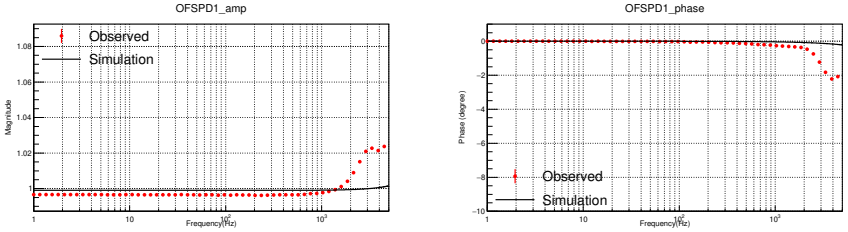

(a) OFSPD1 Amplitude

(b) OFSPD1 Phase

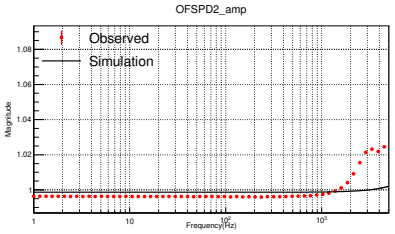

(c) OFSPD2 Amplitude

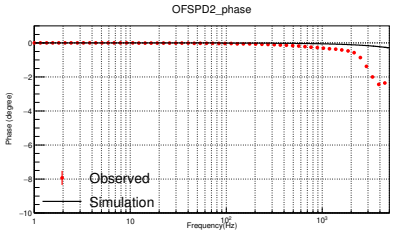

(d) OFSPD2 Phase

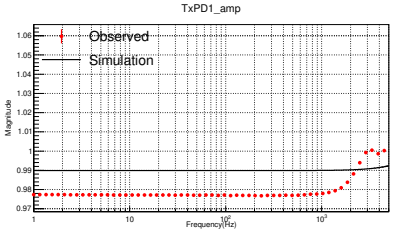

(e) TxPD1 Amplitude

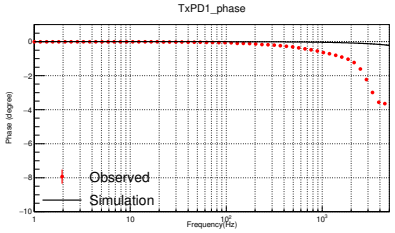

(f) TxPD1 Phase

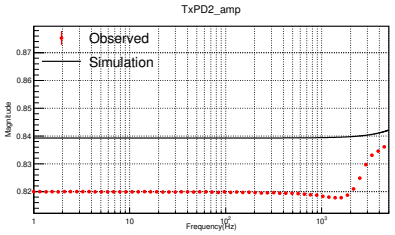

(g) TxPD2 Amplitude

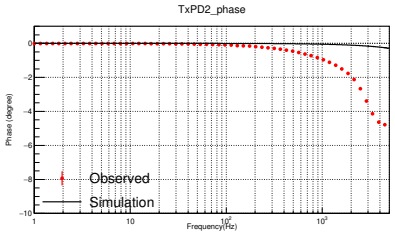

(h) TxPD2 Phase

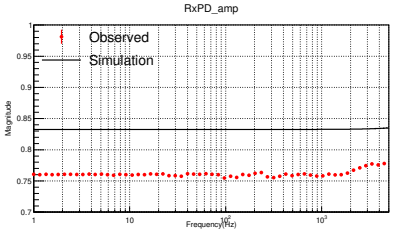

(i) RxPD Amplitude

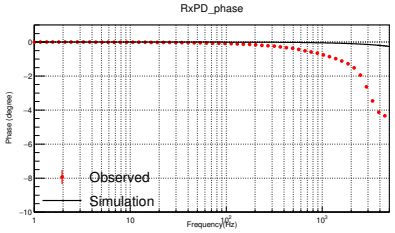

(j) RxPD Phase

FIGURE 7.29: Closed loop Transfer function with 30 dB gain

We can find that DC gain and the tendency of the open-loop transfer function results are close to simulation results. For the closed-loop results, we can see that for OFSPD1 and OFSPD2, the observed results and the simulation results are close to each other in both amplitude and phase. For the TxPD results the observed gain is deviate with the simulated gain. This reason is because we realigned the TxPD position to reduce the measured noise of TxPD, however the transfer function also changed. By re-measuring TxPD transfer function we can make the observed results matches simulation results. In the RxPD result, we can find some zigzag shape in the amplitude figure. This zigzag is not caused by the digital system because we already use the 10 cycle-0.2 s measurement time to remove the zigzags from the digital system. After we finished the measurement, we found that the RxPD value is still fluctuating. This may because when we measure the transfer function, the modulated laser signal is sent to the end test mass and cause the small vibration on end test mass. Since our system is a 72 meter optics, a small vibration in the end test mass would make the beam position in the Rx module fluctuating. Beside, the Airy disk size on the Rx module is almost the same size as Rx integrating sphere, therefore, if the beam position is fluctuating, RxPD cannot receive whole laser power and the RxPD value will also fluctuating. We think that is the reason why there is zigzag shape in RxPD amplitude measurement.

7.5 Noise measurement

Relative power noise measurement is the most important measurement in this thesis. In Sec. 4.6 we calculate the requirement of relative power noise of Pcal. We need to achieve the noise floor to below -140 dB/rtHz. First we made a noise model to understand the noise source. Then we measure the noise source from each instrument. Finally we measure the relative power noise of Pcal, and adjust the gain and offset value of OFS to achieve the lowest RPN floor.

7.5.1 Noise model

To understand the noise of Pcal, we made a model to calculate the noise of Pcal system. The noise model is shown in Fig. 7.30.

We assume the laser power contains a stable power P plus a noise fluctuation n_{laser}. The laser beam injected into AOM and modulated by AOM. The modulated beam consists with original laser power and the AOM DC value T_0 plus AOM noise T'. The modulated beam pass though beam sampler, and the sampled beam is catched by OFSPD. We assume the noise of photodetector to be n_{OFSPD} and the gain to be g_2. The readout of

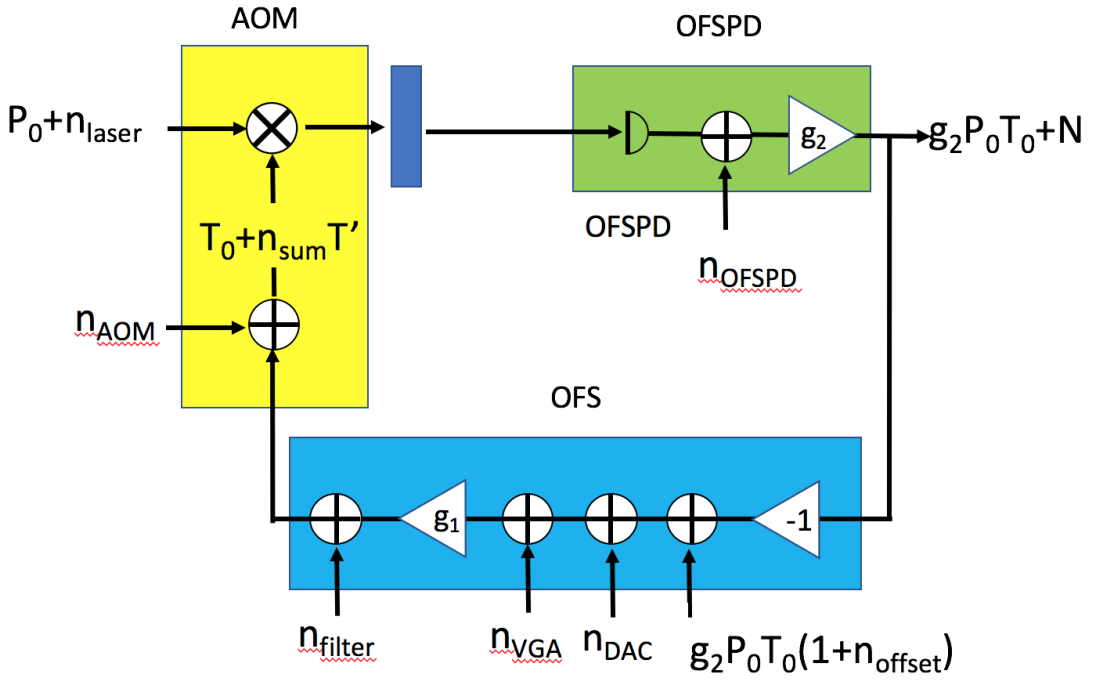

FIGURE 7.30: Noise model

OFSPD then becomes $g_2P_0T_0 + N$, where N is the noise of the readout signal. Then the PD signal is sent to OFS, and we adjust the offset and gain in OFS. The noise of offset port is marked as n_{offset}, and our input value from offset port is $g2P_0T_0 + n_{\text{offset}}$. We assume the noise of VGA is n_{VGA}, and the gain of VGA is g_1. After that the noise of the set of filters is marked as n_{filters}, and the noise of AOM driver is n_{AOM}. The sum of noise from PD output to AOM is called n_{sum}.

The noise of the detector can be described as

$$g_2P_0T_0 + N = g_2((P_0 + n_{\text{laser}})(T_0 + n_{\text{sum}}T') + n_{\text{OFSPD}}) \tag{7.14}$$

where n_{sum} is written as

$$\begin{aligned} n_{\text{sum}} &= n_{\text{AOM}} + g_1(n_{\text{VGA}} + n_{\text{DAC}} + g_2P_0T_0(1 + n_{\text{offset}}) - g_2P_0T_0 - N - g_2n_{\text{OFSPD}}) \\ &= n_{\text{AOM}} + n_{\text{filter}} + g_1(n_{\text{VGA}} + n_{\text{DAC}} + g_2P_0T_0n_{\text{offset}} - N - g_2n_{\text{OFSPD}}) \end{aligned} \tag{7.15}$$

From Eq. 7.14 and Eq. 7.15, we can see

$$\begin{aligned} g_2P_0T_0 + N &= g_2((P_0 + n_{\text{laser}})(T_0 + T'(n_{\text{AOM}} + n_{\text{filter}} + g_1(n_{\text{VGA}} + n_{\text{DAC}} + \\ &\quad g_2P_0T_0n_{\text{offset}} - N - g_2n_{\text{OFSPD}}))) + n_{\text{OFSPD}}) \\ &= g_2(P_0T_0 - P_0T'g_1N + P_0T'(n_{\text{AOM}} + n_{\text{filter}} + g_1(n_{\text{VGA}} + n_{\text{DAC}} \\ &\quad + g_2P_0T_0n_{\text{offset}} - g_2n_{\text{OFSPD}})) + n_{\text{laser}}T_0 + n_{\text{OFSPD}}) \end{aligned} \tag{7.16}$$

$$\begin{aligned} N(1 + g_1g_2P_0T') = g_2(P_0T'(n_{\text{AOM}} + n_{\text{filter}} + g_1(n_{\text{VGA}} + n_{\text{DAC}} + g_2P_0T_0n_{\text{offset}} \\ - g_2n_{\text{OFSPD}})) + n_{\text{laser}}T_0 + n_{\text{OFSPD}}) \end{aligned} \tag{7.17}$$

Finally, the relative power noise of laser can be written as

$$\begin{aligned} \text{RPN} \equiv \frac{N}{g_2P_0T_0} = \frac{1}{1 + g_1g_2P_0T'}(\frac{n_{\text{laser}}}{P_0} + \frac{n_{\text{OFSPD}}}{P_0T_0} + \frac{T'}{T_0}(n_{\text{AOM}} + n_{\text{filter}} \\ + g_1(n_{\text{VGA}} + n_{DAC} + g_2P_0T_0n_{\text{offset}} - g_2n_{\text{OFSPD}}))) \end{aligned} \tag{7.18}$$

7.5.2 Open loop noise

7.5.2.1 Overview

To reduce the noise of the laser, first we need to understand how much the laser noise is. The laser noise is measured as open-loop noise, which we control AOM by sending gain and offset signal to OFS directly, and PD signal is not feedbacked to OFS.

7.5.2.2 Setup

Switch OFS loop to open loop. Set the gain of OFS to 0 V (6.8 dB), and measure the laser noise at AOM working point ("To AOM"=0.23 V). Use diaggui to measure noise spectrum, and divide the noise spectrum by the DC level to get the relative power noise of open-loop noise.

7.5.2.3 Result

The open-loop noise result is shown in Fig. 7.31.

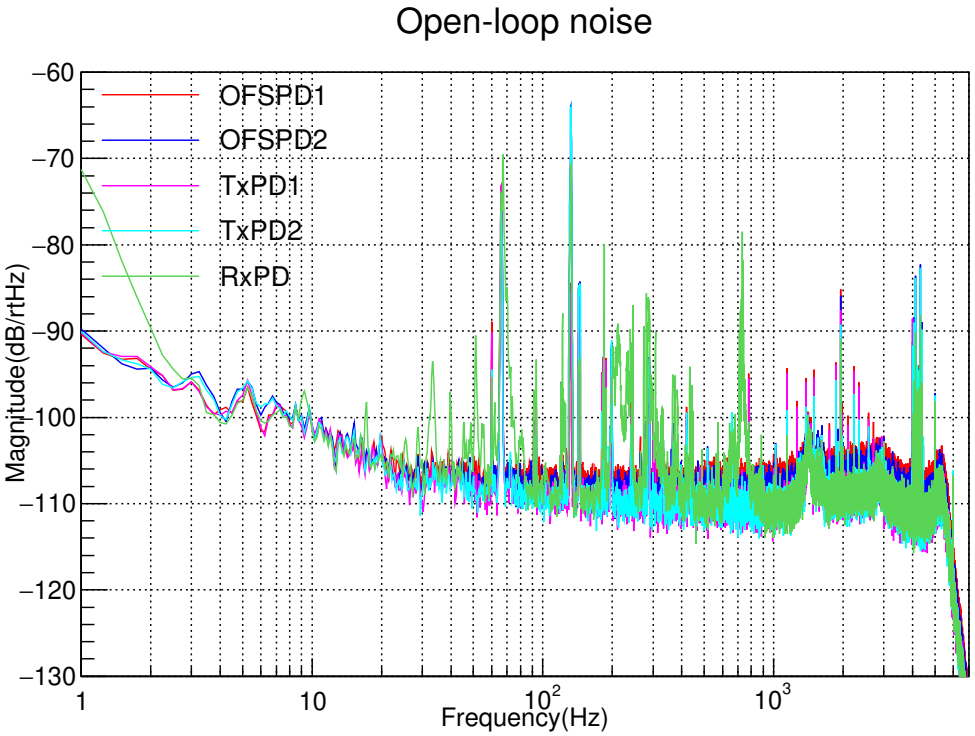

FIGURE 7.31: Open-loop noise

From Fig. 7.31, we can know that the open-loop noise of laser is around -110 dB/rtHz. Next we will investigate other noise sources in the Photon Calibrator.

7.5.3 DAC noise

7.5.3.1 Overview

DAC plays an important role in Photon Calibrator. It provide gain and offset for the OFS, and generate modulated signals to modulate the laser power. The noise of DAC directly propagate to the readout noise of the detectors, therefore, DAC noise is a critical issue. If we have high DAC noise in our digital system, we cannot decrease the noise of our Photon Calibrator.

7.5.3.2 Setup

We connect DAC output port using a 70 meters cable to EYA area, and connect the 70 meters DAC cable to a SR560 amplifier input (Fig. 7.32). SR560 is a low noise preamplifier which we can adjust the type of filters and gain. In our measurements we set the band-pass filter which a high-pass filter at 3 Hz and low-pass filter at 3 kHz in order to remove DC and high frequency noise.

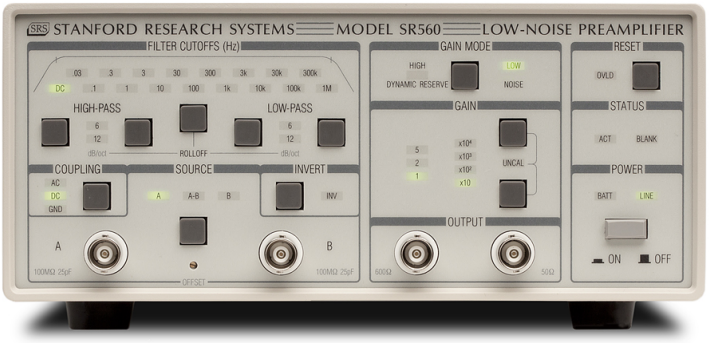

FIGURE 7.32: SR560 low noise amplifier

The amplifier output is connected to 70 meters ADC cable, and we connect 70 meters ADC cable to ADC input port. Set the filter to be a band-pass filter whose pole at 3 Hz and zero at 3 kHz, set gain of amplifier to 100, and use diaggui to measure noise spectrum. The measured noise spectrum is a 100 times amplified noise spectrum. We subtracted the measured result by 40 dBV to get the real noise spectrum. We measure the DAC noise floor in two situations:

1. Change the environmental factors in EYA area.
2. Input DC or AC value from DAC.

7.5.3.3 Result

First, we measured the DAC noise with changing environmental factors. There are ten air cleaners in the EYA clean booth which are used for refreshing the air inside clean booth (Fig. 7.33). The air cleaners generate large sound and vibration, which may be one of the noise source. Therefore we test the DAC noise by switching air cleaner on and off. Next, the ground noise in KAGRA site is not stable. Connecting the electrical device to the ground may transfer the ground noise to the electrical devices. We check it by connecting the power supply of amplifier. Finally, we vibrate the DAC cable by hand to check whether DAC noise level is changed. The measured results are shown in Fig. 7.34.

From Fig. 7.34, we can understand the DAC noise floor is -130 dBV/rtHz. Changing environmental factors did not affect the DAC noise floor. Only when we connected the power supply of the SR560 amplifier, the noise of the ground propagated to the amplifier and increased the DAC noise floor to -100 dBV/rtHz.

FIGURE 7.33: Air cleaner in clean booth (white ones)

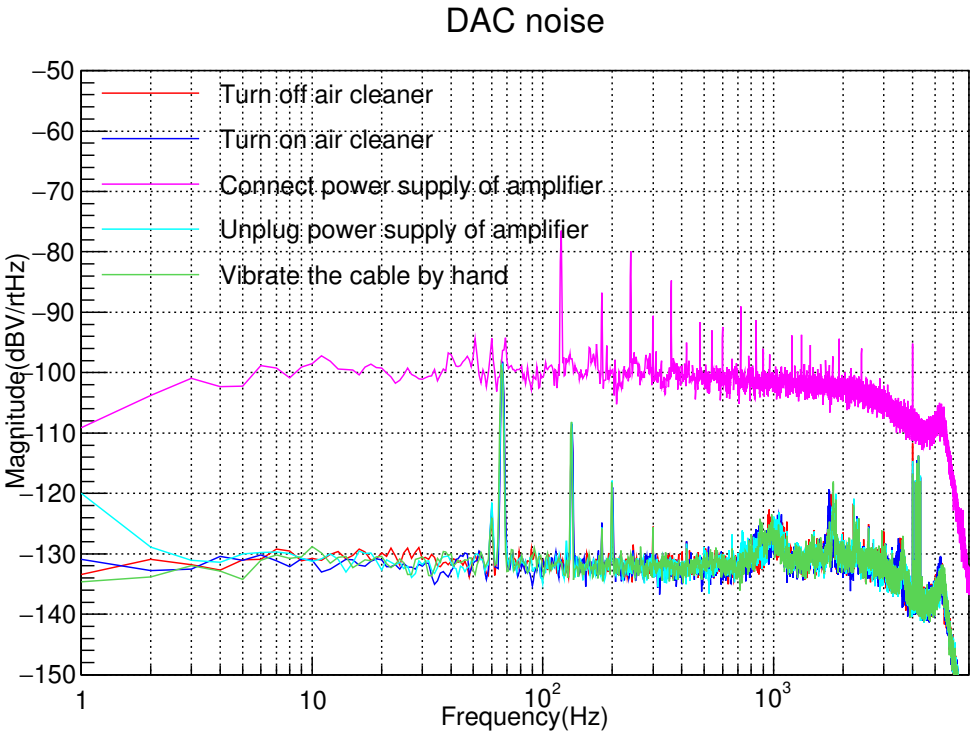

FIGURE 7.34: DAC noise (changing environment)

Next, we input DC and AC signal from DAC to check whether input signals change the noise floor. We send DC voltage with 1 V, 2 V, 5 V, and measure the noise spectrum. The result is shown in Fig. 7.35. Then we change the input signal to AC signal. We set the signal frequency to 300 Hz, and change the peak-to peak amplitude from 1 mV, 10 mV, 100 mV to 1 V. For 1 mV, 10 mV amplitude, we still set the gain of amplifier to 100. For 100 mV amplitude, if we set the gain to 50, the signal will exceed ADC limit. Therefore, we can only set the gain to 20. Similarly, for 1V amplitude I can only set the gain to 5. Since our ADC noise level is -110 dBV/rtHz and DAC noise level is -130 dBV/rtHz, we need at least gain of 10 to see the DAC noise floor from ADC. Therefore we can only measure the upper limit of the noise in 1V peak-to-peak amplitude measurement. The measured result is shown in Fig. 7.36.

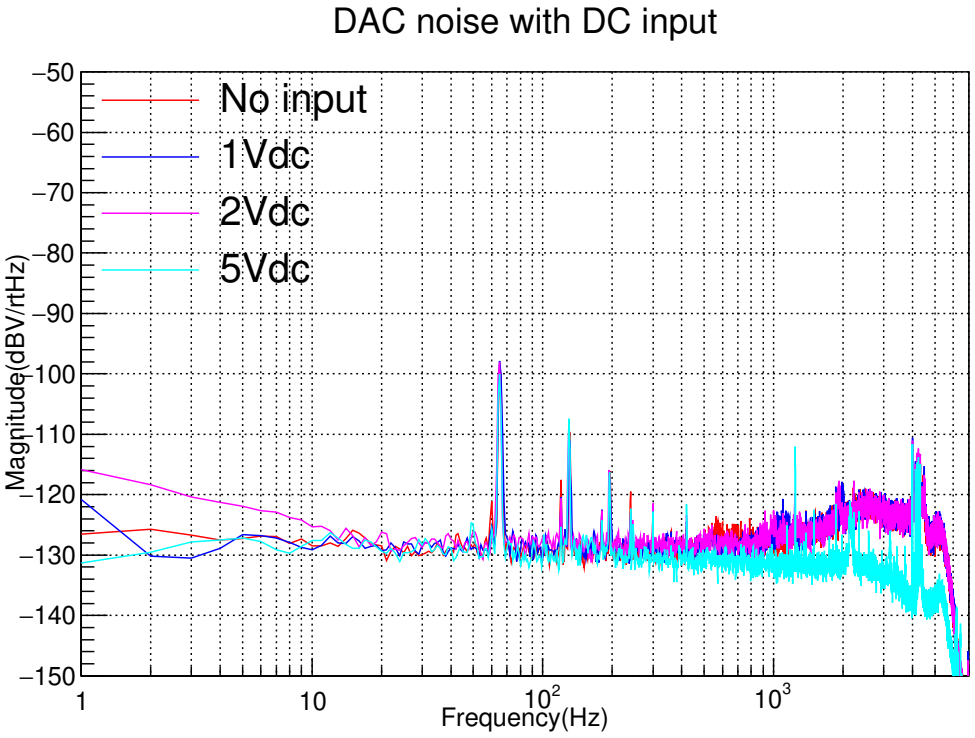

FIGURE 7.35: DAC noise with DC input

From DC result (Fig. 7.35), we can see that the DAC noise floor does not depend on DC voltage level. From AC result (Fig. 7.36), we can also see that DAC noise floor does not depend on AC voltage level. Therefore, we can conclude that our DAC noise floor is -130 dBV/rtHz.

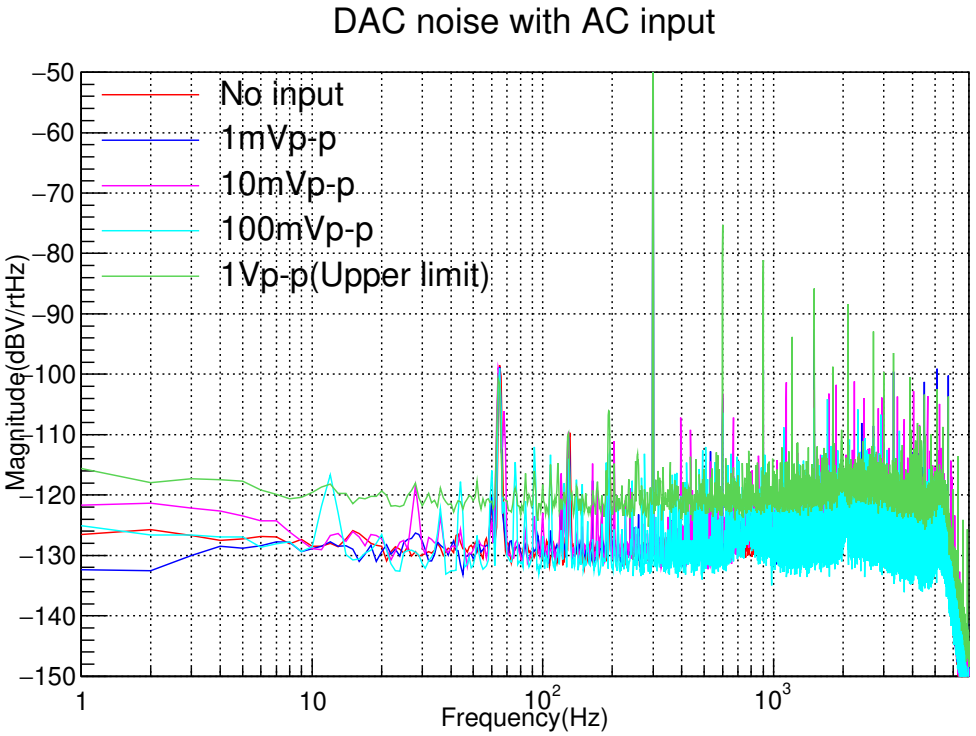

FIGURE 7.36: DAC noise with AC input

7.5.4 VGA noise

7.5.4.1 Overview

In OFS, we employ AD8336 variable gain amplifier(VGA) to adjust the gain and offset of OFS. The noise of VGA directly propagate to the noise of Photon Calibrator. Therefore, we need to understand the noise of VGA.

7.5.4.2 Setup

Set the gain of VGA to be 16.4 dB, 19.7 dB, 29.7 dB, 41.3 dB, the gain of OFS become 6.8 dB, 10 dB, 20 dB, and 31 dB. For each gain, we changed the offset value to see whether the VGA noise depends on DC offset signal. We adjust the DC offset value to make the OFS output to change from 0V to 0.5 V, with 0.1 V step. We connected OFS output to a SR560 amplifier (Fig. 7.32), and set the gain of SR560 to be 100. The output of SR560 is connected to digital system, and we use digital system to measure the noise level of VGA.

7.5.4.3 Result

The VGA results by changing offset are shown in Fig. 7.37, and the result by changing gain is shown in Fig. 7.38.

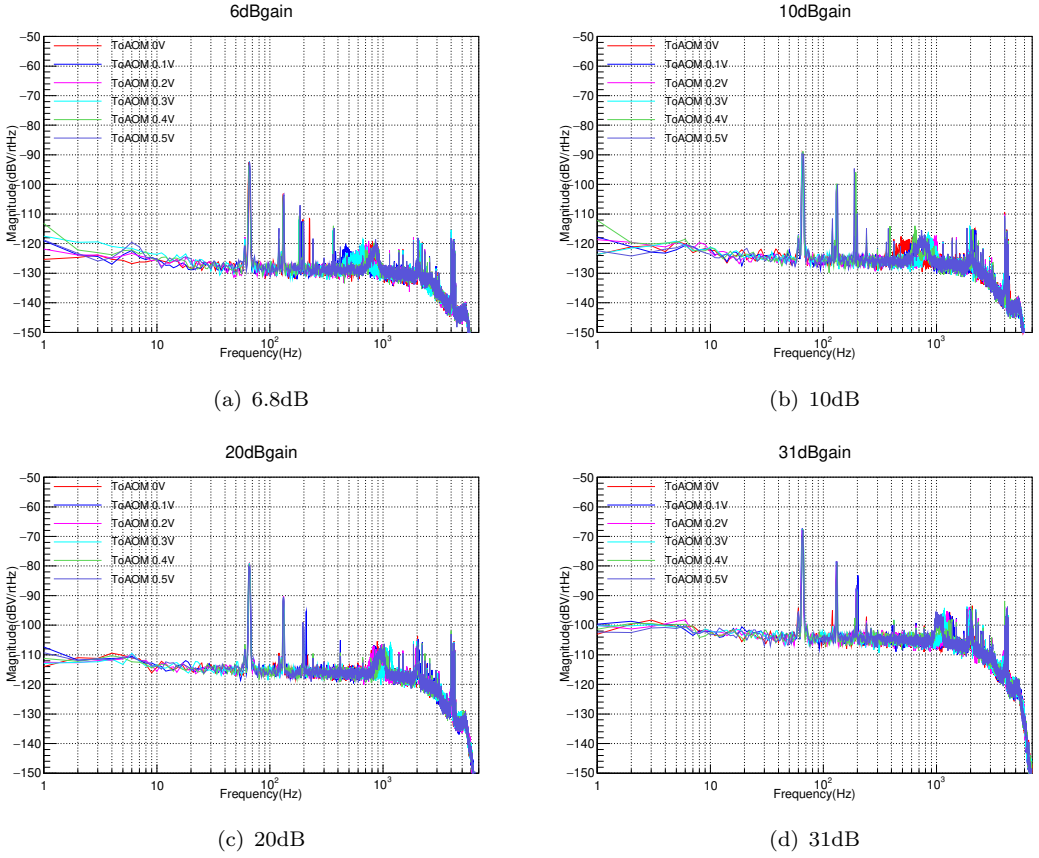

(a) 6.8dB (b) 10dB

(c) 20dB (d) 31dB

FIGURE 7.37: VGA noise by changing offset

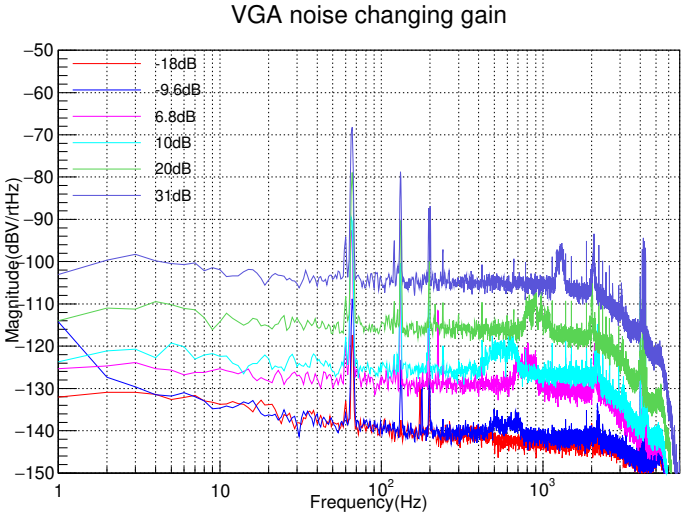

FIGURE 7.38: VGA noise by changing gain

From Fig. 7.37, we can see that the noise level of VGA does not change no matter what offset value is. That is, the noise of DAC is not related to offset value, which is consistent with our measurement in Sec. 7.5.3. However, from Fig. 7.38, the noise level of VGA depends on gain, linear in dB. We plot the noise floor against gain value in Fig. 7.39.

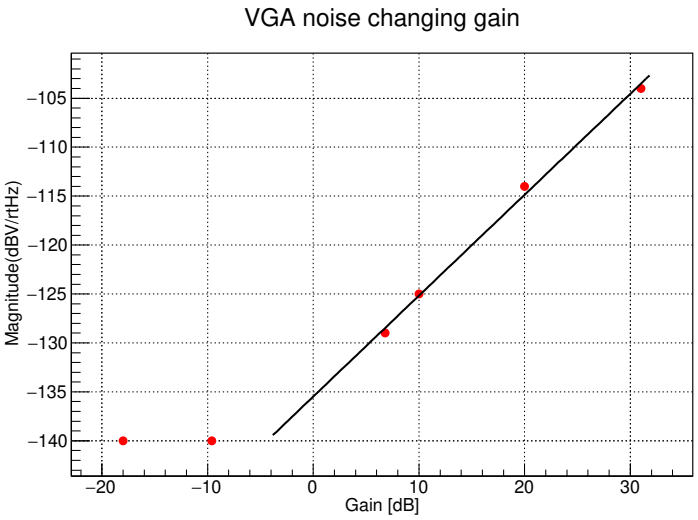

FIGURE 7.39: VGA noise by changing gain

The noise floor of VGA n_{VGA} can be written as

$$n_{\mathrm{VGA}} = -135 + G_{\mathrm{VGA}}[dB] \tag{7.19}$$

where G_{VGA} is the gain of VGA in dB.

7.5.5 Relative Power Noise measurement

7.5.5.1 Overview

Relative Power Noise is one of the important measurement of Photon Calibrator. From Sec. 4.6, we understand that the requirement of relative power noise is -140 dB/rtHz. The main purpose of importing OFS is to decrease the relative power noise. We make a model of relative power noise of the Photon Calibrator and change the gain and offset to see if our model is correct.

7.5.5.2 Setup

We change the gain of OFS to 6.8 dB, 20 dB, 30 dB. For each gain, adjust the offset to make OFS output value be 0.1 V, 0.2 V, 0.3 V, 0.4 V, 0.5 V, and use diaggui to measure

the noise spectrum of OFSPD1, OFSPD2, TxPD1, TxPD2, and RxPD detectors. To monitor the amplified noise remotely with multiple channels, we put a high pass filter whose zero at 1 Hz and a pole at 10 Hz to remove the DC signal. After that we placed a whitening filter which is a high boost filter shown in Fig. 7.40. We remove the effect of whitening filters and digital system filters to show the real RPN level of Pcal.

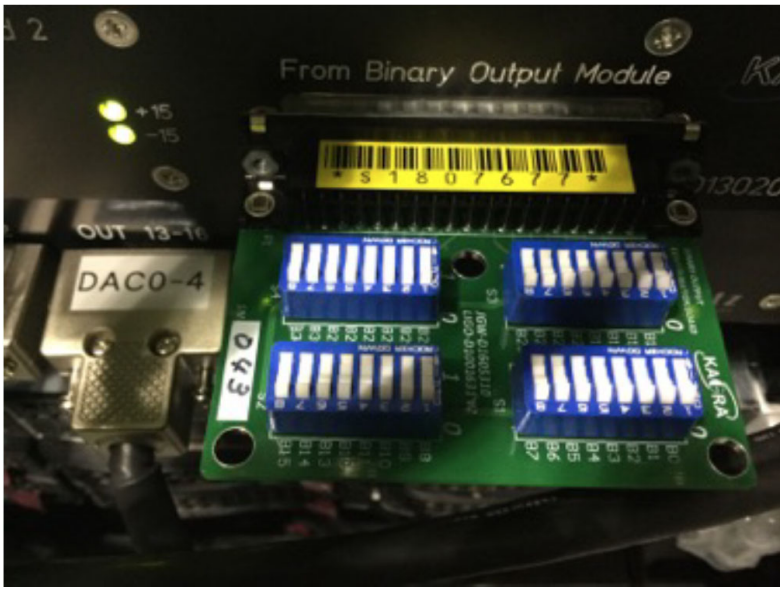

FIGURE 7.40: Whitening filter

The gain of the whitening filter is set to 100 make the noise level of each detector exceed the ADC noise level. Record the mean value of each detector in each measurement. Divide the noise spectrum by mean value of corresponding detectors to get the relative power noise.

7.5.5.3 Result

Fig. 7.41, Fig. 7.42, and Fig. 7.43 show the relative power noise with 6.8 dB, 20 dB, 30 dB gain. For each gain, we measure the RPN for 5 detectors, and for each detector we measure RPN with different V_{AOM} voltage. The noise floor of RPN is summarized in Table. 7.8. We plot the noise floor against AOM input voltage in Fig. 7.44, Fig. 7.45, and Fig. 7.46.

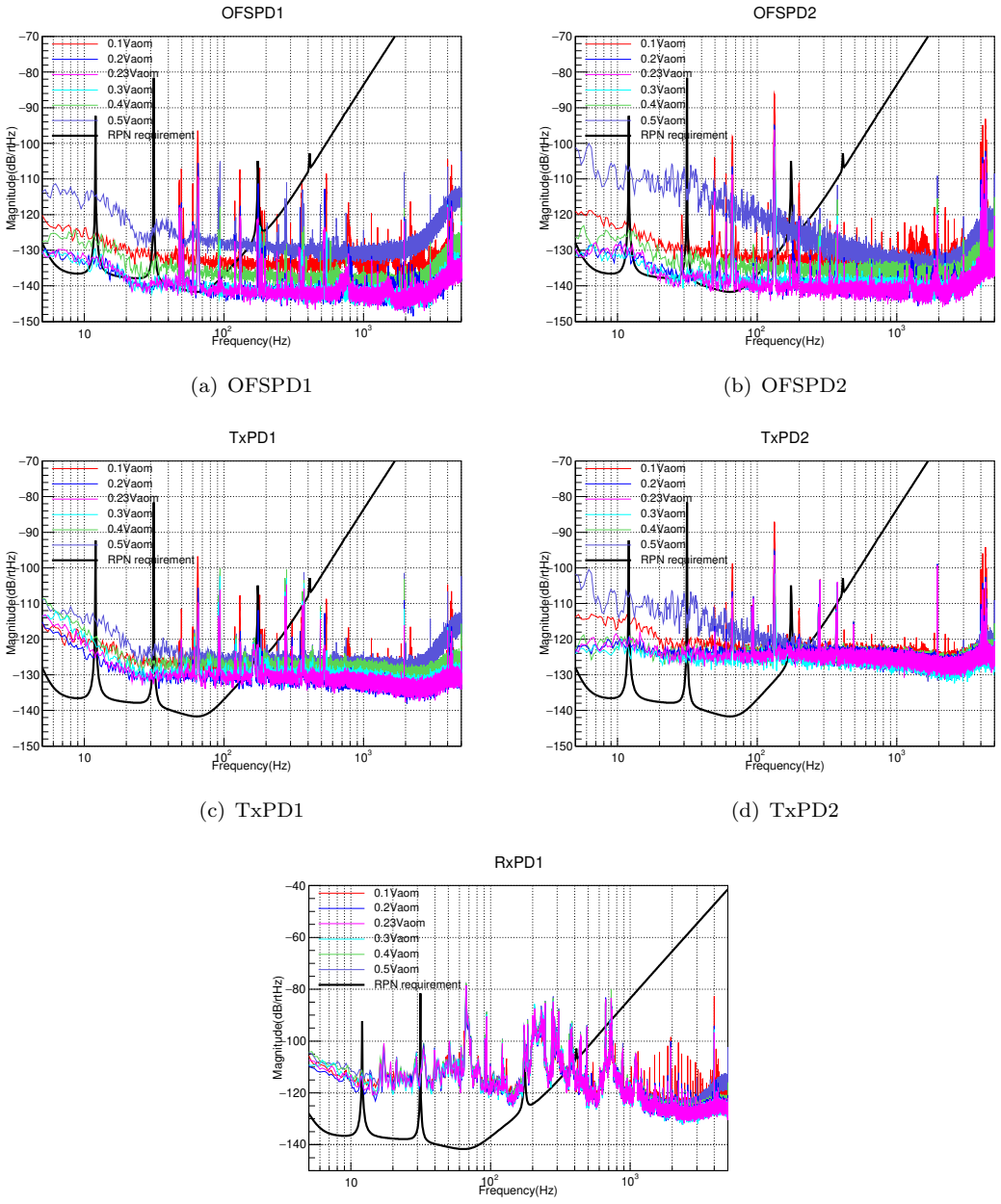

(a) OFSPD1

(b) OFSPD2

(c) TxPD1

(d) TxPD2

(e) RxPD

FIGURE 7.41: Relative Power Noise with 6.8dB gain

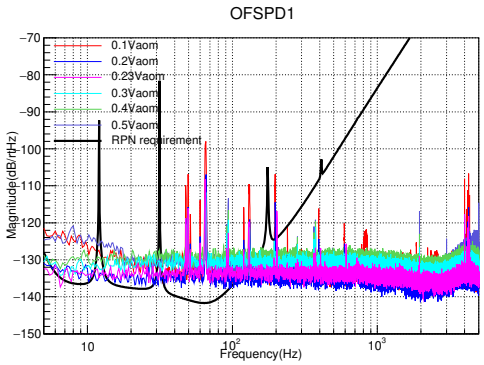

(a) OFSPD1

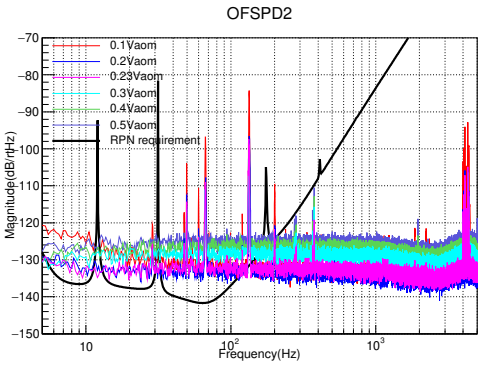

(b) OFSPD2

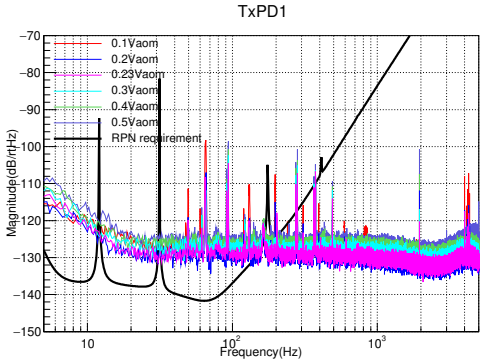

(c) TxPD1

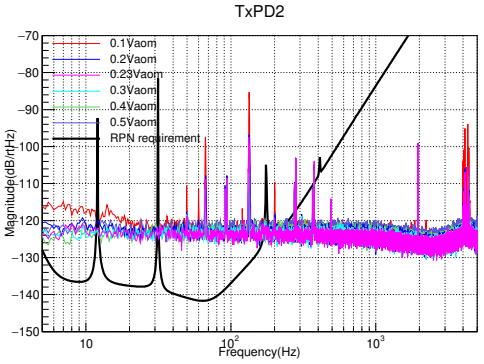

(d) TxPD2

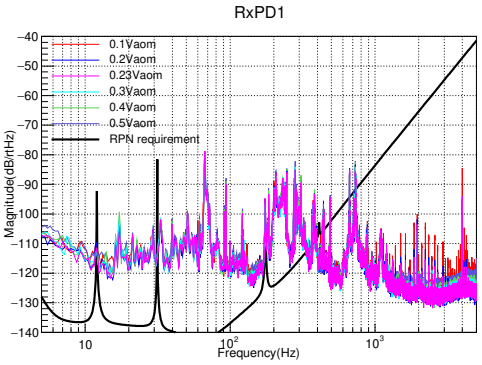

(e) RxPD

FIGURE 7.42: Relative Power Noise with 20dB gain

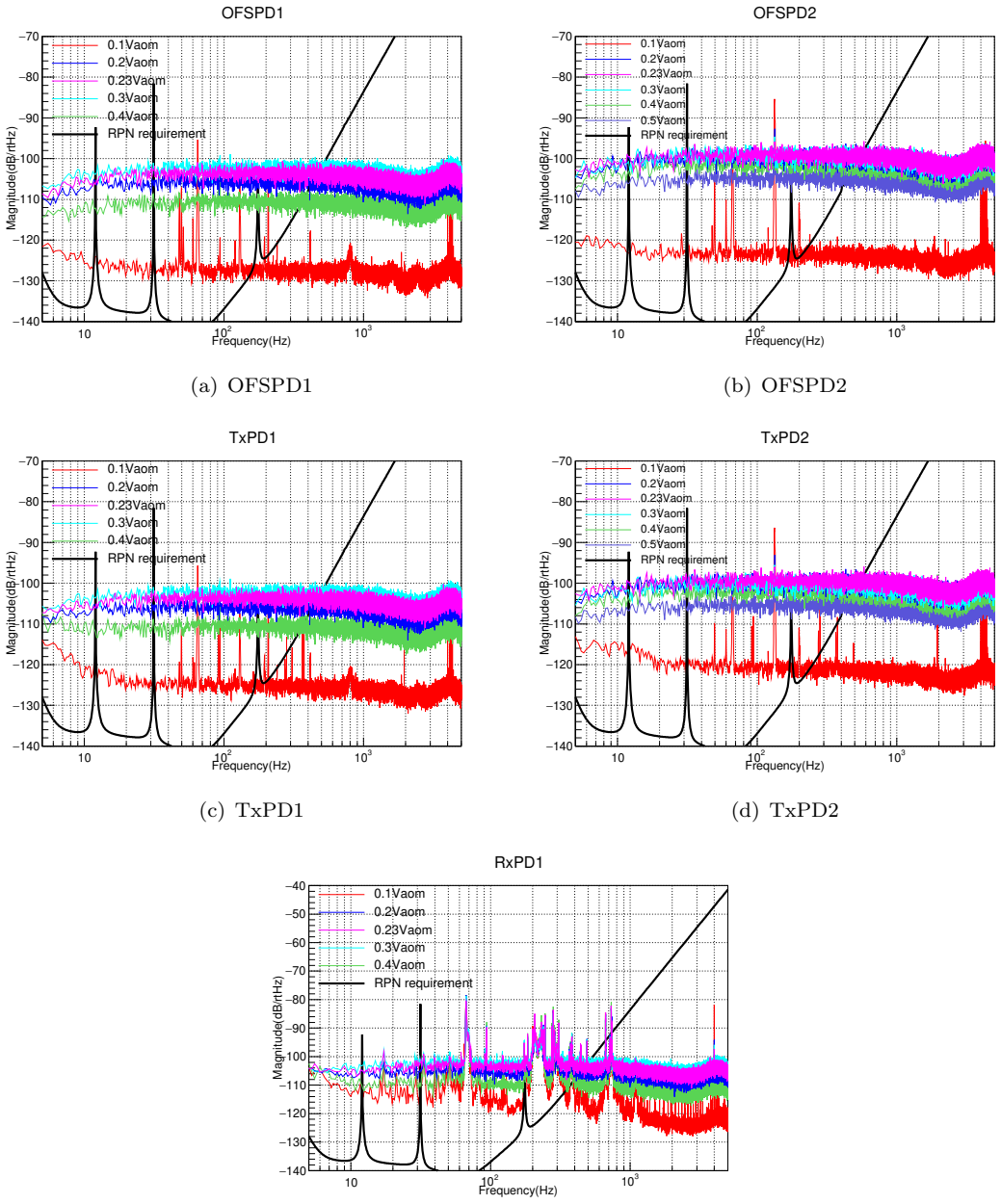

(a) OFSPD1

(b) OFSPD2

(c) TxPD1

(d) TxPD2

(e) RxPD

FIGURE 7.43: Relative Power Noise with 30dB gain

Gain	V_{AOM} [V]	OFSPD1	OFSPD2	TxPD1	TxPD2	RxPD
6.8 dB	0.1	-135	-133	-128	-123	-125
	0.2	-143	-141	-131	-123	-125
	0.23	-143	-141	-131	-125	-125
	0.3	-143	-140	-130	-125	-125
	0.4	-138	-135	-128	-125	-125
	0.5	-130	-130	-127	-123	-125
20 dB	0.1	-134	-132	-128	-123	-124
	0.2	-136	-134	-130	-123	-124
	0.23	-134	-134	-130	-123	-124
	0.3	-131	-129	-128	-123	-124
	0.4	-129	-127	-127	-123	-124
	0.5	-131	-125	-125	-121	-124
30 dB	0.1	-128	-124	-126	-121	-120
	0.2	-108	-106	-106	-102	-107
	0.23	-105	-100	-104	-100	-105
	0.3	-103	-102	-102	-102	-104
	0.4	-111	-103	-112	-104	-110
	0.5	-	-106	-	-106	-

TABLE 7.8: Noise floor with each gain and offset. Unit: [dB/rtHz]

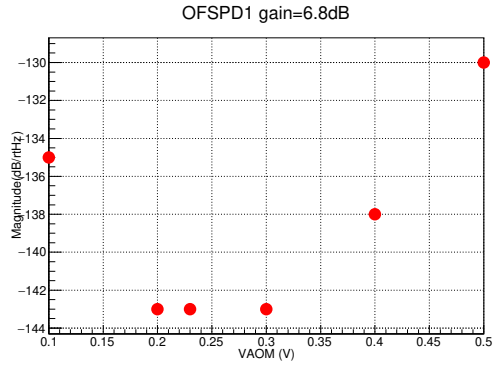

(a) OFSPD1

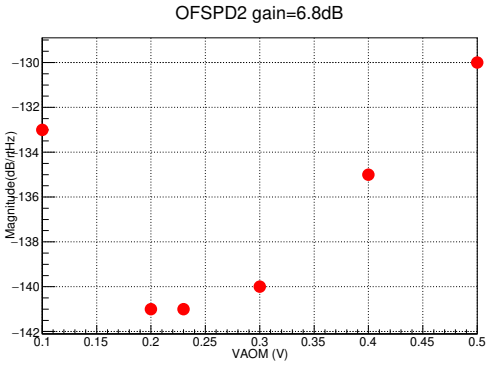

(b) OFSPD2

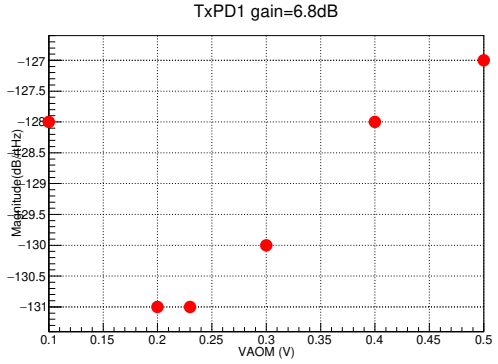

(c) TxPD1

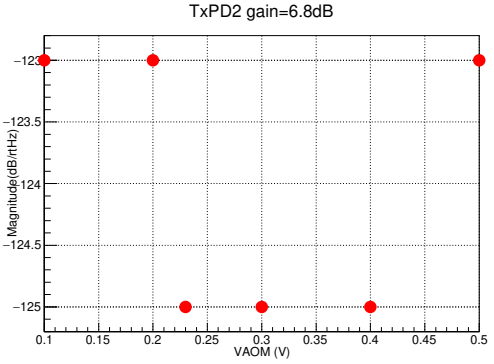

(d) TxPD2

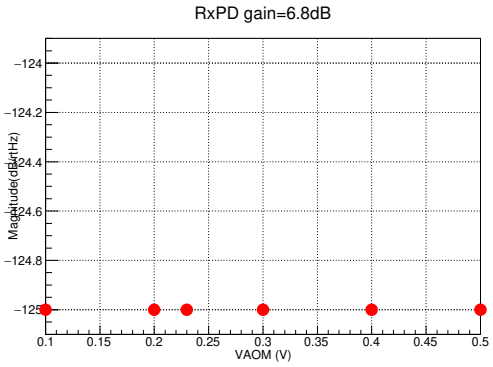

(e) RxPD

FIGURE 7.44: Relative Power Noise with 6.8dB gain

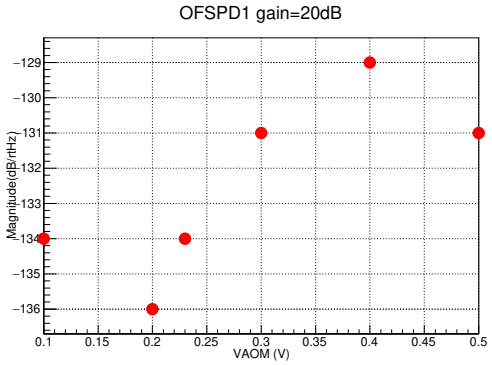

(a) OFSPD1

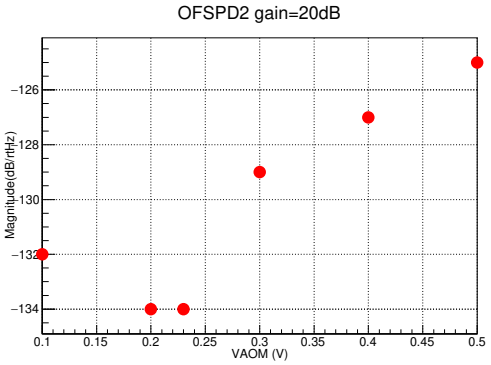

(b) OFSPD2

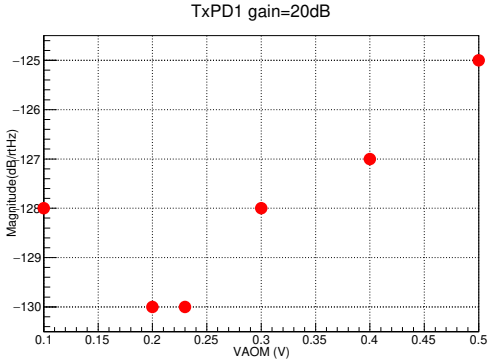

(c) TxPD1

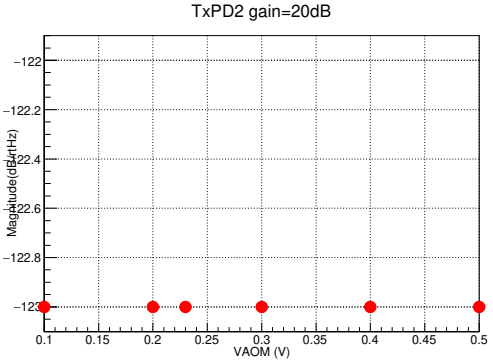

(d) TxPD2

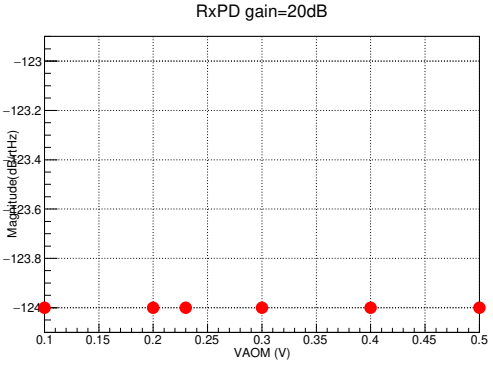

(e) RxPD

FIGURE 7.45: Relative Power Noise with 20dB gain

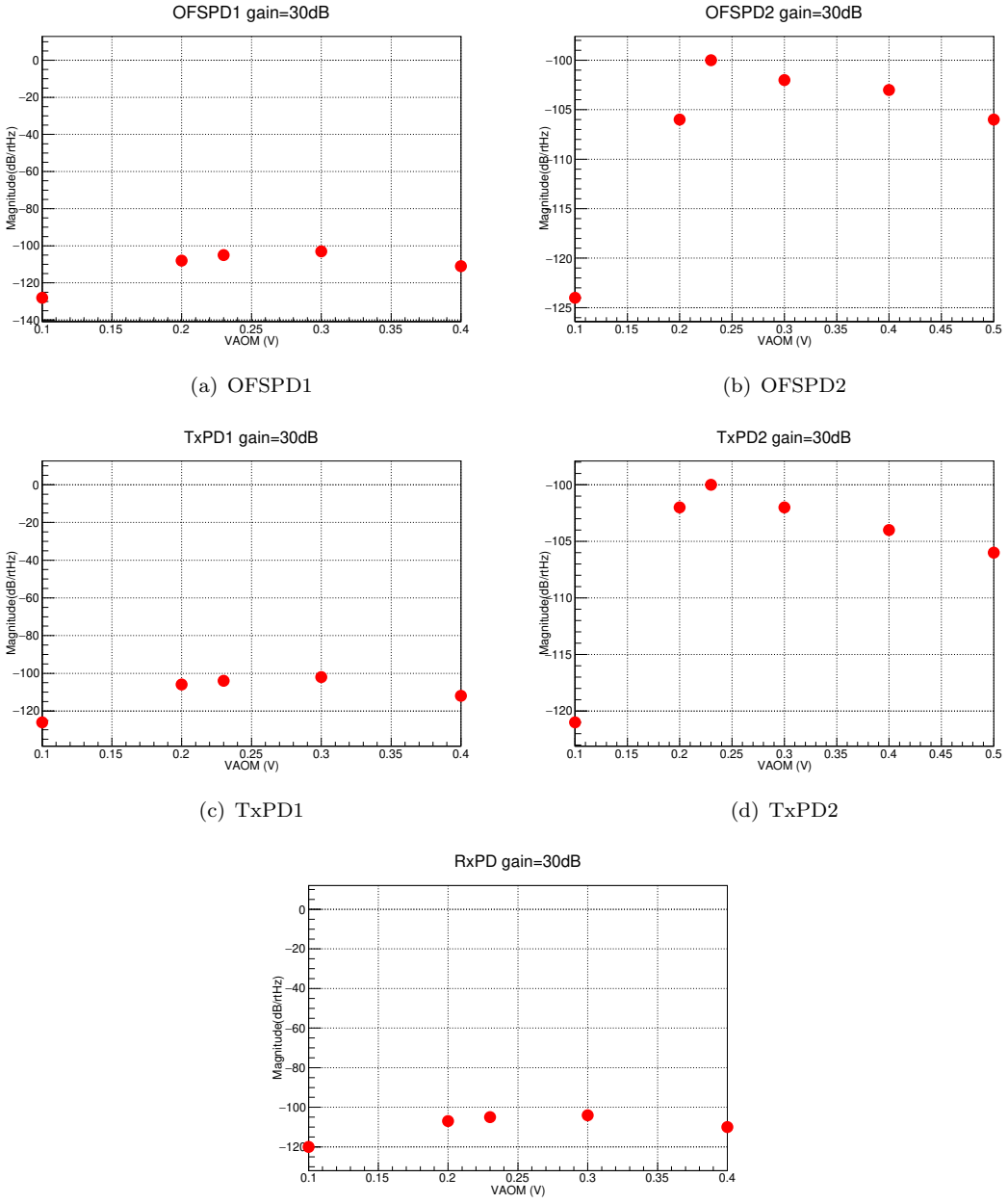

(a) OFSPD1

(b) OFSPD2

(c) TxPD1

(d) TxPD2

(e) RxPD

FIGURE 7.46: Relative Power Noise with 30dB gain

From the result, we can see when "To AOM value" is 0.23 V the relative power noise has the lowest value. When the gain is 6.8 dB, RPN has the lowest value, and the noise floor of OFSPDs are lower than -140 dB/rtHz, and the corresponding TxPD is -130 dB/rtHz, and RxPD is -125 dB/rtHz. When we increase the gain, the noise floor also increases.

Comparing Table. 7.8 and Eq. 7.18, we found that by changing offset value, we are actually changing the T_0 value, which is the DC value of AOM. When offset value increase, T_0 increases, then the RPN should decrease. However, we found that the minimum point of RPN happens at V_{AOM} is around 0.23 V. When we increase V_{AOM} to

above 0.23 V, the RPN also increases. This shows that the noise of AOM T' depends on the AOM DC value T_0. According to Fig. 7.17, we can find that the AOM transmittance curve is nearly linear when V_{AOM} equals 0.23 V, and when V_{AOM} is 0 V or 5 V it has a curve shape. We think that T' has the maximum value at V_{AOM} equals 0 V and 0.5 V, and has the minimum value at V_{AOM} equals 0.23 V.

Next, when we change the gain of OFS, we are changing g_1 in the Eq. 7.18. The RPN is proportional to the term $n_{\text{VGA}} + n_{\text{DAC}} + g_2 P_0 T_0 n_{\text{Offset}} - g_2 n_{\text{OFSPD}}$ with the gain g_1, especially from Eq. 7.19 we can see the noise of VGA also increases when the gain of VGA increases. The observed result matches our estimated model.

Furthermore, we found that the output VGA noise from specification sheet is shown in Fig. 7.47. The OFS gain 6.8 dB, 20 dB, 30 dB correspond to V_{VGA} equals 0 V, 0.26 V, 0.5 V. We can found that when V_{VGA} is over than around 0.3 V the noise of VGA increases significantly. This result also correspond with our measured results.

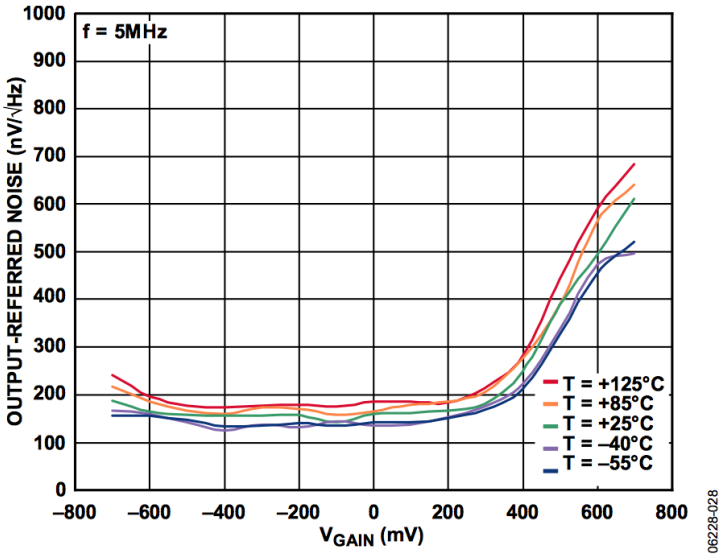

Figure 28. Output-Referred Noise vs. V_{GAIN} at Various Temperatures (T) (See Figure 62)

FIGURE 7.47: Output noise of VGA

7.5.6 Peak identification

7.5.6.1 Overview

From the relative power noise measurement result, we found that there were many peaks in Rx module. We want to understand where those peaks come from. We performed the hammmering test to identify the source of each peaks.

7.5.6.2 Setup

Use the hammer to hit a specific position and monitor the noise spectrum of RxPD. If the peak increases when we perform the hammering test, we can understand that the peak comes from the vibration of that specific position. By fixing that position and making it become stable, we can reduce the peaks. We performed the hammering test at the following 10 positions: Tx stand, Tx optical table, Tx module wall, Tx cover, Tx duct, Tcam duct, EYA chamber wall, EYA chamber floor, Rx stand, Rx duct. There are also 10 air cleaners in the EYA chamber in order to maintain the air clean inside EYA clean booth. We also turned off the air cleaner to check the noise peak affected by air cleaner.

7.5.6.3 Result

The results of hammering test in 12 different conditions are shown in Fig. 7.48. The red arrows show the peaks which increases when we use hammer to hit the certain region. The region then becomes the suspected peak source.

Finally, we can distinguish the suspected source of each peak in RxPD. The result is shown in Fig. 7.49.

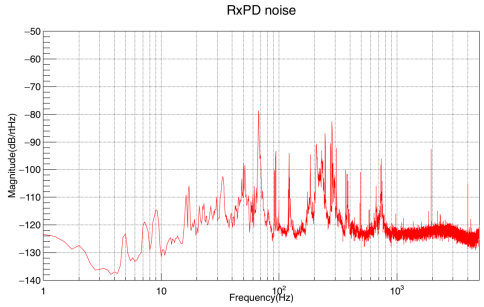

(a) No hammering test

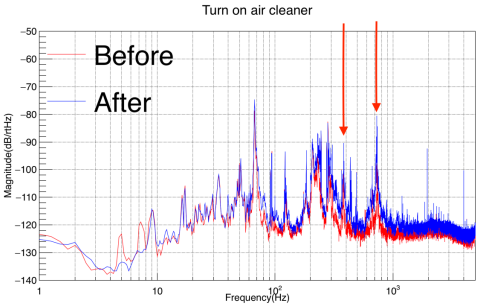

(b) Turn on air cleaner

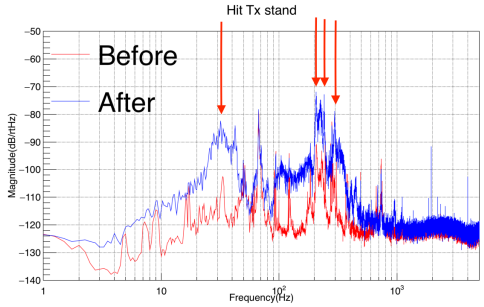

(c) Hammering test on Tx stand

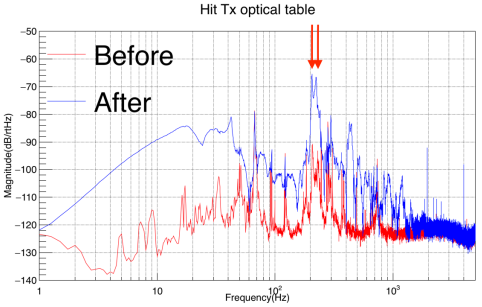

(d) Hammering test on Tx optical table

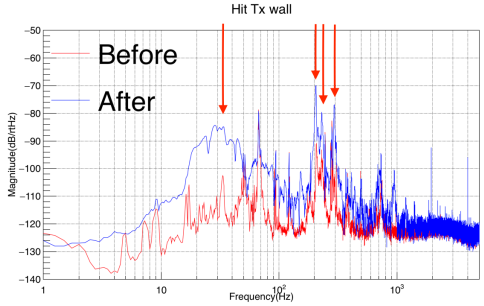

(e) Hammering test on Tx wall

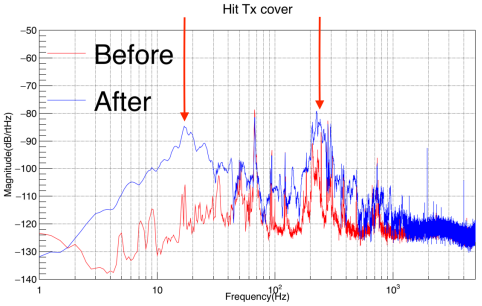

(f) Hammering test on Tx cover

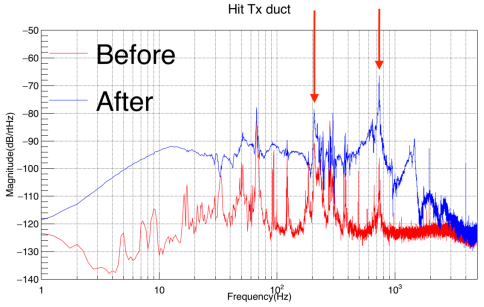

(g) Hammering test on Tx duct

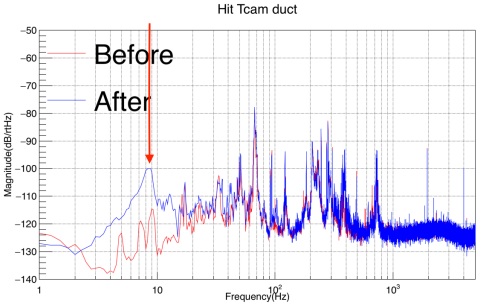

(h) Hammering test on Tcam duct

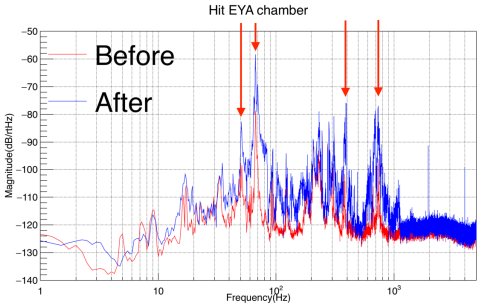

(i) Hammering test on EYA chamber

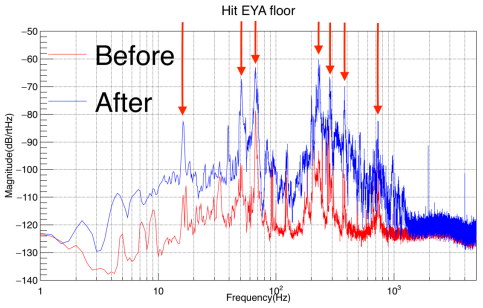

(j) Hammering test on EYA floor

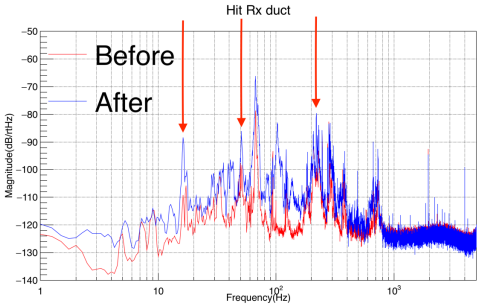

(k) Hammering test on Rx duct

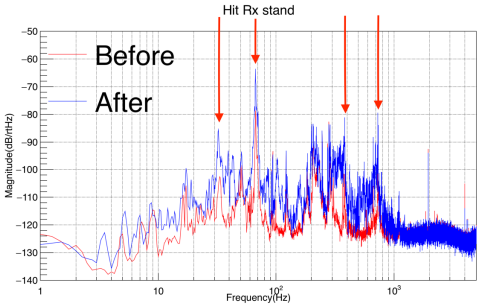

(l) Hammering test on Rx stand

FIGURE 7.48: Hammering test

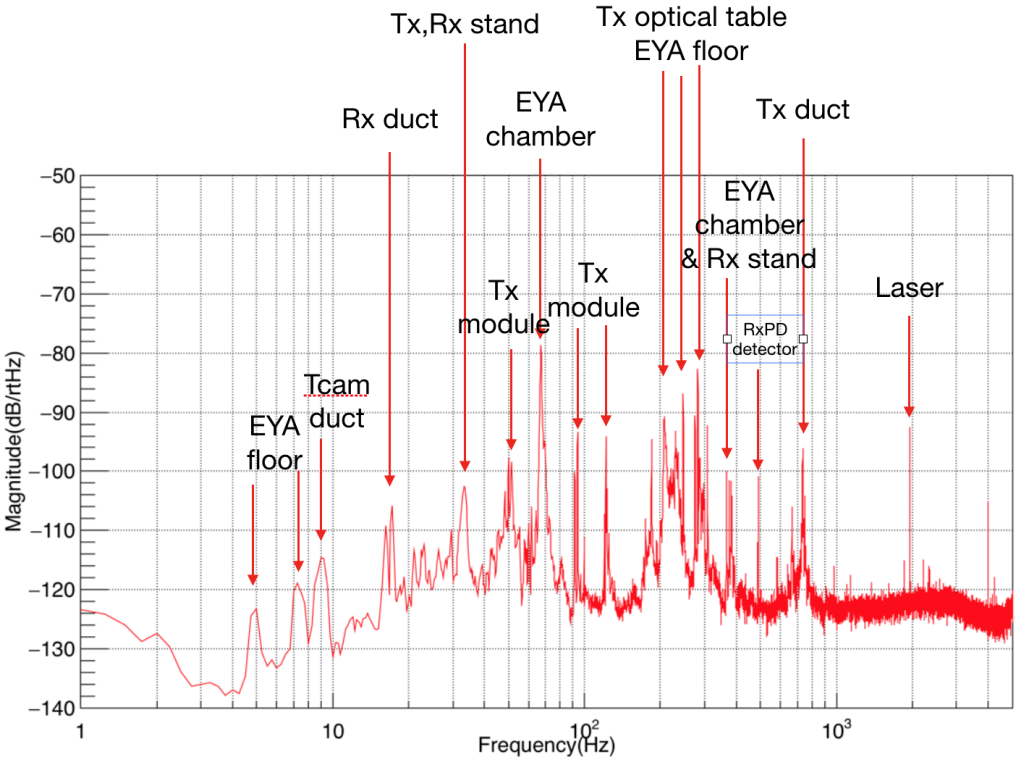

FIGURE 7.49: Peak identification in the RxPD. The red arrow shows the suspected region which generate the peak

7.6 Summary

In this chapter we introduce the integration test to measure the performance of Pcal. The first measurement is power loss measurement. We checked at which stage does the power loss happens. The main reason of our power loss is because the size of Airy disk is larger than our power meter so we cannot measure the full power. Next we did the measurement of transmittance of AOM and each photodetectors. The purpose of this measurement is to understand the performance of AOM and each detectors, and also use for calculate the expected DC gain of transfer function of Pcal. Third, we measure the open-loop and closed-loop transfer function and compare to the simulation result. Since there is some deviation of DC gain, we need to measure the transfer function of each detector again. Finally we measured relative power noise with adjusting gain and offset of OFS. We achieved in-loop PD noise to -140 dB/rtHz, and out-loop PD noise to -130 dB/rtHz. We still need to decrease the out-loop PD noise to below our requirement curve. We also find many peaks in RxPD detector, so we performed hammering tests to check where the each peaks come from. Finally, we summarized the suspected region of peak sources.

Chapter 8

Discussion

8.1 Remaining Issues

8.1.1 Transfer function

In the transfer function of digital system, the statistical error is inconsistent with the total error, which means there is systematic error exists in the digital system transfer function. From the result of setting average times to 20 and 30 times, we can see that the systematic error is frequency dependent, which increases when frequency is larger than 8 Hz. To understand the error of Pcal transfer function, we need to understand the systematic error of digital system transfer function.

For the Pcal transfer function, the DC gain of TxPD and RxPD is deviate from the expected value. We need to measure the transfer function of each detector again and crosscheck with the measured DC gain of transfer function to find where we lost the gain. Furthermore, we need to understand the reason of DC gain fluctuation in RxPD transfer function. If the reason of amplitude fluctuation is from mirror displacement induced by Pcal beam, we need to adjust the beam size of RxPD or enlarge the aperture of RxPD.

8.1.2 Relative Power Noise

Although we achieved in-loop PD noise to -140 dB/rtHz, the out-loop PD noise remains at -130 dB/rtHz, which we still need to control. We need to understand the source of each noises which make this noise floor, e.g. DAC noise, VGA noise, offset noise, detector noise, and so on. The noise floor of DAC and VGA is -130 dBV/rtHz and -135 dBV/rtHz. This is the absolute noise, and the relative noise floor can be reduced by increasing DC

value of photodetector. For example, by increasing DC value of photodetector to be 10 V, the noise of DAC and VGA can be decreased 20 dB.

8.1.3 Peak stability

We performed a hammering test to check the source of the peaks in RxPD. We distinguished some peaks but there are some peaks that happens in several hammering tests. It may come from the joint region of two hammering test position. These peaks should be investigate further.

8.2 Absolute power calibration

8.2.1 Working standard

In this thesis, we use StarBright power meter (Fig. 4.14) to measure the absolute laser power. The systematic error of this power meter calibration is 2.2%. This systematic error directly propagate to calibration error. To reduce the systematic error of absolute power calibration, we will employ working standard (WS) and gold standard (GS) [38]. The working standard KAGRA (WSK) is a integrating sphere with a InGaAs photodetector calibrated by GS of LIGO (GSL). The ratio of measured voltage in WSK and GS is $V_{\mathrm{WSK}}/V_{\mathrm{GSL}}$. The GSL is calibrated by National Institute of Standard and Technology (NIST). The working standard for LIGO Hanford Observatory (LHO) and LIGO Livingston Observatory (LLO) is also calibrated from GSL. We use WSK for calibrating the readout of TxPD and RxPD, which the ratios are $V_{\mathrm{TxPD}}/V_{\mathrm{WSK}}$ and $V_{\mathrm{RxPD}}/V_{\mathrm{WSK}}$. Therefore, we can calibrate the TxPD readout power P_{TxPD} and RxPD readout power P_{RxPD} against the calibrated power standard in NIST P_{GS}, which can be written as

$$P_{\mathrm{TxPD}} = \frac{V_{\mathrm{TxPD}}}{V_{\mathrm{WSK}}}\frac{V_{\mathrm{WSK}}}{V_{\mathrm{GSL}}}P_{\mathrm{GS}} \tag{8.1}$$

$$P_{\mathrm{RxPD}} = \frac{V_{\mathrm{RxPD}}}{V_{\mathrm{WSK}}}\frac{V_{\mathrm{WSK}}}{V_{\mathrm{GSL}}}P_{\mathrm{GS}} \tag{8.2}$$

The estimated laser power uncertainty of this method is 0.52 %.

8.2.2 Gravity Field Calibrator (Gcal)

Beside working standard, an additional method to calibrate absolute laser power of Pcal is gravity field calibrator (Gcal) [52]. Gcal generate modulated gravitational potential by rotating multipole masses with motor. The masses on the motor are placed in a

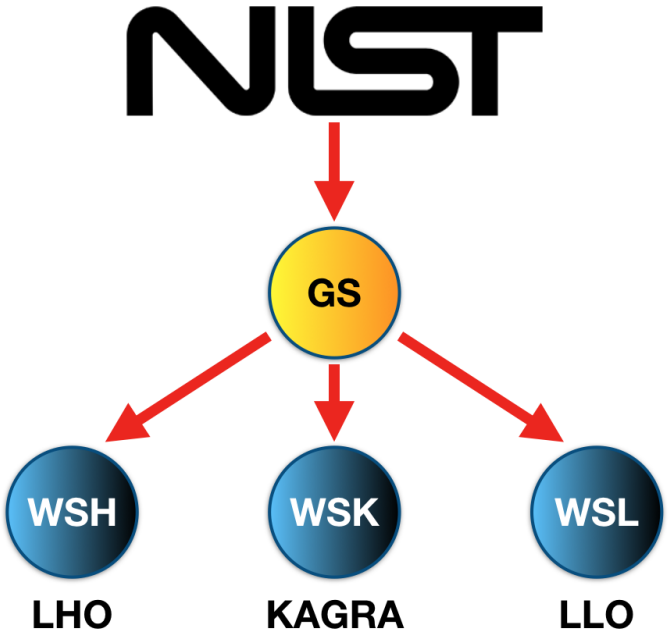

FIGURE 8.1: Absolute power calibration

combination of quadrupole and hexapole arrangement. When Pcal and Gcal is operating, the displacement of the mirror can be described as

$$x = \frac{729}{625}\frac{GMm_{\mathrm{q}}^{5}r_{\mathrm{q}}^{10}}{m_{\mathrm{h}}^{4}r_{\mathrm{h}}^{12}}\frac{V_{3f}^{R^4}}{V_{2f}^{R^5}}V_{\mathrm{in}}s(\omega) \tag{8.3}$$

where m_{q}, r_{q} are the masses and radii of quadrupole arrangement, m_{h}, r_{h} are the masses and radii of hexapole arrangement, V_{2f}^{R} and V_{3f}^{R} are the RxPD readout voltage generated by quadrupole and hexapole of Gcal, V_{in} is the amplitude of input voltage, and $s(\omega)$ is the transfer function of end test mass. This method provides another way to calibrate the absolute laser power of Pcal. The estimated uncertainty of this method is 0.17%.

8.3 Future works

8.3.1 Harmonic noise

To modulate the laser power and send the modulate force to end test mass, we use digital system to generate modulated signal. The modulated signal is sent to AOM to modulate the laser power. However, due to the nonlinearity of AOM, the unwanted harmonic are generated in measured noise spectrum. One of the purpose of Optical Follower Servo is to reduce the harmonics of the modulated signal.

We want to measure the relation between the harmonic noise modulated amplitude. According to AOM transmittance, we set the offset point at the middle of AOM transmittance curve and the total amplitude corresponds to the maximum and minimum transmittance of AOM. We measure the harmonics for the frequencies using for calibration lines. The harmonic noise amplitude depends on the modulated signal amplitude. For each frequency, we adjust the modulated amplitude from 10%, 20% $\cdots$ to 100% and compare the peaks of the harmonic with main peak amplitude. We have calculated the harmonic noise requirement using KAGRA sensitivity curve. We need to reduce the harmonics until below the requirement value.

8.3.2 Peak stability

In order to modulate the mirror with stable force for mirror displacement calibration, we need to generate stable modulated photon pressure, called calibration lines. We will generate 5 calibration lines, with 7 Hz, 35 Hz, 330 Hz, 1 kHz, and 3 kHz with modulated amplitude are set to be signal to noise ratio 100, according to the KAGRA sensitivity requirement. We modulate the laser power, monitored the peak of each calibration lines with one day, one week, one month, and required the uncertainty of the peak value to be with in 1 percent.

Chapter 9

Conclusion

I have developed and characterized the KAGRA Photon Calibrator in order to perform the accurate calibration of gravitational wave signal in KAGRA. KAGRA is a gravitational wave interferometer which is constructed underground and is equipped with cryogenic mirror in order to reduce the seismic noise and thermal noise. KAGRA plans to join gravitational wave network at the end of 2019, and Photon Calibrator will also play an important role in calibration at the same time.

Photon Calibrator generate the modulated photon pressure by auxiliary laser source. The requirement of relative power noise is -140 dB/rtHz. In order to achieve this low noise, I have developed the Optical Follower Servo for stabilizing laser power. Optical Follower Servo is a active controller used for controlling laser power modulation and correcting the relative power noise of laser, and reducing the harmonic noise of the sinusoidal modulation generated by digital system. I have tested the performance of Optical Follower Servo, and showed that the performance of Optical Follower Servo meet our requirement. After that, I measured the beam profile of the laser, and checked the laser performance met the specification from the company. Then I aligned the laser beam to meet the beam profile requirement for AOM and ETM. I achieved to make a 72 meters Photon Calibrator, and measured the performance of it.

First I measure the power loss of the from transmitter module to receiver module, and I found that there were some power loss because the Airy disk of the beams are larger than the aperture of power meter. The reason of the Airy disk comes from the misalignment of the modematching lenses. Then I measure transmittance of AOM, transfer function of each detectors, and use these parameters to calculate the gain of open-loop and closed-loop transfer function of each detector. I confirmed that the transfer function basically matched with our calculation, although the power loss in receiver module

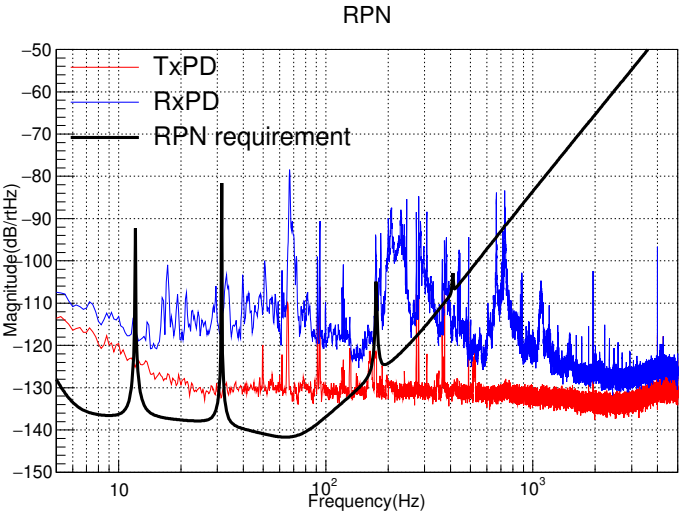

FIGURE 9.1: RPN of Pcal

generated some fluctuations in transfer function amplitude. Next, I move to noise measurement. I measure the noise of laser, digital to analog converter (DAC) of the digital system, and the variable gain amplifier (VGA), to understand each noise source in our Photon Calibrator system. I confirmed that the noise level of digital system is around -130dBV/rtHz. Finally, I measured the relative power noise using OFS closed-loop control, and performed the hammering test to identify the peaks in the noise spectrum of the detector.

We achieved to reach -140 dB/rtHz noise in OFSPD in the transmitter module, the corresponding RPN of TxPD and RxPD is -130 dB/rtHz and -125 dB/rtHz, which is larger than Pcal requirement around than 10 dB/rtHz. The result is shown in Fig. 9.1. When Pcal start operating, we need to achieve RPN level below -140 dB/rtHz.

Bibliography

[1] B. Schutz. *A First Course in General Relativity*. Cambridge University Press, 2009. ISBN 9781139479004. URL https://books.google.co.jp/books?id=GgRRt7AbdwQC.

[2] Christopher M Hirata. Lecture VIII: Linearized gravity, 2012. URL http://www.tapir.caltech.edu/~chirata/ph236/lec08.pdf.

[3] Peter R. Saulson. *Fundamentals Of Interferometric Gravitational Wave Detectors (Second Edition)*. World Scientific Publishing Company, 2017. ISBN 9789813146204. URL https://books.google.co.jp/books?id=KfatDgAAQBAJ.

[4] LIGO, 2018. URL https://www.ligo.caltech.edu.

[5] SOUNDS OF SPACETIME, 2018. URL https://www.soundsofspacetime.org/the-basics-of-binary-coalescence.html.

[6] Benjamin P. Abbott et al. The basic physics of the binary black hole merger GW150914. *Annalen Phys.*, 529(1-2):1600209, 2017. doi: 10.1002/andp.201600209.

[7] B. P. Abbott et al. Observation of Gravitational Waves from a Binary Black Hole Merger. *Phys. Rev. Lett.*, 116:061102, Feb 2016. doi: 10.1103/PhysRevLett.116.061102. URL https://link.aps.org/doi/10.1103/PhysRevLett.116.061102.

[8] B. P. Abbott et al. GW151226: Observation of Gravitational Waves from a 22-Solar-Mass Binary Black Hole Coalescence. *Phys. Rev. Lett.*, 116:241103, Jun 2016. doi: 10.1103/PhysRevLett.116.241103. URL https://link.aps.org/doi/10.1103/PhysRevLett.116.241103.

[9] B. P. Abbott et al. GW170104: Observation of a 50-Solar-Mass Binary Black Hole Coalescence at Redshift 0.2. *Phys. Rev. Lett.*, 118:221101, Jun 2017. doi: 10.1103/PhysRevLett.118.221101. URL https://link.aps.org/doi/10.1103/PhysRevLett.118.221101.

[10] B.. P.. Abbott et al. GW170608: Observation of a 19-solar-mass Binary Black Hole Coalescence. *Astrophys. J.*, 851(2):L35, 2017. doi: 10.3847/2041-8213/aa9f0c.

[11] B. P. Abbott et al. GW170814: A Three-Detector Observation of Gravitational Waves from a Binary Black Hole Coalescence. *Phys. Rev. Lett.*, 119:141101, Oct 2017. doi: 10.1103/PhysRevLett.119.141101. URL https://link.aps.org/doi/10.1103/PhysRevLett.119.141101.

[12] B. P. Abbott et al. GW170817: Observation of Gravitational Waves from a Binary Neutron Star Inspiral. *Phys. Rev. Lett.*, 119:161101, Oct 2017. doi: 10.1103/PhysRevLett.119.161101. URL https://link.aps.org/doi/10.1103/PhysRevLett.119.161101.

[13] B. P. Abbott et al. Multi-messenger Observations of a Binary Neutron Star Merger. *Astrophys. J.*, 848(2):L12, 2017. doi: 10.3847/2041-8213/aa91c9.

[14] B. S. Sathyaprakash and Bernard F. Schutz. Physics, astrophysics and cosmology with gravitational waves. *Living Reviews in Relativity*, 12(1):2, Mar 2009. ISSN 1433-8351. doi: 10.12942/lrr-2009-2. URL https://doi.org/10.12942/lrr-2009-2.

[15] B. P. Abbott et al. Binary Black Hole Mergers in the first Advanced LIGO Observing Run. *Phys. Rev.*, X6(4):041015, 2016. doi: 10.1103/PhysRevX.6.041015.

[16] B. P. Abbott et al. Prospects for Observing and Localizing Gravitational-Wave Transients with Advanced LIGO, Advanced Virgo and KAGRA. *Living Rev. Rel.*, 21:3, 2018. doi: 10.1007/s41114-018-0012-9,10.1007/lrr-2016-1. [Living Rev. Rel.19,1(2016)].

[17] SINET5, 2018. URL https://www.sinet.ad.jp/case/kamioka2.

[18] Virgo, 2018. URL http://www.virgo-gw.eu.

[19] C. Affeldt et al. Advanced techniques in GEO 600. *Class. Quant. Grav.*, 31(22): 224002, 2014. doi: 10.1088/0264-9381/31/22/224002.

[20] LIGO-India, 2018. URL http://www.gw-indigo.org/tiki-index.php?page=LIGO-India.

[21] LIGO Scientific Collaboration. Instrument Science White Paper. *LIGO Document*, 2014. DCC Number T1700231-v2.

[22] Harald Lueck. EINSTEIN TELESCOPE STATUS/PROGRESS/OUTLOOK, 2018. URL http://www.gravity.ircs.titech.ac.jp/GWADW2014/slide/Harald_Lueck.pdf.

[23] Craig Cahillane, Joe Betzwieser, Duncan A. Brown, Evan Goetz, Evan D. Hall, Kiwamu Izumi, Shivaraj Kandhasamy, Sudarshan Karki, Jeff S. Kissel, Greg Mendell,

Richard L. Savage, Darkhan Tuyenbayev, Alex Urban, Aaron Viets, Madeline Wade, and Alan J. Weinstein. Calibration uncertainty for Advanced LIGO's first and second observing runs. *Phys. Rev. D*, 96:102001, Nov 2017. doi: 10.1103/PhysRevD.96.102001. URL https://link.aps.org/doi/10.1103/PhysRevD.96.102001.

[24] E Goetz et al. Accurate calibration of test mass displacement in the LIGO interferometers. *Class. Quant. Grav.*, 27:084024, 2010. doi: 10.1088/0264-9381/27/8/084024.

[25] Optical Breadboards with Sealed Holes, 2018. URL https://www.thorlabs.com/newgrouppage9.cfm?objectgroup_id=7164&pn=B9090L.

[26] LEA Photonics. CW YtterbiumFiber Laser, 2018. URL http://www.lea-photonics.com/products-services-lasers-amplifiers/ytterbium-fiber-laser/.

[27] Ophir. StarBright P/N 7Z01580, 2018. URL https://www.ophiropt.com/laser--measurement/laser-power-energy-meters/products/laser-power-meters/starbright.

[28] Go Photonics. QWPO-1047-05-2-R10, 2018. URL https://www.gophotonics.com/products/waveplates/cvi-laser-optics/38-441-qwpo-1047-05-2-r10.

[29] Karl Lambrecht Corporation. Narrow Band Polarizing Cubes, 2018. URL http://www.klccgo.com/tfpc.htm.

[30] CVI Laser Optics. Y1S: Ion Beam Sputtered High Energy Nd:YAG Laser Mirror, 1064nm, 2018. URL https://www.cvilaseroptics.com/y1s-ion-beam-sputtered-high-energy-nd-yag-laser-mirror-1064nm/product/y1s_ion_beam_sputtered_high_energy_nd-col-yag_laser_mirror.

[31] CVI Laser Optics. BS1: High Energy Plate Beamsplitter, 2018. URL https://www.cvilaseroptics.com/bs1-high-energy-plate-beamsplitter/product/bs1_high_energy_plate_beamsplitter.

[32] ISOMET. M1080-T80L-1.5 NIR Acousto-Optic Modulator, 2018. URL http://www.isomet.com/AO_Pdf/M1080-T80L-NIR.pdf.

[33] ISOMET. 532C-x Series Analog Modulation RF Driver, 2018. URL http://www.isomet.com/RF_Pdf/532C_C4_C7.pdf.

[34] CVI Laser Optics. PLCX-UV: Laser Grade Plano-Convex Lenses, Fused Silica, NIR, 2018. URL https://www.cvilaseroptics.com/plcx-uv-laser-grade-plano-convex-lenses-fused-silica-nir-wavelengths/product/plcx_uv_laser_grade_plano-convex_lens_NIR.

[35] HOLO/OR. SA-014-I-Y-A, 2018. URL http://www.holoor.co.il/Diffractive_Optics_Products/php/productParameters_page.php?PN=SA-014-I-Y-A&lamda=1064&Dim=1D.

[36] Lasermet. LS-10-12, 2018. URL https://www.lasermet.com/laser-beam-shutters.php.

[37] Thorlabs. Position Sensing Detector, 2018. URL https://www.thorlabs.com/drawings/11270d9584aca95-5F09E1F8-D4EA-EDE0-AACC89240832C546/PDQ30C-SpecSheet.pdf.

[38] Y. Inoue, Y.-K. Chu, S. Haino, B.-H. Hsieh, N. Kanda, T. Shishido, T. Tomaru, T. Yamamoto, and T. Yokozawa. KAGRA Photon Calibrator, 2017. Design report T1706293 Ver.5.

[39] Thorlabs. BP209-VIS/M - Dual Scanning Slit Beam Profiler, 2018. URL https://www.thorlabs.com/thorproduct.cfm?partnumber=BP209-VIS/M.

[40] Thorlabs. Operating Ranges of the BP209 Series, 2018. URL https://www.thorlabs.com/newgrouppage9.cfm?objectgroup_id=804.

[41] Astrophysics and Space Research Group (ASR) Wikis. JamMt - Just another mode matching tool, 2018. URL http://www.sr.bham.ac.uk/dokuwiki/doku.php?id=geosim:jammt.

[42] B. Abbott. Optical Follower Servo. *LIGO Document*, 2014. DCC Number D1300514-v4.

[43] B. Abbott. Optical Follower Back board. *LIGO Document*, 2013. DCC Number D1300561-v1.

[44] B. Abbott. PCal Interface board. *LIGO Document*, 2014. DCC Number D1400152-v2.

[45] B. Abbott. PCal Interface back board. *LIGO Document*, 2014. DCC Number D1400149-v1.

[46] LM317 3-Terminal Adjustable Regulator, 2018. URL http://www.ti.com/lit/ds/symlink/lm317.pdf.

[47] M137, LM337-N3-Terminal AdjustableNegativeRegulators, 2018. URL http://www.ti.com/lit/ds/symlink/lm137.pdf.

[48] B. Abbott. Pcal Interface Chassis Test Procedure. *LIGO Document*, 2014. DCC Number T1400484-v2.

[49] Spherical aberration, 2018. URL https://en.wikipedia.org/wiki/Spherical_aberration.

[50] ISOMET. Acousto-optic Modulation, 2018. URL http://www.isomet.com/App-Manual_pdf/AO%20Modulation.pdf.

[51] Ophir Power/Energy Meter Calibration Procedure and Traceability/Error Analysis, 2018. URL https://www.ophiropt.com/laser--measurement/knowledge-center/article/1110.

[52] Yuki Inoue, Sadakazu Haino, Nobuyuki Kanda, Yujiro Ogawa, Toshikazu Suzuki, Takayuki Tomaru, Takahiro Yamanmoto, and Takaaki Yokozawa. Improving the absolute accuracy of the gravitational wave detectors by combining the photon pressure and gravity field calibrators. *Phys. Rev.*, D98(2):022005, 2018. doi: 10.1103/PhysRevD.98.022005.